UNIVERSITY OF UDINE

PHD PROGRAMME IN ENVIRONMENTAL AND ENERGY ENGINEERING SCIENCE
XXXVIII CYCLE

Performance Analysis and Optimization of Receivers for Solar Thermal Power Plants

---

Candidate:
Vinod Kumar

Supervisor:
Prof. Stefano Savino

Co-Supervisor:
Prof. Carlo Nonino

A thesis submitted in fulfillment of the requirements for the degree of Doctor of Philosophy

2026

Author's e-mail:

kumar.vinod@spes.uniud.it
vkhokhar_4u@yahoo.com

Author's address:

Polytechnic Department of Engineering and Architecture
University of Udine
via delle Scienze 206
33100 Udine - Italy

Last updated

Udine - February 22, 2026

"The sun shines equally on all; technology decides who harnesses it"

Credits

I, Vinod Kumar, declare that this thesis entitled, "Performance Analysis and Optimization of Receivers for Solar Thermal Power Plants" and the work presented are:

- **Chapter 4**: This work was carried out at the Computational Thermal Fluid Dynamics research group in the University of Udine.
- **Chapter 5**: This work was carried out at the Computational Thermal Fluid Dynamics research group in the University of Udine.
- **Chapter 6**: This work was carried out at the Line-Focus Concentrating Solar Thermal Technologies Unit in the Plataforma Solar de Almería (PSA)- CIEMAT, Almeria (Spain), under the supervision of Dr. Loreto Valenzuela.
- **Chapter 7**: This work was carried out at the Thermal Engineering Research Group in the University of Twente, Enschede (Netherlands), under the supervision of Dr. A.K. Singh.

Udine, February 22, 2026

Abstract

Parabolic Trough Collector (PTC) technology is one of the most mature and widely deployed Concentrating Solar Thermal/Power (CST/CSP) technologies for medium- to high-temperature thermal applications. Improving the thermal efficiency, reliability, and dispatchability of PTC plants requires advancements at both the receiver and system levels, including effective thermal energy storage. This thesis presents a comprehensive numerical investigation into the thermal optimisation of parabolic trough receivers and preliminary modelling of thermochemical energy storage (TCES) systems, addressing key heat transfer mechanisms, heat loss pathways, and system integration challenges in CSP plants.

Following a comprehensive literature review on heat transfer enhancement techniques and thermal loss mechanisms in parabolic trough receivers, the first part of the thesis focuses on enhancing the thermal performance of receiver tubes through internal heat transfer augmentation. Longitudinal fins are investigated as a simple and cost-effective modification to the absorber tube. Detailed Computational Fluid Dynamics (CFD) simulations are conducted to evaluate the influence of fin number, height, and circumferential placement under the inherently non-uniform solar heat flux distribution characteristic of PTC receivers. A novel performance evaluation metric is proposed to provide a more representative comparison than conventional methods. The numerical model is validated against experimental data from the literature. Results demonstrate that optimal configurations require shorter fins in high heat flux regions and longer fins in low heat flux regions, achieving up to a 45.6% enhancement in the overall Nusselt number and an 18.0% reduction in heat losses compared to smooth receivers.

The second part of the thesis investigates heat loss mechanisms in smooth and longitudinally finned parabolic trough receivers under varying annulus vacuum levels. A coupled heat transfer model incorporating conduction, convection, and radiation is developed to quantify the effects of annulus pressure, ambient conditions, and heat transfer fluid inlet temperature. The results reveal that total heat loss increases significantly with rising annulus pressure and operating temperature, with conductive losses becoming dominant as vacuum degrades, while radiative losses remain relatively constant. The inclusion of longitudinal fins lowers the outer surface

temperature of the receiver and reduces total heat loss by approximately 9%, highlighting their added benefit under non-ideal vacuum conditions.

The third part examines the thermal behaviour of evacuated linear receivers under realistic operating scenarios, including hydrogen accumulation in the annulus and external wind effects. CFD simulations over a wide range of mass flow rates, inlet temperatures, solar irradiance levels, and wind speeds show that hydrogen presence can increase heat losses by up to three times compared to fully evacuated conditions, resulting in elevated glass envelope temperatures. Increasing the mass flow rate significantly reduces circumferential temperature gradients in the absorber tube, thereby mitigating thermal stresses. Wind effects are found to increase convective heat losses while simultaneously reducing glass temperatures.

The final part of the thesis presents additional work on the numerical modelling of $CaO/Ca(OH)_2$-based thermochemical energy storage to complement the receiver-focused investigations and address system-level dispatchability. A high-fidelity CFD–UDF framework is developed in ANSYS FLUENT to simulate coupled heat transfer, mass transport, and reaction kinetics in a packed-bed TCES reactor.

Overall, the thesis provides an integrated numerical framework for improving receiver performance and advancing thermochemical energy storage modelling, contributing to more efficient, reliable, and dispatchable solar thermal power systems.

Acknowledgements

Throughout my PhD, I have received a great deal of support and assistance. Doing a PhD abroad is challenging and can lead to mixed feelings, especially when leaving behind a two-month-old baby, facing cultural differences, and overcoming language barriers. At this point, I can say without a doubt that it was the best decision of my life. I will always be grateful to everyone I have had the opportunity to meet during these years who made me feel at home. I am happy to have found another big family, and Udine will always be in my heart.

First and foremost, I would like to thank my supervisor, Professor Stefano Savino, for all his help, patience and encouragement throughout my PhD. His wise guidance and consistent support have kept me on track and motivated. Thank you, Professor Savino, for your help and active participation in writing this thesis. I will always be grateful for everything you have taught me, including compassion, patience, support and availability, as well as the passion you bring to your work. You are an amazing person, both personally and professionally. Thank you for always being there, listening and caring. I really hope you are happy with the final result. This thesis could not have been completed without your guidance, and I'm extremely proud of what we achieved together. Thank you for giving me this opportunity!

I would also like to express my gratitude to my co-supervisor, Prof. Carlo Nonino, for his invaluable assistance and for always taking the time to offer me valuable insights. His technical advice has helped me in many ways, from solving problems and improving my methods to enhancing my research overall. I am very grateful for his help with writing scientific papers and preparing presentations. He always helped me improve my slides, paying special attention to details such as alignment, fonts and the clarity of graphs. This made my work look much more professional. His accuracy, hard work and constant support have had a significant impact on my growth as a researcher.

A big thank you to Dr. Loreto Valenzuela of Plataforma Solar Almería (PSA) in Spain for giving me the chance to do research at the world's biggest concentrating solar thermal plant. This experience really helped my research and taught me a lot more about solar thermal technology.

I am very grateful to Dr. A.K. Singh from the University of Twente, Netherlands, for approving my request to conduct research on thermochemical energy storage for CST applications. His help and the collaborative environment he created were very important for moving my study forward in this area.

I want to thank all of my colleagues, fellow researchers, and the academic community at the University of Udine in Italy for their help and support. Their guidance and ideas have helped me become a better researcher and made the journey more fulfilling.

Finally, I want to thank my lovely wife, Pushpa Mohan, and my son, Manvir Khokhar, for always being there for me and loving me. Even though my family is in Pakistan and I am in Italy, their patience and sacrifices have always been a source of strength and motivation for me. I also want to thank my parents for their blessings, support, and faith in me, which have always been my guiding light. I really couldn't have finished my journey without them.

Contents

List of Figures

List of Tables

Nomenclature

A_c	Flow cross-sectional area	[m^2]
A_{ri}	Receiver inner surface area	[m^2]
A_{ro}	Receiver outer surface area	[m^2]
c_p	Specific heat	[$J/(kg\,K)$]
D_{gi}	Glass cover inner diameter	[m]
D_{go}	Glass cover outer diameter	[m]
D_{ri}	Receiver tube inner diameter	[m]
D_{ro}	Receiver tube outer diameter	[m]
ΔP	Pressure drop	[Pa]
$\Delta P/L$	Pressure gradient	[Pa/m]
f	Friction factor	[-]
g	Gravitational acceleration	[m/s^2]
H, H_l, H_s	Fin heights (medium, long, short)	[mm]
h_i	Inner heat transfer coefficient	[$W/(m^2\,K)$]
h_o	Overall heat transfer coefficient	[$W/(m^2\,K)$]
L	Length	[m]
$\dot{m}$	Mass flow rate	[kg/s]
N	Number of fins	[-]
Nu, $\mathrm{Nu_i}$, $\mathrm{Nu_o}$	Nusselt numbers	[-]
Q_{loss}	Heat loss	[W/m]
Q_{tot}	Total heat	[W/m]
Q_u	Useful heat	[W/m]
Ra	Rayleigh number	[-]
Re	Reynolds number	[-]
t	Fin thickness	[mm]
T_{amb}	Ambient temperature	[°C]
T_b, $T_{b,in}$, $T_{b,out}$	Bulk fluid temperatures	[°C]
T_{go}	Glass outer wall temperature	[°C]
T_{in}, T_{out}	Inlet and outlet temperatures	[°C]

T_{ri}	Receiver inner wall temperature	[°C]
T_{ro}	Receiver outer wall temperature	[°C]
T_{sky}	Sky temperature	[°C]
u_{in}	Inlet velocity	[m/s]
α, θ	Angles	[°]
β	Thermal expansion coefficient	[K^{-1}]
ϵ	Emissivity	[-]
λ	Thermal conductivity	[W/(m K)]
μ	Dynamic viscosity	[mPa · s]
ρ	Density	[kg/m^3]
$\sigma_{h,t}$	Turbulent Prandtl number	[-]
ri	Receiver inner	
ro	Receiver outer	
amb	Ambient	
gi	Glass inner	
go	Glass outer	
in	Inlet	
out	Outlet	
r	Receiver	
avg	Average	
max	Maximum	
min	Minimum	
DNI	Direct normal irradiance	[W/m^2]
PTC	Parabolic trough collector	
PTR	Parabolic trough receiver	
HTF	Heat transfer fluid	
CST	Concentrating solar thermal	
LCR	Local concentration ratio	[-]
PSA	Plataforma Solar de Almería	

Dedicated to
Pushpa and Manvir

Chapter 1

Introduction

1.1 Motivation

Due to increasing energy demand and the depletion of conventional energy sources, concentrating solar thermal (CST) technologies have emerged as a reliable option for generating both electricity and industrial heat [1, 2]. The most advanced and extensively used CST technology is the parabolic trough collector (PTC). In the PTC system, sunlight is focused onto a linear receiver by a parabolic mirror along its focal line. A heat transfer fluid (HTF) then circulates through the receiver, carrying the absorbed heat to a power block, a thermal storage device, or end users. Therefore, the parabolic trough receiver (PTR) is essential for the system's thermal efficiency and durability [3].

One of the main challenges associated with parabolic trough systems is the non-uniform heat flux distribution on the receiver tube. Most of the radiation is reflected by the parabolic mirror to the bottom of the tube, resulting in the lower surface absorbing more heat than the upper surface. The temperature variations along the tube circumference induce thermal stresses, mechanical deformation, and selective degradation of the coating. In severe conditions, these stresses can result in tube bowing, fractures in the glass envelope, or failure of the glass-to-metal seal [4, 5].

Furthermore, prolonged operation of the HTF at high temperatures promotes thermal decomposition, generating hydrogen gas that permeates the receiver wall and enters the vacuum annulus. In the annulus, as the getter materials (chemically reactive metallic compounds designed to absorb residual gas molecules and maintain the vacuum) gradually become saturated, hydrogen accumulation reduces the vacuum level, causing an increase in conductive and convective heat losses, sometimes by a factor of three. This degradation reduces the receiver thermal efficiency and accelerates long-term performance decline [6].

Operational experience from commercial PTC plants, especially the SEGS facilities in California, has shown that receiver reliability is one of the most significant concerns with parabolic trough technology. Price *et al.* [7] reviewed field data and found multiple types of failures that keep happening because of mechanical, thermal, and material stresses. Table 1.1 summarizes the principal types of receiver failure, their main causes, and their associated effects. These findings highlight the need for more robust receiver designs and improved thermal management strategies, both of which form the central motivation for the present research on enhanced heat transfer and vacuum stability in parabolic trough receivers.

As will be discussed in detail in Chapter 2, most previous studies have looked at either internal heat transfer enhancements or vacuum degradation separately, without considering how the two affect each other. In real operating conditions, these effects happen at the same time and influence both heat transfer and the receiver's overall reliability. Because of this, the goal of this thesis is to develop a detailed heat-transfer model that combines both effects, that is, the geometry of the longitudinal fins and the quality of the vacuum, to better understand how they interact. The primary objective is to develop receiver designs that exhibit higher efficiency, a more uniform temperature distribution, and consequently, improved mechanical strength, thereby enhancing the next generation of solar thermal power systems.

The results show that using well-designed longitudinal fins, especially asymmetric ones that match the non-uniform heat flux around the receiver, can reduce temperature differences, enhance heat transfer, and lower heat losses. The thesis also shows that maintaining a good vacuum around the receiver is just as important, since hydrogen buildup, air leaks, or wind can increase heat losses and lower efficiency. Overall, a receiver's performance depends on how efficiently it transfers heat inside to the HTF and how much heat it loses to the surroundings. This work combines both aspects into one model, helping to design receivers that are more efficient, more uniform in temperature, and more reliable for long-term use in solar thermal plants.

TABLE 1.1: Summary of Common Receiver Failures in PTC Systems [7].

Failure Type	Main Cause	Effect / Result
Receiver bowing	Non-uniform heat flux or low HTF flow rate	Glass breakage, major heat loss
Vacuum loss	Seal, hydrogen permeation, getter saturation	Increased heat loss, reduced efficiency
Glass breakage	Bowing, seal failure, or mechanical impact	Loss of vacuum, $3\times$ heat loss, tube replacement

1.2 Research Context

PTC systems are currently the most advanced and commercially viable form of CST technology [8, 9]. They account for more than half of the world's installed concentrating solar power (CSP) capacity [10].

The linear receiver of a PTC (commonly called an absorber or heat collection element) consists typically of a stainless steel tube enclosed within an anti-reflective borosilicate glass tube (also known as a glass envelope or glass cover). Glass-to-metal seals are installed between the outer surface of the absorber and the glass tube to create a vacuum space in the annulus, reducing convective heat losses and preventing oxidative degradation of the selective steel tube coating [5]. Typically, the vacuum is maintained at 10^{-2} mbar. The selective coating helps to increase the absorptance of direct and reflected radiation and maintains a low thermal emissivity at high operating temperatures. Even with an optimal design, the receiver operates under extremely harsh conditions, facing intense solar flux and large temperature swings. Over time, these stresses make it difficult for the receiver to maintain high performance [11].

The lower part of the receiver tube receives reflected solar radiation, causing it to become significantly hotter than the upper part, which is exposed only to direct radiation. The nonuniform distribution of heat flux causes a circumferential temperature difference in the receiver tube that leads to thermal stresses, damage to the coating, and bending of the tube, especially at low flow rate conditions. Over time, these effects lead to losses in efficiency and possible damage to the structure [12].

To address these issues, researchers have explored various methods for enhancing internal heat transfer. Numerous studies have assessed the effectiveness of passive techniques for improving convective heat transfer between the receiver wall and the HTF. Approaches such as twisted tapes, wire coils, and longitudinal fins have been investigated, among others [13]. Further details are provided in Chapter 2. Longitudinal fins have been shown to be an effective solution, offering significant enhancement of internal heat transfer with minimal pressure loss, while being simple and cost-effective. The configuration and positioning of the fins have a significant influence on the temperature distribution and the receiver's overall thermal performance [14].

Although the internal fins greatly improve convective heat transfer within the receiver tube, the receiver's external thermal losses are largely influenced by the integrity of the vacuum in the annular region. In practice, receivers rarely achieve ideal vacuum conditions throughout their operational lifespan due to factors such as hydrogen permeation, air leakage, and getter degradation, which progressively increase the annular pressure. As this pressure rises, conduction and natural convection become more important, resulting in total heat losses that can increase by more than threefold under degraded vacuum conditions [15].

Even after implementing internal enhancements, the vacuum level in the annular area continues to have a significant impact on the receiver's heat-loss performance. Several factors can contribute to increasingly severe vacuum degradation, including hydrogen escaping from the HTF, air seeping through seals, and getter fatigue. Total heat loss increases threefold or fourfold compared to optimal vacuum conditions due to the significant increase in conductive and convective losses. Hydrogen has the greatest impact on the receiver's vacuum quality due to its significantly higher heat conductivity compared to air [16].

1.3 Identified gaps and research questions

A comprehensive and critical review of parabolic trough receivers, internal heat transfer enhancement techniques, and thermal loss mechanisms is presented in Chapter 2. Despite the extensive research, several aspects of their thermal behaviour remain insufficiently understood. In particular, the combined influence of non-uniform solar heat flux, internal heat transfer enhancement techniques, and external heat-loss mechanisms has not been comprehensively addressed under realistic conditions. Based on a critical assessment of existing work and the scope of the present PhD research, the following principal knowledge gaps are identified.

- Most current research assumes uniform circumferential heat flux/temperature distributions or symmetrical fin arrangements. This overlooks the fact that solar flux distributions are intrinsically non-uniform in real PTC systems.
- The effect of the position, number and height of longitudinal fins on circumferential temperature uniformity, maximum receiver temperatures and overall heat losses under non-uniform heat flux conditions has not been thoroughly investigated.
- The combined effect of internal fins and heat loss due to vacuum degradation and ambient conditions has not been investigated systematically.
- Most studies on evacuated PTC receiver tubes assume that the annular space is completely evacuated, but in reality partial vacuum conditions and gases such as air and hydrogen can significantly affect heat transfer.
- There is a lack of appropriate performance metrics to effectively evaluate and compare the overall thermal performance of finned (internally enhanced tubes) and smooth receiver tubes under non-uniform heat flux conditions.

To address these gaps, the present research is guided by the following research questions:

1. How do the height, number, and circumferential placement of longitudinal fins influence heat transfer performance, temperature distribution, and pressure drop within parabolic trough receivers?
2. What are the dominant heat-transfer mechanisms associated with fins located in different circumferential regions of the absorber tube, and how do these mechanisms influence circumferential temperature uniformity and hot-spot formation?

3. How does vacuum degradation resulting from hydrogen permeation or air leakage into the annular space affect total heat loss and thermal behaviour in both smooth and finned receivers?

4. What is the combined impact of internal fin geometry and vacuum degradation on the overall thermal performance and efficiency of the receiver?

5. Can a new performance metric be developed to enable meaningful comparison of finned and smooth receivers under non-uniform heat flux conditions?

1.4 Contribution to the knowledge

This PhD research contributes to the understanding and optimization of parabolic trough receivers by providing new insights into the coupled effects of fin geometry and vacuum degradation. The main contributions can be summarized as follows:

- Development of a three-dimensional conjugate heat-transfer model that integrates conduction, convection, and radiation mechanisms to represent realistic operating conditions.

- Quantitative evaluation of the influence of fin height, number, and circumferential position on heat transfer, temperature gradients, and pressure drop.

- Identification of the dominant heat-transfer mechanisms for fins, showing that fins on the bottom side enhance conduction while upper side fins promote convection.

- Demonstration that asymmetric fin configurations, with shorter fins in the high-flux region (lower side) and longer fins in the upper region, reduce the maximum wall temperature and increase the overall Nusselt number compared with a smooth receiver.

- Comprehensive analysis of vacuum degradation effects, showing that hydrogen ingress can increase total heat loss by a factor of three to four relative to a fully evacuated annulus.

- Confirmation that the inclusion of longitudinal fins lowers the outer-wall temperature and total heat loss even under degraded vacuum conditions, demonstrating their dual role in improving internal and external thermal performance.
- Development of a new performance evaluation framework that overcomes the limitations of conventional metrics and enables meaningful comparison of finned and smooth receiver tubes under non-uniform heat flux.

As already mentioned, despite extensive work on internal heat-transfer enhancement and external heat-loss mitigation, existing studies typically analyse these mechanisms separately and under simplified assumptions that do not reflect real plant behaviour. In practice, however, parabolic trough receivers operate under strongly non-uniform solar flux, temperature-dependent fluid properties, flow redistribution caused by fins, and progressive vacuum degradation driven by hydrogen permeation. Moreover, these effects are coupled and simultaneously influence temperature uniformity, internal convection, radiative and conductive losses, and long-term receiver durability. To address this complexity, the present PhD research develops a series of three-dimensional conjugate heat-transfer models—ranging from periodic finned-receiver domains to full-length commercial receivers—to capture the interactions between fin geometry, circumferential flux asymmetry, vacuum degradation, and gas composition. This integrated modelling approach enables a realistic understanding of receiver thermo-hydraulic behaviour and provides a rigorous foundation for optimizing fin configurations, quantifying vacuum-loss impacts, and guiding the design of next-generation high-efficiency parabolic trough receivers.

1.5 Software packages

Specialised software tools were employed to create geometries, generate meshes, run simulations and process the resulting data. The main software used in this study is listed below.

- **ANSYS Workbench:** It is used as the primary simulation platform, providing an integrated environment for preparing geometry, generating meshes, setting up solvers and processing results. Versions from 2023 R1 through 2025 R2 were employed over the course of this study.
- **ANSYS Meshing:** This was used to generate high-quality computational meshes.
- **ANSYS Fluent:** It was used as the primary CFD solver to simulate fluid flow and heat transfer. The governing equations were solved using the finite volume method with the appropriate turbulence and radiation models, as well as suitable discretisation schemes.
- **CFD-Post:** This was used for the post-processing and visualisation of simulation results, including velocity fields, pressure contours and temperature distributions.
- **Tecplot:** It was used for the advanced visualisation and analysis of CFD results.
- **Engineering Equation Solver (EES):** It was used for thermodynamic and heat transfer calculations, as well as for verifying analytical models. The built-in property database facilitates the efficient and accurate solution of complex equations.
- **REFPROP:** Accurate thermophysical properties of working fluids were obtained from the NIST Reference Fluid Thermodynamic and Transport Properties Database, ensuring consistency between analytical and numerical calculations.
- **Gnuplot:** Used for plotting and analyzing numerical data. Gnuplot facilitated the creation of high-quality 2D and 3D plots, contour maps, and comparative visualizations of simulation and analytical results.

1.6 Publications

The main findings of this thesis have been published in the following papers:

1.6.1 Papers for international journals

- **Vinod Kumar**, Stefano Savino, Carlo Nonino, On the improvement of the thermal performance of longitudinally finned parabolic trough solar receivers - *Applied Thermal Engineering* - LINK
- **Vinod Kumar**, Stefano Savino, Rafael Lopez-Martin, Loreto Valenzuela, Effect of Vacuum Degradation on Heat Losses in Parabolic Trough Collector Receivers - *Applied Thermal Engineering* - (LINK)
- **Vinod Kumar**, Stefano Savino, Carlo Nonino, Effect of height and position of inner rectangular longitudinal fins in parabolic trough solar receivers - *Computational Thermal Sciences: An International Journal* - LINK

1.6.2 Papers for international conferences

- **Vinod Kumar**, Stefano Savino, Carlo Nonino, Effect of height and position of inner rectangular longitudinal fins in parabolic trough solar receivers. 41st *UIT International Heat Transfer Conference, Naples, Italy* 19-21 June, 2024
- **Vinod Kumar**, Stefano Savino, Carlo Nonino, Enhancing the thermal efficiency of longitudinally finned parabolic trough solar receivers. 30th *International Conference on Solar Power & Chemical Energy Systems (SolarPACES), Rome, Italy* 8-11 October 2024- LINK
- **Vinod Kumar**, Carlo Nonino, Stefano Savino, Numerical analysis of heat losses in smooth and longitudinally finned parabolic trough receivers under various vacuum conditions. *Journal of Physics: Conference Series* - Under review with minor revisions

1.7 Structure of the Thesis

This thesis is organized into seven chapters, each addressing a specific aspect of the research carried out during the Ph.D. programme. A brief overview of the contents of each chapter is provided in the following table.

Chapter 1	Introduces Concentrated Solar Thermal systems, motivation, research context, identified gaps, research questions, contributions, software tools, publications, and the overall thesis structure.
Chapter 2	Provides a comprehensive literature review covering heat transfer enhancement techniques in parabolic trough receivers, thermal loss mechanisms, and research gaps relevant to receiver performance.
Chapter 3	Describes the numerical modelling of parabolic trough collector receivers, including system geometry, computational domain, governing equations, boundary conditions, modelling approaches, and data processing methodology.
Chapter 4	Presents the thermal–hydraulic performance analysis of longitudinally finned receivers under non-uniform heat flux, including flow behaviour, temperature fields, fin effects, Nusselt numbers, pressure drop, and performance evaluation criteria.
Chapter 5	Investigates the influence of vacuum degradation on heat losses in smooth and finned receivers, analysing radiative and conductive losses under varying annulus pressures and atmospheric conditions.
Chapter 6	Examines the effect of hydrogen-induced vacuum degradation in commercial receivers using a detailed 3D conjugate heat-transfer model, including temperature profiles, circumferential gradients, heat-loss mechanisms, and wind effects.
Chapter 7	Presents additional work on thermochemical heat-storage modelling that can be used for PTC systems, including reactor modelling, governing equations, reaction kinetics, and hydration/dehydration behaviour.

Chapter 2

Literature Review

Overview

Rising energy demand, the depletion of conventional energy sources, and climate change have major problems worldwide. At the same time, fossil fuel power plants account for around 60% of global electricity output and are a major source of pollution. To address this problem, researchers must focus on long-term solutions. One effective approach is to utilize clean and renewable energy sources. Solar thermal energy is a viable solution that can meet rising energy demands while reducing greenhouse gas emissions and fossil fuel consumption. Concentrating Solar Thermal (CST) is among the most promising environmentally friendly technologies for heat and power generation [17, 18].

There are two main types of concentrated configurations among CST systems: point-focus and line-focus. Point-focus systems, such as solar towers and dish-Stirling units, concentrate sunlight onto a single focal point. This achieves very high temperatures, which are suitable for generating electricity and advanced thermal applications. Line-focus systems, including parabolic troughs and linear Fresnel collectors, concentrate sunlight along a line to heat a working fluid. These systems typically operate within medium temperature ranges, suitable for power and heat generation. The Parabolic Trough Collector (PTC) is the most mature and commercially viable technology among these systems and is widely used for power generation and industrial process heat [19–21]. It comprises a parabolic reflector that concentrates solar radiation onto a receiver tube, enclosed in a glass cover, where a Heat Transfer Fluid (HTF) absorbs thermal energy [22], as shown in the Figure 2.1. The linear receiver of a PTC (commonly called absorber or heat collection element) [3, 20] consists typically of a stainless steel tube enclosed within an anti-reflective borosilicate glass tube (also known as glass envelope or glass cover). Glass-to-metal seals are installed between the outer surface of the absorber and the glass tube to create a vacuum space in the annulus, reducing convective heat losses and preventing oxidative degradation of the selective steel tube coating. Typically, the vacuum is maintained at 10^{-2} mbar. The selective coating helps to increase the absorptance of direct and reflected radiation and maintains a low thermal emissivity at high operating temperatures [5].

FIGURE 2.1: Parabolic trough collector system.
Source: PSA/CIEMAT.

To structure the discussion effectively, the chapter is organized into two main literature review sections. The first section reviews research on heat transfer enhancement techniques in PTC receivers, and the second analyzes the different thermal loss mechanisms affecting receiver performance.

2.1 Overview of Heat Transfer Enhancement Techniques in PTC Receivers

The receiver tube is the main and most critical component of the PTC system, as it is exposed to a non-uniform heat flux distribution, which may lead to large temperature gradients at low HTF flow conditions. Various passive enhancement methods have been proposed to improve thermal performance and mitigate temperature gradients in PTC receivers and extend their lifespan. Comprehensive reviews of these techniques can be found in [13, 14, 23]. Some of the most commonly employed internal enhancement techniques include twisted tapes, wire coils, porous media, rings, the use of nanofluids, fins, and other heat transfer techniques [24]. A summary of the reviewed internal enhancement techniques is shown in Figure 2.2.

2.1.1 Twisted tapes

Song *et al.* [25] performed a numerical analysis of the thermal performance of a PTC receiver tube with a helical screw-tape insert and Dowtherm-A as the HTF, as shown in Figure 2.3a. The analysis considered Reynolds numbers between 10,000 and 75,000, as well as inlet temperatures ranging from 373 K to 640 K. The results showed that the insert improved thermal performance by reducing heat losses and maximum absorber temperatures compared to a smooth receiver tube. At mass flow rates of 0.6 and 0.11 kg/s, respectively, heat losses were reduced by a factor of three and six compared to a smooth tube. However, the pressure drop increased 23 times in the case of the helical screw-tape insert. Mwesigye *et al.* [26] conducted a numerical analysis to evaluate the impact of a wall-detached twisted tape on the thermal efficiency of a PTC system, as shown in Figure 2.3 b. The Reynolds numbers range varies from 10,260 to 1,353,000, with Syltherm 800 oil as the HTF and inlet temperatures of 400 K, 500 K, and 600 K. Different twist ratios (0.5, 1, 1.5, and 2) and width ratios (0.53–0.91) were investigated. The findings demonstrated that augmenting the width ratio and diminishing the twist ratio markedly enhanced thermal performance, albeit resulting in a moderate increase in the friction factor. The thermal performance and friction factor increased by 1.05–2.69 times and 1.6–14.5 times, respectively, compared to a smooth receiver tube. Also, when the twist ratio

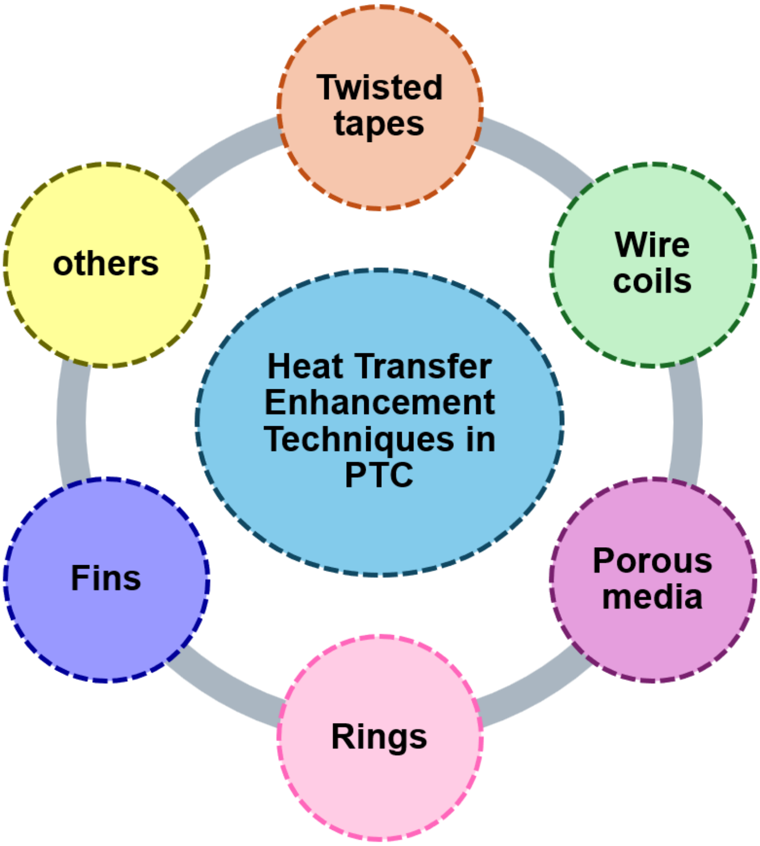

FIGURE 2.2: Different heat transfer enhancement techniques used in PTC receivers.

was more than 1, using twisted tapes reduced the circumferential temperature variation of the absorber tube by 4–68% and increased the thermal efficiency by 5–10%. Liu *et al.* [27] conducted a numerical optimization study in which two twisted-tape inserts were employed to improve the thermal performance of PTC receivers in direct steam generation (DSG) systems. The study aimed to minimize the temperature difference around the absorber tube by optimizing the flow field under specified viscous dissipation constraints. The results showed that generating longitudinal vortices along the main flow direction significantly improved temperature

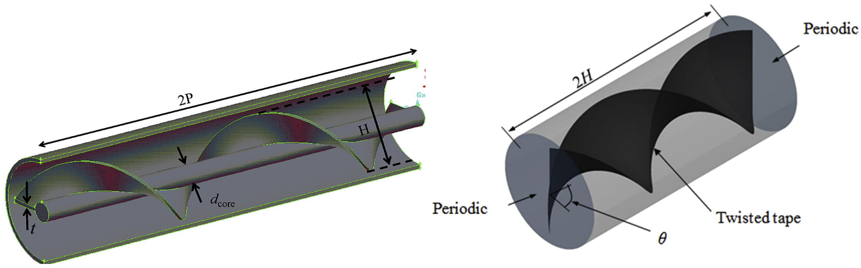

FIGURE 2.3: PTC receiver tube with a) helical-screw tape [25] and b) twisted tape [26].

uniformity, reducing the temperature difference from 69 K to 42 K. Mehta *et al.* [28] experimentally investigated the thermal performance enhancement of a parabolic trough solar collector (PTC) using single and dual twisted-tape inserts within the absorber tube. Experiments were conducted at Reynolds numbers ranging from 1,000 to 9,000, with pitch-to-width ratios $y/w = 1, 1.5, 2, 2.5, 3$ for single twisted tapes and $y/y_0 = 2, 3, 4$ for dual twisted tapes. The results indicated that the dual twisted-tape configuration with a pitch ratio of $y/y_0 = 2$ achieved the highest thermal enhancement, particularly at lower flow rates ($Re < 4400$). Under these conditions, the dual twisted-tape insert exhibited a 14% increase in thermal efficiency and a 372% enhancement in the Nusselt number compared to the plain tube. Abidi *et al.* [29] performed a numerical analysis to assess the thermal efficiency of a PTC receiver integrated with twisted-tape inserts containing circular holes, as shown in Figure 2.4. This study examined three hole diameter-to-tape width ratios (d/W = 0.5, 0.7, and 0.9) at Reynolds numbers of 10,000, 20,000, and 30,000.
The results indicated that the integration of twisted tapes featuring circular holes markedly improved the heat transfer rate in comparison to a smooth absorber tube.

2.1.2 Wire coils

Saini *et al.* [30] investigated the use of a helical wire coil flow insert in the receiver tube of a PTC to enhance its thermal performance. A three-dimensional computational fluid dynamics (CFD) model developed in

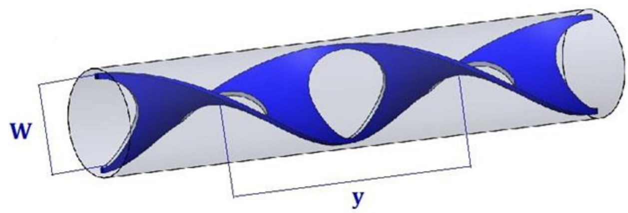

FIGURE 2.4: PTC receiver tube with twisted tape with circular holes [28].

ANSYS was employed to compare the thermal and exergy characteristics of the PTC with and without the wire coil insert. The analysis considered inlet fluid temperatures ranging from 303 K to 603 K and volumetric flow rates between 50 and 250 L/min. Results indicated that the wire coil insert significantly enhanced heat transfer and energy efficiency while requiring only a minor increase in pumping power. At an inlet temperature of 303 K and a flow rate of 50 L/min, the overall, exergy, and thermal efficiencies improved by 2.07%, 2.1%, and 2.2%, respectively. Sahin *et al.* [31] examined the thermal performance of a parabolic trough collector (PTC) receiver enhanced with coiled wire turbulators of different pitch distances. Using both experimental measurements and three-dimensional CFD simulations for Reynolds numbers ranging from 3000 to 17,000, they evaluated the influence of wire coil inserts on heat transfer and friction characteristics. The results showed that the Nusselt number increased by 2.28, 2.07, and 1.95 times compared to a smooth receiver tube for coil pitches of 15, 30, and 45 mm, respectively.
Yilmaz *et al.* [32] numerically analyzed the effect of wire coil inserts on the thermal performance of a parabolic trough collector (PTC) receiver operating under non-uniform heat flux, as shown in Figure 2.5 a. A wire coil was modelled, and realistic heat flux distributions obtained from Monte Carlo ray tracing were applied to a CFD model with temperature-dependent fluid properties. Wire coil inserts of triangular cross-section and varying pitches (0.076–0.152 m) and widths (0.03–0.036 m) were examined. The inclusion of wire coils significantly enhanced fluid mixing and disrupted the thermal boundary layer, reducing absorber wall temperatures and improving heat transfer by up to 183%. Thermal efficiency increased between 0.4% and 1.4% at flow rates below 13 m^3/h. These findings demonstrate that helical wire

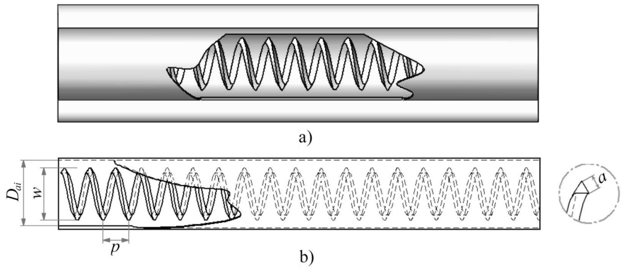

FIGURE 2.5: a) Wire coil insert in the receiver tube and b) Details of insert wire [32].

coil inserts can effectively improve the thermal performance of parabolic trough solar collectors with minimal impact on pressure drop, making them a promising approach for enhancing solar thermal energy systems.

2.1.3 Porous media

Wang *et al.* [33] numerically investigated the influence of inserting metal foam into the receiver tube of a PTC on heat transfer and thermo-hydraulic performance. The study analyzed the effects of foam placement (top or bottom) of the inner tube, geometric parameter ($H = h/D$, height of the metal foam/inner tube diameter), and porosity on flow resistance, heat transfer, and overall performance under non-uniform heat flux conditions. Results indicated that when the metal foam was positioned at the bottom, the Nusselt number increased by approximately 5–10 times while the friction factor rose by 10–20 times, yielding a performance evaluation criterion (PEC) between 1.4 and 3.2. When placed at the top, the Nusselt number improved by 10–12 times, though with a much higher friction increase (400–700 times), and a PEC between 1.1 and 1.5. Furthermore, the maximum circumferential temperature difference on the receiver outer surface decreased by nearly 45%, reducing thermal stress.

Ebadi *et al.* [34] examined the thermal and hydraulic efficiency of a PTC receiver partially filled with metallic Raschig ring porous inserts, as shown in Figure 2.6. The researchers used three-dimensional CFD simulations to analyze two filling configurations, lateral and central, under realistic, non-uniform solar flux conditions. The partially filled porous sections were

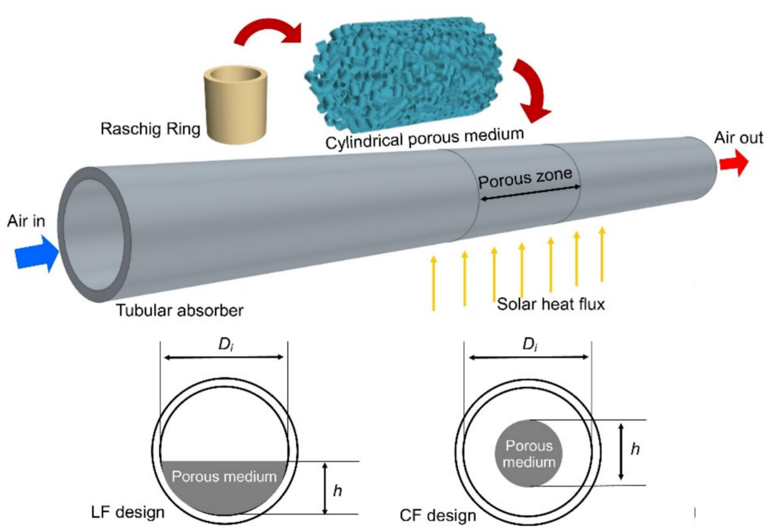

FIGURE 2.6: Porous media in the receiver tube [34].

designed to enhance heat transfer while minimizing pressure drop, a significant issue with fully filled porous receivers. Both configurations mixed the fluids well and improved heat transfer through the walls. Compared to fully filled designs, partial filling reduced the pressure drop by up to 95%, increased energy efficiency by up to 40%, and increased exergy efficiency by nearly 90%. These results demonstrate that partially filling porous receivers is an effective method for enhancing the thermal performance and overall efficiency of high-temperature solar collectors while reducing flow resistance.

Peng *et al.* [35] introduced a novel metal foam architecture, termed gradient metal foam (GMF), within the receiver of PTC. An experimental and numerical study was conducted to compare PTC outcomes with GMF, uniform metal foam (UMF), and a transparent receiver. The GMF foam consisted of two copper foam layers (inner and outer) with a pore density gradient of 5 PPI and 40 PPI and porosities of 0.9 and 0.98, respectively. PTC performance was evaluated by considering the impact of porosity and pore density gradients on the Nusselt number, friction factor, entropy generation, and energy efficiency. SYLTHERM 800 was used as the heat transfer fluid and exhibited a Reynolds number between 200,000 and 1,000,000. The research indicated that the GMF enhances the PTC's thermal performance, increasing the Nusselt number and Performance Evaluation Criteria by 43.7% to 812.6% and from 1.5 to 3.6, respectively. This is accompanied by a factor of 4.2 to 16.7 increase in the friction factor compared to a transparent receiver. Peak exergetic efficiency improved by 24.4%, and entropy generation decreased by 92.6% at a low Reynolds number of 2×10^5 with pore densities of 40 PPI and 5 PPI and an overall porosity of 0.9. Ultimately, GMF outperforms UMF, as evidenced by the subsequent results. Performance assessment criteria and exergetic efficiency improved by 66.4% to 227.3% and 12.8% to 33.3%, respectively, while entropy generation decreased by 22.4% to 60.2%. Overall, the findings demonstrated that the geometric layout of the metal foam has a more pronounced impact on heat transfer enhancement than porosity, and that metal foam inserts effectively improve the thermal performance and temperature uniformity of PTC receivers.

2.1.4 Rings

Ahmed and Natarajan [36] examined the implementation of internal toroidal rings within the receive tube of a PTC to enhance its thermal efficiency, as shown in Figure 2.7. They numerically examined nine distinct receiver configurations under fully developed turbulent flow conditions using the realizable k–ϵ turbulence model with enhanced wall treatment in ANSYS FLUENT. They methodically investigated the impact of altering the toroidal ring diameter ratio (H) and pitch size (p) on heat transfer and fluid flow properties across various inlet temperatures and flow rates of the heat transfer fluid (HTF). The results showed that the receiver with H = 0.88 and p = 2*inner tube diameter had the greatest thermal efficiency, while the setup with H = 0.92 and p = 2d had the greatest energy efficiency. At an input temperature of 600 K, the thermally and energy-efficient configurations increased the Nusselt number by 2.33 and 1.49 times and the total efficiency by 3.74% and 1.88%, respectively, compared to the smooth receiver tube. These results suggest that toroidal ring inserts can significantly improve convective heat transfer and thermal efficiency in PTC receivers while maintaining satisfactory hydraulic performance.

Ghasemi and Ranjbar [37] conducted a numerical analysis using ANSYS Fluent to investigate the effects of integrating porous rings into the absorber tube of a parabolic trough collector. The study examined several ring spacings and ring-to-receiver diameter ratios to evaluate their effect

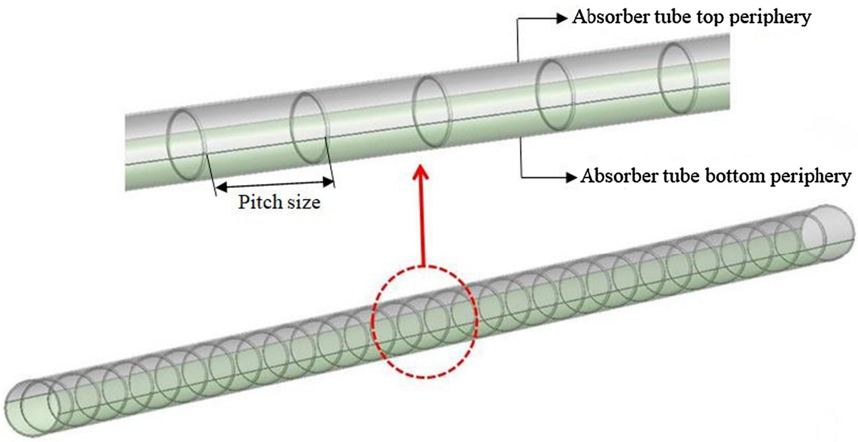

FIGURE 2.7: Receiver tube with toroidal rings [36].

on thermal performance. Three-dimensional simulations were performed under steady-state circumstances using SYLTHERM 800 as the heat transfer fluid, with Reynolds numbers ranging from 30,000 to 251,000. The results indicated that the porous rings significantly enhanced convective heat transfer; as the Reynolds number increased, the Nusselt numbers increased from 374.6 to 1766, while the smooth tube's values rose from 229.46 to 1286.37.

2.1.5 Nanofluids

Nanofluids have also been extensively explored for heat transfer enhancement in PTC receivers [38–45]. For example, Talem *et al.* [41] achieved a peak thermal efficiency of 50% using Au nanoparticle-based oil nanofluids. Panja *et al.* [43] reported efficiencies of 59.75% and 62.96% with Al_2O_3 and CuO nanofluids, respectively. Mohan *et al.* [45] demonstrated that Fe_3O_4 nanofluids could enhance thermal efficiency by 72.9%, outperforming conventional water-based systems. The combination of the two techniques mentioned above, i.e., turbulators or extended surfaces and the use of nanofluids, has also been investigated in the literature [46–48]. Recent advancements have focused on the synergistic effects of optimizing the formulation of nanofluids and the geometry of PTC receivers, as described by Rashid *et al.* [49]. Their comprehensive review of studies revealed that hybrid nanofluids (HNFs)—mixtures of two or more nanoparticles in a base fluid—can outperform mono nanofluids in parabolic trough collectors. Hybrid nanofluids such as Al_2O_3–Cu/H_2O, MWCNT–Al_2O_3/H_2O, and Au–Cu/engine oil can increase thermal efficiency by 22% to 35% compared to water and, in some cases, by up to 197%. This improvement depends on the composition of the nanoparticles and the flow regime. Rashid *et al.* also stated that altering the geometry, such as by adding twisted tapes, fins, wavy or grooved absorber tubes, and turbulators, can increase the Nusselt number by 30–75%; however, it will also result in a slight increase in pressure. The review emphasized that combining hybrid nanofluids with optimized receiver geometries yields the best thermal-hydraulic performance and energy/exergy efficiencies, which are usually 20–60% higher than those of regular fluids. However, the authors pointed out major problems such as agglomeration of nanoparticles, increased pumping power requirements, and high preparation costs. They called for more research on eco-friendly base fluids, long-term stability studies, and cost-effective synthesis methods to enable the use of these materials in solar thermal plants.

Additionally, nanofluids have been examined in various solar thermal systems, including direct absorption solar collectors (DASCs), in which the working fluid directly absorbs incident radiation rather than relying on a coated absorber surface. Berto *et al.* [50] conducted experimental research on carbon-based nanofluids containing single-wall carbon nanohorns (SWCNHs) in a volumetric solar receiver and attained optical and thermal efficiencies between 88% and 92%. Their study demonstrated that nanofluids can significantly enhance the photo-thermal conversion process by facilitating the absorption of solar energy and the movement of heat within the fluid. However, the study also revealed significant issues, such as agglomeration, sedimentation, and deposition of nanoparticles on receiver surfaces at higher particle concentrations. These issues negatively impacted long-term stability. To maintain stable thermal performance, the authors recommended optimizing nanoparticle concentration, improving synthesis methods, and ensuring material compatibility (e.g., avoiding the use of copper parts). These findings are particularly relevant to parabolic trough receivers (PTRs) because stable nanofluid suspensions can significantly improve convective heat transfer and thermal efficiency during continuous high-temperature operation.

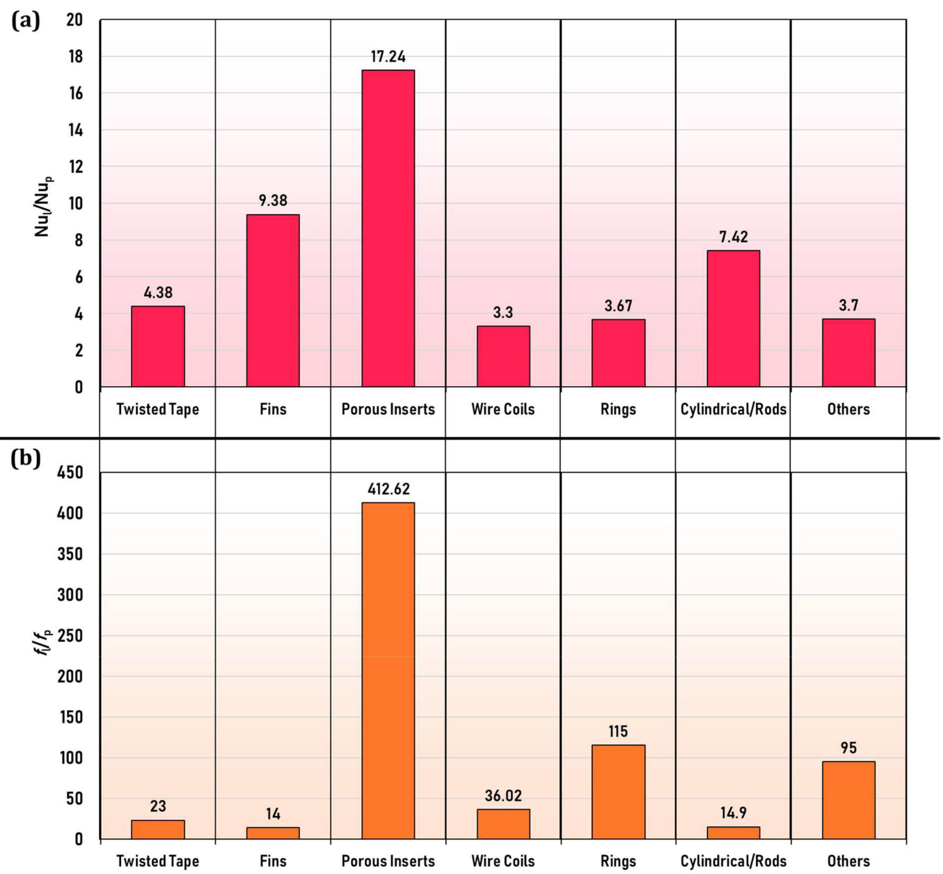

FIGURE 2.8: Reviewed data analysis by [14] of maximum recorded values. (a) Nu number ratio (b) Friction factor ratio.

In conclusion, despite extensive research on various passive heat transfer enhancement methods, such as twisted tapes, wire coils, rings, porous inserts, and the use of nanofluids, significant challenges remain in optimizing the thermal-hydraulic performance of parabolic trough receivers. As quantitatively summarized by Allam *et al.* [14] (Fig. 2.8), porous inserts provide the highest reported heat transfer enhancement, with a maximum Nusselt number ratio (Nu/Nu_p) of 17.24. However, this improvement is accompanied by an extremely high friction factor ratio ($f/f_p = 412.62$), indicating a severe pumping power penalty.

In contrast, longitudinal fins achieve a comparatively high maximum Nu/Nu_p ratio of 9.38 while maintaining a much lower friction factor ratio (maximum reported value of 14). This places fins among the most balanced enhancement techniques in terms of thermal gain versus hydraulic penalty. Twisted tapes and wire coils exhibit moderate heat transfer enhancement but generally introduce higher friction penalties relative to fins.

These quantitative comparisons clearly illustrate the classical trade-off between convective enhancement and pressure drop. While porous media offer superior thermal augmentation, their excessive friction penalties limit their practical implementation in high-temperature PTC systems. Longitudinal fins, on the other hand, provide a favorable compromise, offering significant heat transfer enhancement with comparatively moderate hydraulic losses. This balance justifies the focus of the present thesis on optimizing fin geometry and placement to further improve thermal performance under realistic operating conditions.

2.1.6 Longitudinal finned in PTC Receivers

Internally finned tubes were extensively studied under the assumption of a uniform temperature boundary condition. Just to mention a few works, Edwards et al. [51] experimentally investigated the turbulent flow in longitudinally finned tubes and collected data on the friction factor. In the experimental study by Jensen and Vlakancic [52], the influence of fin geometry on heat transfer and pressure drop was investigated, and new correlations for finned tubes were developed. Liu and Jensen [53] analyzed the effect on friction factor and Nusselt number of longitudinal fins with rectangular, triangular, and round crest profiles, as well as helical fins.

As mentioned earlier, PTC receiver tubes are subjected to a non-uniform heat flux, resulting in non-uniform circumferential temperatures. In contrast, simpler solutions such as longitudinal fins offer high thermal performance with minimal pressure drop. The use of internal fins with conventional heat transfer fluids has been widely investigated as a means to enhance thermal performance in PTCs, with numerous studies reporting significant improvements, as shown in Figure 2.9.

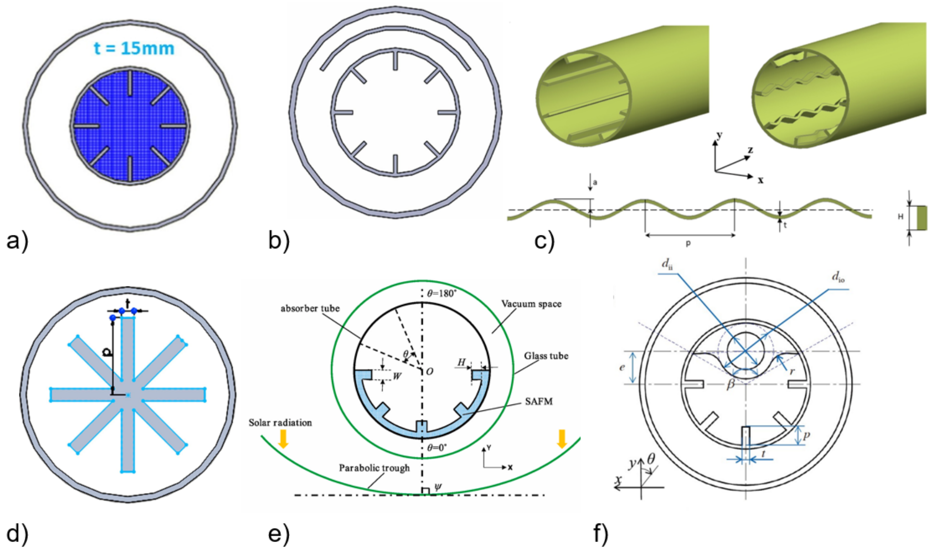

FIGURE 2.9: Different finned receivers: a) [54], b) [55], c) [56], d) [57], e) [58], and f) [59].

The use of pin fin arrays in receiver tubes was investigated by Gong *et al.* [60]. Their research found that the use of pin fins increased the Nusselt number by 9%, and the overall thermal performance by 12%. In [61], longitudinal vortex generators (LVGs), like pin fins, in the bottom inner side of the parabolic trough receiver tube were analyzed numerically. The effects of the HTF mass flow rate, HTF inlet temperature, and different dimensions of LVGs were examined. The conclusion was that the use of LVGs could reduce thermal losses by between 1.35% and 12.1%. Bellos *et al.* [54] conducted a numerical parametric study on internally finned receivers, as shown one of the case in Figure 2.9a, analyzing twelve configurations with varying fin lengths (5–20 mm) and thicknesses (2–6 mm). The optimal configuration, i.e., fins 10 mm high and 2 mm thick, reduced the mean circumferential temperature by 20%, increased thermal efficiency by 0.82%, and enhanced the Nusselt number by a factor of 1.652 compared to a smooth tube. Bellos and Tzivanidis [55] studied internal fins along with some optical techniques (reflector shield) to enhance thermal efficiency, as shown in Figure 2.9b. Though reflector shields decrease optical efficiency, combined internal fins and reflector shields lead to increased thermal efficiency. This technique is suitable for higher operating temperature conditions, and improves the thermal efficiency by 2.41%, and decreases the temperature difference by 23 K. The effect of longitudinal fins and sinusoidal lateral surfaces in parabolic receiver tubes was numerically investigated by Kurşun [56], as shown in Figure 2.9c. Syltherm oil 800 was used as HTF, with an inlet temperature varying from 300 to 600 K and a Reynolds number range of 20,000 to 80,000. The Nusselt number increased by 78% for sinusoidal fins and by 25% for flat fins. By using sinusoidal fins, the temperature difference was reduced by 48 K for the fluid inlet temperature of 500 K. In [57], a CFD analysis was conducted using SolidWorks Flow Simulation to examine the impact of a star fin insert (see Figure 2.9d) on the overall performance of the PTC. The fin height varies from 15 to 30 mm, and the fin thickness ranges from 2 to 5 mm. They assessed the model based on various parameters, including the PTC's thermal efficiency, exergy efficiency, and overall efficiency. The input temperature and Reynolds number were selected to range from 400 K to 650 K and from 4,000 to 100,000, respectively, using SYLTHERM 800 as the heat transfer fluid. The Nusselt number and heat transfer coefficient increased by 60%, while heat losses decreased by 14%. However, the pressure drop and friction factors increased by 900%. Peng *et al.* [58] numerically examined the integration of semi-annular and finned metal foams into a PTC receiver to enhance heat transfer efficiency, as shown in Figure 2.9f. Three fin geometries—rectangular, triangular, and trapezoidal—each measuring 16 mm in height, were examined, with widths of 2.4, 3.4, and 4.8 mm, respectively. The semi-annular and fin sections had a porosity of 0.5 and pore densities of 5 and 40 PPI, respectively. Using SYLTHERM 800 oil under non-uniform heat flux conditions with Reynolds numbers ranging from 200,000 to 1,000,000, the results showed significant improvements compared to a conventional receiver. The Nusselt number increased by 256.3% to 838.7%, exergy efficiency improved by 2.2% to 10.1%, and the friction factor increased by 440.3% to 788.8%. Concurrently, entropy generation decreased by 64.2% to 93.3%, and the performance criteria ranged from 2.1 to 4.6. Triangular fins demonstrated the highest overall performance among all options, and hybrid configurations surpassed individual foam or fin arrangements.

Liu *et al.* [59] conducted a numerical investigation on a novel finned parabolic trough receiver with an inner tube (FPTR-IT) aimed at improving thermal efficiency and enabling solar cascade heat collection, as shown in

Figure 2.9e). The proposed design integrates straight internal fins and an eccentric inner tube into a conventional parabolic trough receiver. The fins enhance convective heat transfer in the lower region of the absorber subjected to high concentrated heat flux, while the inner tube carries low-temperature water to reduce absorber temperature in the upper directly irradiated region and suppress negative thermal-flux phenomena. This technique reduces the temperature gradient in the receiver and increases the velocity gradient near the heated surface. The results show that this design enhances the Nusselt number by 2.28 times, while the maximum temperature drops up to 93.9 K. Laaraba and Mebarki [62] showed that fin height plays a more significant role than the thickness. In their analysis, five internal fins were added on the bottom side of the receiver. The analysis of the velocity field showed that fins cause a 24.55% increase in fluid velocity compared to the smooth receiver; however, the maximum velocity shifted toward the upper (cold) side, which represents a drawback. The results revealed that the thermal efficiency improved by 8.45%.

2.2 Thermal Loss Mechanisms in Receivers

The growing adoption of parabolic trough collector (PTC) technologies in commercial solar thermal energy applications drives the need for accurate receiver modeling to optimize thermal efficiency, minimizing heat losses, and enhance operational reliability of this type of system.

The receiver is one of the most critical components of a PTC and is susceptible to performance degradation and damage. Over time, helium gas from the atmosphere could diffuse through the glass tube, increasing heat losses by up to 20% [63]. When vacuum is lost, the receiver experiences twice the normal heat loss. If the glass envelope is broken, the heat loss could be 4 to 10 times greater than that of an undamaged receiver, largely depending on wind conditions. Degradation of heat transfer fluids (HTFs) at high temperatures generates hydrogen gas, which slowly permeates through the absorber wall into the annular space, causing heat losses four times higher compared to those with a good vacuum [5, 6, 64]. Receiver failure rates were discussed in [11, 65] to understand future trends, address operation and maintenance issues, and develop new designs with improved performance.

Over the past decade, extensive research has been conducted to enhance the performance of PTC systems, primarily by addressing heat losses that significantly impact efficiency and sustainability. Many studies have explored a wide range of factors, including geometrical design, receiver coatings, vacuum pressure, HTF flow and temperature, and ambient conditions such as wind velocity, to better understand and mitigate heat loss. A comprehensive literature review on heat losses in PTC receivers can be found in [16, 66]. In the following subsections, relevant studies are divided into two main categories: experimental and numerical analyses.

2.2.1 Experimental analysis

In laboratory heat loss measurements, Burkholder *et al.* [67] conducted an experimental study at the National Renewable Energy Laboratory (NREL) to quantify the off-sun, steady-state thermal losses of the PTC receiver using a electric-resistance testing apparatus. The study evaluated two commercial receivers, the Solel UVAC2 and the Schott PTR70. Experiments were conducted at absorber temperatures between 100°C and 450°C. The results revealed that the UVAC2 and PTR70 had comparable heat losses of approximately 370 W/m at 400°C. Loreto *et al.* [68] examined the effects of hydrogen infiltration into the evacuated annulus of parabolic trough solar receivers, as shown in Figure 2.10. Utilizing the HEATREC electric-resistance heating test platform at PSA-CIEMAT, they evaluated heat losses on standard PTR®70 Gen 2 tubes under two conditions: with an intact vacuum and following hydrogen doping of the annulus at approximately 1 mbar, covering absorber temperatures ranging from 100°C to 400°C. Their findings indicate that, in the presence of hydrogen, heat losses escalated significantly—from approximately 211 W/m under vacuum to approximately 867 W/m at 400°C—representing an increase of up to four times. The authors ascribe this to improved conductive heat transmission via the gas-filled annulus (Knudsen effect) and highlight that hydrogen ingress significantly impairs the thermal efficiency of receivers. They conclude that regulating hydrogen production and buildup is essential for sustaining efficiency in solar trough plants. In [69], laboratory heat loss tests were conducted on Schott's 2008 PTR70 parabolic trough receiver at receiver surface temperatures ranging

FIGURE 2.10: Experimental setup of receiver for heat loss measurement [68].

from 100 °C to 500 °C. Figure 2.11 shows the heat loss that occurs in the system. They observed that the receiver exhibited significantly lower heat losses compared to previous receiver designs, primarily due to improvements in the receiver's selective coating. At operating temperatures around 400 °C, the measured heat loss was approximately 190 W/m, representing a notable reduction compared to older receiver designs.

Burkholder and Kutscher [70] evaluated Solel's UVAC3 receiver, developing heat loss correlations based on absorber and ambient temperature differences. Lei *et al.* [71] introduced a new test stand and methodology to measure overall and end losses, demonstrating that end losses become more significant at lower operating temperatures. Marquez *et al.* [72] further contributed to the experimental characterization of receiver heat losses, focusing on the annulus region and resistance heating techniques. Setien *et al.* [73] presented a methodology to analyse the influence of partial vacuum pressures in the heat losses of PTC receivers, considering air as an incoming gas. Utilising infrared thermography, the approach

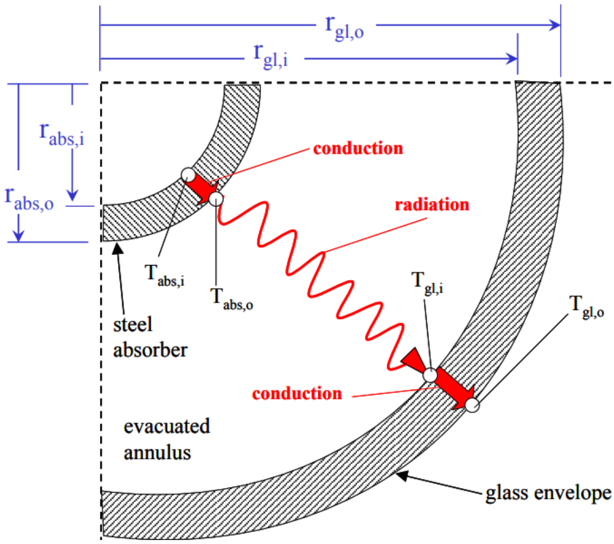

FIGURE 2.11: Schematic of 1-dimensional heat loss [69].

enables noninvasive measurement of glass envelope temperatures, facilitating the detection of vacuum degradation. They measured a significant increase in glass cover temperature when the vacuum is completely lost (air pressure $= 10^3$ mbar) compared to when there is only a partial loss (10^{-4} mbar $<$ air pressure $< 10^2$ mbar), regardless of the receiver temperature. Furthermore, several studies have used infrared thermography to evaluate the performance of receivers and detect faults in PTC fields. Caron and Röger [74] performed in-situ receiver heat-loss measurements through transient infrared thermography, providing valuable insights into local temperature variations and vacuum degradation. Carra *et al.* [75] investigated the influence of measurement parameters on vacuum level assessment in PTC receivers, improving the accuracy of thermographic diagnostics. Oufadel *et al.* [76] integrated infrared imaging with artificial intelligence methods to estimate receiver heat losses in real operating conditions. This concept was further developed in [77] by applying a meta-learning framework with hypernetworks for efficient and scalable fault detection. Likewise, Price *et al.* [7] conducted an early field investigation to evaluate receiver performance and identify thermal anomalies under practical operating conditions. Figure 2.12 shows the relationship between receiver thermal losses, the difference between HTF and ambient temperature, and the condition of the receiver annulus. As can be seen, helium slightly increases thermal losses in the annulus, but not nearly as much as air or hydrogen do. The glass envelope temperature can also be determined using the receiver model.

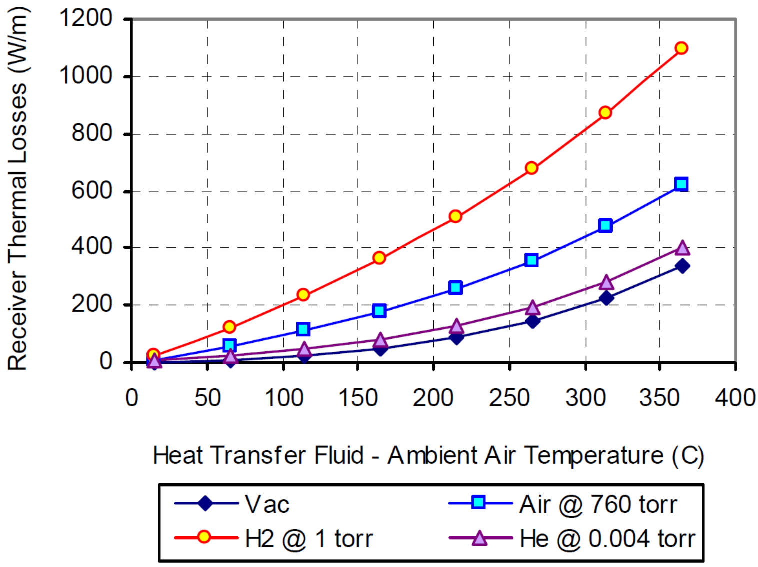

FIGURE 2.12: Receiver thermal losses as a function of fluid temperature and annulus condition [7].

Heat losses are directly proportional to the temperature of the glass. Under a given ambient condition, the glass temperature depends on the heat transfer mechanisms in the annulus. As vacuum pressure increases, conduction and natural convection heat transfer in the annulus also increase. Additionally, if gases with higher thermal conductivity than air - such as hydrogen, which has seven times the thermal conductivity of air - enter the annulus, they further enhance conduction and convection, resulting in an increased glass temperature. Hence, vacuum loss, by any means, can be detected using temperature sensors, as shown in [78]. Glatzmaier [79] developed and tested a hydrogen measurement and extraction process at the Nevada Solar One (NSO) PTC solar power plant. An integrated sensor/separator system was installed to simultaneously measure hydrogen partial pressure and extract hydrogen from the headspace gas in the HTF expansion vessels. This system, based on a palladium/silver membrane design, allowed real-time monitoring of hydrogen levels without intrusive modifications to the plant. The technology was jointly developed by NREL and Acciona Energy and was then installed at full-scale at NSO.

2.2.2 Numerical studies

One of the first one-dimensional thermal models of PTC receivers was developed by Forristall [80]. He set up a heat transfer model using Engineering Equation Solver (EES) to simulate the thermal behavior of PTC receivers, incorporating detailed thermodynamic and optical properties. Padilla *et al.* [81] conducted a one-dimensional numerical analysis of receiver heat transfer, validating their model with experimental data from Sandia National Laboratories. Kalogirou [82] presented a comprehensive thermal model that accounted for conduction, convection, and radiation losses, implemented in EES and validated against existing collector performance. Wu *et al.* [83] performed a three-dimensional transient simulation using CFD and Monte Carlo ray-tracing, revealing detailed temperature distributions and the impact of fluid velocity on thermal gradients. Guo *et al.* [84] examined the thermal and exergy efficiencies of a parabolic trough solar receiver using first- and second-law thermodynamic analyses. Their research revealed that convective heat loss from the glass cover primarily causes thermal loss, while exergy destruction is primarily caused by losses at the receiver end. The researchers determined an ideal mass flow rate that maximizes exergy efficiency and observed that thermal and exergy efficiencies exhibit inverse patterns under different operating conditions. Their findings showed that optical heat losses considerably surpass those of the receiver, especially at high sun angles, highlighting the importance of improving optical performance. The authors concluded that selecting suitable assessment criteria — whether thermal or exergy efficiency — is essential for optimizing the design and operational parameters of parabolic trough solar systems. Lei *et al.* [85] conducted a comprehensive 2-D numerical investigation of conduction and radiation heat losses in the vacuum annulus of parabolic trough receivers, as shown in Figure 2.13. They employed the Direct Simulation Monte Carlo (DSMC) method to simulate rarefied gas dynamics. The researchers examined the impact of annulus

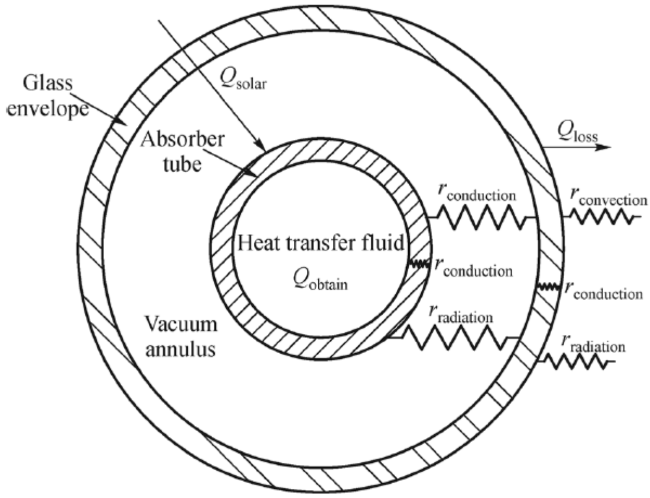

FIGURE 2.13: Heat transfer model of the receiver and heat transfer model of the vacuum annulus [85].

pressure, gas composition, absorber temperature, and annulus shape on overall heat loss. Their findings revealed that conduction heat loss increases as the vacuum deteriorates. Hydrogen and helium were identified as the most significant gases due to their high diffusivity and thermal conductivity. The study showed that, at pressures under 1 Pa, total heat loss is primarily radiative. However, at higher pressures (over 100 Pa), conduction dominates, increasing total heat loss by up to five times. Furthermore, it was found that reducing the emittance of the selective coating while maintaining a larger annulus gap can considerably minimize heat loss, particularly in cases of partial vacuum failure.

2.3 Summary of Literature and Research Gaps

Longitudinal fins have demonstrated strong potential for thermal enhancement of PTC receivers. Previous studies have demonstrated the influence of geometric parameters, such as fin height, width, and number, on the thermal performance of PTC receivers. However, these investigations have primarily considered fins with the same height, symmetrically distributed along the receiver circumference. Nevertheless, most studies have focused on geometric parameters such as height and width, with limited attention to fin placement. Given the non-uniform heat flux distribution around the receiver circumference, fin positioning could significantly influence thermal gradients. This aspect remains underexplored. Bellos *et al.* [86] conducted one of the few studies addressing this issue, showing through multi-objective optimization that placing three fins on the lower half of the receiver yielded the highest efficiency gain (0.51%), whereas fins on the upper half had a negligible impact.

This thesis introduces and systematically evaluates a novel configuration involving asymmetrically distributed longitudinal fins, varying in both height and position, tailored to the circumferential non-uniform heat flux distribution. To address an additional research gap, this work examines the distinct heat transfer mechanisms associated with fins located on the upper and lower halves of the receiver tube, which are predominantly exposed to direct and reflected solar radiation, respectively. Finally, a new performance evaluation criterion is proposed, based on the external surface temperature of the receiver tube, in contrast to the internal surface temperature commonly used in existing literature.

As is evident from the literature, heat losses in PTC receivers depend directly on absorber and glass tube temperatures, ambient and geometrical parameters, receiver emissivity, annulus vacuum pressure, and HTF inlet temperature, and indirectly on HTF mass flow rate [16, 87]. Extensive research has been conducted on thermal performance under various conditions, and many studies have focused primarily on theoretical models or laboratory experiments using a constant receiver tube temperature without considering HTF flow rate or real operating conditions. In a PTC solar field, receiver tubes are subjected to non-uniform heat flux, and very few studies examine the thermal performance under real operating conditions. Although previous studies have examined receiver heat losses, most have either treated the annulus region in isolation or assumed ideal conditions, ignoring the presence of hydrogen and the effects of outdoor winds.

The main outcome of this PhD research will be a detailed CFD-based thermal analysis of a PTC receiver, considering realistic scenarios involving a vacuum atmosphere at different pressures in the annulus space between the absorber and the glass tube. While the baseline simulations will be conducted under no-wind conditions to isolate the effects of internal flow and annulus properties, the influence of wind-induced forced convection on the external glass envelope will also be investigated. By capturing the coupled effects of conduction, convection, and radiation heat transfer under these conditions, the model will offer an accurate prediction of heat losses and thermal behavior of the receiver. The results not only will deepen the understanding of thermal performance in degraded vacuum conditions but will also provide practical insights for PTC field operators.

Chapter 3

Numerical Modelling of the PTC Receiver

This chapter describes the numerical modelling and computational techniques used to simulate the thermo-hydraulic performance of a PTC receiver system. It outlines the procedures for creating a three-dimensional (3D) computational fluid dynamics (CFD) model to predict the flow dynamics, temperature distribution, and thermal efficiency of the receiver under realistic conditions.

3.1 1D and 3D numerical approaches

A PTC receiver's performance can be analyzed using analytical, experimental, or numerical methods. Analytical models are typically based on one-dimensional energy balance equations, which provide an approximate estimate of the receiver's performance. Although these models are computationally efficient, they often oversimplify complex physical phenomena, such as non-uniform solar flux distribution, radiative losses, and convective heat transfer between the receiver tube and glass envelope.

Although experimental investigations are precise and realistic, they are often limited by high costs, lengthy testing periods, and environmental uncertainties. In contrast, numerical modelling using computational fluid dynamics (CFD) offers a versatile, economical, and thorough approach to understanding the coupled effects of flow, heat transfer, and radiation in PTC systems.

Depending on the complexity and objectives of the study, researchers employ different levels of numerical modelling:

3.1.1 One-dimensional models

One-dimensional (1D) numerical models are simplified representations that assume uniform properties along the circumference of the receiver and evaluate the energy balance along its length. These models are widely used to estimate collector efficiency, heat loss, and temperature distribution while maintaining a balance between computational simplicity and physical accuracy.

Forristall [80] developed a significant 1D heat transfer model for parabolic trough receivers at NREL using the Engineering Equation Solver (EES) software. The model included detailed energy balances for the absorber, the glass envelope and the annulus, and accounted for all three main mechanisms of heat transfer: conduction, convection and radiation. Empirical correlations for Nusselt numbers and friction factors were used to make accurate predictions of thermal performance, which were then checked against the LS-2 test results from Sandia National Laboratories. Padilla *et al.* [81] improved upon this methodology by numerically solving the steady-state energy and mass balance equations for several axial segments of the receiver. Their one-dimensional model accounted for the radiative heat transfer between the absorber and glass surfaces. The model also examined alternative annulus conditions, including air and vacuum. The model's results were in good agreement with the experimental data, demonstrating its usefulness for design and optimization studies of parabolic trough systems. Kalogirou [82] developed a one-dimensional, steady-state, numerical model of a PTC receiver using the EES software, as shown in Figure 3.1. This model applies energy balance equations across the receiver's cross-section, demonstrating how heat transfer occurs through a network of thermal resistances. Newton's law of cooling governs internal convection; Fourier's law governs conduction through the receiver and glass walls; and Stefan–Boltzmann's law governs radiative exchange. The Gnielinski correlation was used for turbulent flow inside the receiver, the Raithby and Holland correlation for natural convection in the annulus, and the Churchill–Chu and Zhukauskas correlations for external convection under natural and forced conditions. The model calculates the Nusselt, Rayleigh, and Prandtl numbers to determine the heat transfer coefficients. Zaversky*et al.* [88] developed a 1D transient finite-volume Modelica model for systems that operate with molten salt as the heat transfer fluid. This model can dynamically simulate thermal transients in the receiver and heat transfer fluid, making it ideal for system-level simulations and control studies. Cheng *et al.* [89] created a one-dimensional, non-uniform thermal

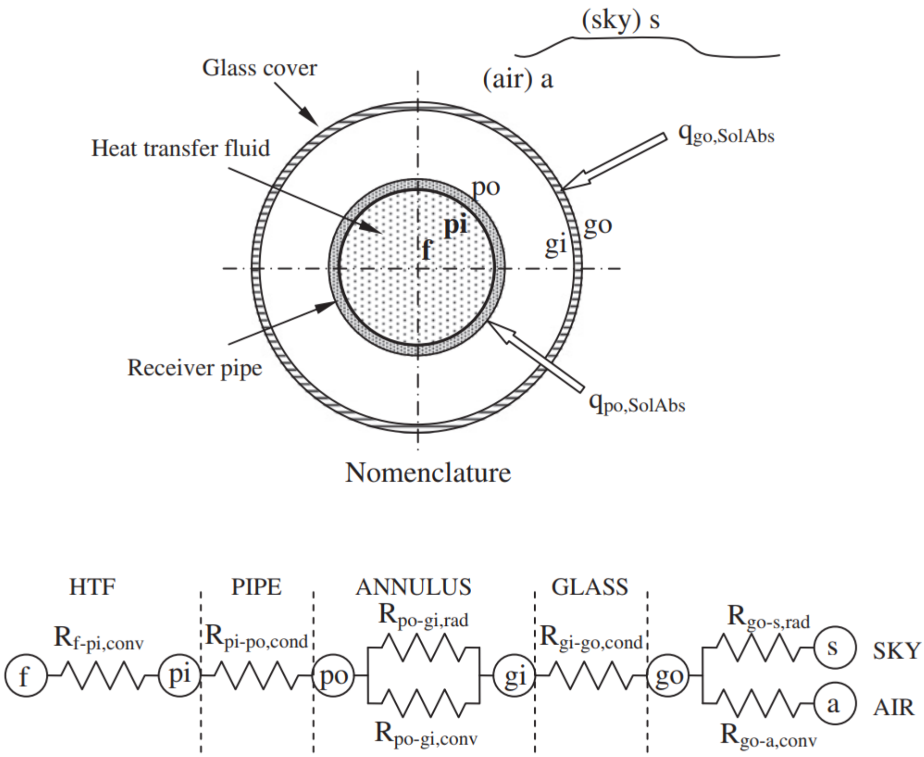

FIGURE 3.1: Collector receiver model; nomenclature and thermal resistance network for the cross-section of the receiver [82].

model of a parabolic trough solar receiver. They achieved this by splitting the receiver into two linear halves (one irradiated and one non-irradiated) and two inactive ends. This model captures local changes in solar flux and heat transport. It uses temperature-dependent properties and the correct correlations for different flow regimes, including energy balances for conduction, convection, and radiation. Written in Fortran and solved iteratively, the model is computationally faster than complicated three-dimensional CFD models. The model was tested against data from the LS-2 collector at Sandia National Laboratories and performed well in both on-sun and off-sun conditions.

Despite their usefulness and computational efficiency, one-dimensional thermal models have intrinsic limitations. They usually assume that the temperature, heat flux, and thermophysical properties are uniform across the receiver's perimeter. However, this assumption does not accurately represent the actual non-uniform distribution of solar radiation. The bottom section of the receiver facing the mirror receives substantially more solar radiation than the top section. This results in asymmetric temperature distributions and uneven heat transfer, which one-dimensional models cannot adequately represent. While this simplification yields modest errors for small-scale collectors or average performance estimations, it limits the model's ability to depict local heat effects and complex flow dynamics.

3.1.2 Three-dimensional models

Three-dimensional (3D) conjugate CFD models represent the most comprehensive numerical approach for investigating the thermal and hydraulic behaviour of parabolic trough collector (PTC) receivers. Unlike reduced-order models, 3D CFD can explicitly take into account: (i) the non-uniform circumferential distribution of solar heat flux; (ii) temperature asymmetries and local hot-spot formation; (iii) secondary flow structures induced by asymmetric heating or internal enhancement devices; and (iv) coupled radiative, conductive, and convective heat losses through the annulus, particularly under degraded vacuum conditions or in the presence of hydrogen or other gases.

Three-dimensional CFD modelling is essential for accurately capturing the complex flow and heat-transfer mechanisms induced by enhanced receiver geometries such as twisted tapes, wire coils, fins, and porous inserts. Previous studies [25, 26, 33, 54, 58] have shown that these configurations generate inherently three-dimensional swirling and multidirectional vortical structures, leading to enhanced mixing, turbulence intensification, and reduced circumferential temperature non-uniformity. The thermal–hydraulic performance was found to be strongly dependent on geometric parameters, flow conditions, and circumferential effects, which cannot be resolved using lower-dimensional models. Consequently, 3D conjugate simulations are required to properly account for non-uniform solar flux, wall conduction, and localized heat-transfer enhancement.

In the present PhD work, a three-dimensional conjugate CFD model is therefore adopted to accurately evaluate the thermo-hydraulic behaviour of the receiver under realistic operating conditions. The analysis focuses exclusively on the receiver component rather than the complete parabolic trough system, enabling a detailed investigation of: (i) non-uniform circumferential solar flux; (ii) fin-enhanced internal heat transfer; and (iii) heat-loss mechanisms associated with vacuum degradation and hydrogen ingress.

3.1.3 Computational Domain and Modelling Strategy

This thesis focuses solely on the computational domain of the receiver assembly in order to analyze the thermo-hydraulic behavior of the receiver tube rather than the PTC system's overall optical performance.

This domain generally includes the HTF flow zone, the solid receiver tube, the annular space, the glass envelope, and the external air region.

3.1.4 Periodic versus Full-Length Computational Domains

In three-dimensional CFD modelling of PTC receivers, two types of computational domains are commonly used: (i) full-length receiver domains and (ii) axially periodic segments. The choice between these approaches depends not only on whether the internal geometry repeats along the axial direction, but more fundamentally on whether the hydrodynamic and thermal fields can be considered fully developed.

Periodic domains based on fully developed flow. A periodic computational domain may be used when the flow and thermal fields reach an axially fully developed state. In such cases, only a representative axial slice of the receiver needs to be modeled, with periodic boundary conditions enforcing equality of velocity, turbulence quantities, and non-dimensional temperature between the inlet and outlet of the periodic domain.

Periodic modelling is appropriate when:

- the receiver geometry is axially uniform (smooth tube or uniformly finned tube),

- the HTF thermophysical properties are independent of temperature,
- the solar heat flux is uniform in the axial direction, and
- the region of interest is sufficiently far from the inlet and outlet so that entrance effects and end losses are negligible.

This approach has been used in only a limited number of studies in the CFD literature, including:

- Mwesigye *et al.* [26] applied periodic boundaries to model a single twisted-tape pitch after demonstrating that the velocity and temperature fields become periodically fully developed downstream of the entrance region.
- Cheng *et al.* [89] employed a periodic approach to analyse the influence of longitudinal vortex generators (LVGs) once hydrodynamic and thermal development was established beyond the initial development zone.
- Yilmaz *et al.* [32] used a periodic slice for wire-coil inserts, justified by the observation that the swirling secondary flow becomes repetitive along the axial direction once full development is reached.

Although periodic domains are often associated with repeating insert geometries, the essential criterion is the establishment of fully developed behaviour, which may also occur in smooth receivers or receivers with uniform axial fin arrangements. Periodic modelling enables high-resolution simulations of complex internal flow structures while significantly reducing computational cost.

Full-length receiver modelling. A full-length computational domain is required when the flow and temperature fields do not reach a fully developed state or when axial variations are important. This includes situations where:

- inlet hydrodynamic and thermal development affect performance,
- axial variation of solar flux, HTF properties, or geometry exists,
- end losses are significant,

- non-periodic fin or insert geometries are used.

For example, full-length modelling is necessary in studies focusing on circumferentially non-uniform solar flux distributions or on global heat-loss characterisation of smooth receivers, as these phenomena generate axial temperature gradients that cannot be reproduced using periodic conditions.

3.2 Receiver Physical Configuration

This thesis focuses on the numerical analysis of a standard receiver tube designed for PTCs with a parabola aperture width of 5.76 m (LS-3 PTC design) [3], which consists of a stainless-steel receiver tube, a sealed annulus region, a surrounding glass envelope, and the flowing HTF. No optical modelling is conducted; instead, the incoming solar energy is imposed directly as a prescribed non-uniform circumferential heat flux on the outer surface of the receiver tube. This heat-flux profile is pre-computed outside the CFD model using the optical characteristics of the LS-3 collector [33]. Although no ray-tracing or optical simulation is performed within the numerical domain, the applied flux distribution already incorporates the main optical parameters of the system—including mirror reflectivity, glass transmittance, absorber absorptance, and the local concentration ratio (LCR). These parameters were used to generate a realistic circumferential flux pattern that represents the LS-3 irradiance distribution, ensuring that the thermal model receives physically meaningful solar heat flux without directly simulating the optical field. This approach allows the modelling effort to focus entirely on the receiver's coupled conduction, convection, and radiation processes. The same LS-3 receiver design is used in Chapters 4, 5, and 6, with the axial domain length and annulus behaviour adjusted according to the objectives of each specific study.

The receiver tube is fabricated from stainless steel (AISI 316/321) and has an inner diameter of 66 mm and an outer diameter of 70 mm. The external surface of the receiver tube is coated with a selective coating whose emissivity increases with temperature. Although optical reflection and absorption are not simulated, this temperature-dependent emissivity is essential for accurately predicting radiative heat losses. The axial length of the receiver model differs across chapters. In Chapter 4 and Chapter 5, where the focus is on cross-sectional thermal behaviour, fin-induced enhancement, and local heat-loss mechanisms, a short periodic domain of one tube diameter (70 mm) is used. Preliminary tests confirmed that the solution is independent of the length of the analysed periodic domain. This periodic configuration allows the study of a thermally fully developed region of the receiver at substantially reduced computational cost. In contrast, Chapter 6 models the full receiver length of 4.06 m, which is required to capture axial variations in HTF temperature, fluid properties, annulus heat transfer, and environmental heat losses.

The glass envelope surrounding the receiver tube has an inner diameter of roughly 109–114 mm and an outer diameter of 115–120 mm. The glass envelope subsequently loses heat to the ambient air by natural or forced convection and by long-wave radiation. The thermal behaviour of the glass, especially its outer-surface temperature, is highly sensitive to conditions in the annulus and becomes an important indicator of receiver performance.

The annulus between the receiver tube and the glass envelope is a crucial region in determining the overall thermal resistance of the receiver. Under ideal conditions, the annulus is evacuated to approximately 10^{-2} mbar, eliminating convection and rendering gas conduction negligible, such that radiation becomes the dominant heat-transfer mechanism across the gap. In Chapter 4, the annulus is assumed to be at atmospheric pressure, and a single value of air thermal conductivity is assigned, since the relative effect of fins on heat transfer is essentially the same at both low and high annulus pressures, allowing fin performance to be evaluated independently of annulus conditions. In Chapter 5, air in the annulus is considered over a range of pressures from near-vacuum to atmospheric conditions and modeled using an effective thermal conductivity approach. Over time, hydrogen generated from HTF degradation can permeate through the receiver tube wall and accumulate in the annulus; due to hydrogen's exceptionally high thermal conductivity, heat transfer across the annulus increases significantly, and at elevated partial pressures, buoyancy-driven laminar natural convection may also occur. For these reasons, Chapter 6 models both a vacuum annulus and a hydrogen-contaminated annulus (1 mbar) as fully active fluid domains.

Inside the receiver tube, the HTF transports absorbed thermal energy downstream. The HTF selection differs across chapters. Chapter 4 and Chapter 5 use Syltherm-800 with constant thermophysical properties evaluated at a representative temperature, enabling the isolation of geometric and local thermal effects in the periodic domain. Chapter 6 uses Therminol VP-1 with full temperature-dependent properties to capture realistic axial variations in convective heat transfer and fluid behaviour along the 4.06 m receiver.

Finally, the external ambient environment interacts thermally with the outer surface of the glass envelope through convection and long-wave radiation. In Chapters 4 and 5, only forced convection (the effect of wind) is considered, while in Chapter 6, both forced and natural convection (no wind) is considered to evaluate their effect on glass temperature and total heat loss.

Overall, the receiver assembly—comprising the receiver tube, annulus, glass envelope, HTF domain, and external environment—is modelled in full three-dimensional detail. The axial domain length is selected according to chapter objectives: periodic (70 mm) in Chapter 4 and Chapter 5, and full length (4.06 m) in Chapter 6. This provides a consistent physical basis for all the numerical analyses presented in the thesis. Further details and discussions are provided in the respective chapters.

3.3 Numerical Modelling

The numerical simulations conducted in Chapters 4, 5, and 6 are based on a three-dimensional, steady-state conjugate heat-transfer framework implemented in ANSYS Fluent. In this formulation, convection within the heat-transfer fluid (HTF) and optionally in the annulus, heat conduction inside the solid components of the receiver tube and glass envelope, and radiative heat exchange across the annular space are solved simultaneously. The governing equations for all fluid domains consist of the incompressible, steady Reynolds-Averaged Navier–Stokes (RANS) equations. The continuity equation is expressed as

$$\frac{\partial(\rho u_i)}{\partial x_i} = 0 \tag{3.1}$$

while the momentum equation for the HTF is

$$\frac{\partial}{\partial x_j}(\rho u_i u_j) = -\frac{\partial p}{\partial x_i} + \frac{\partial}{\partial x_j}\left[(\mu + \mu_t)\left(\frac{\partial u_i}{\partial x_j} + \frac{\partial u_j}{\partial x_i}\right) - \frac{2}{3}(\mu + \mu_t)\frac{\partial u_k}{\partial x_k}\delta_{ij} - \frac{2}{3}\rho k \delta_{ij}\right] + S_i \tag{3.2}$$

and the corresponding energy equation is

$$\frac{\partial}{\partial x_j}(\rho c_p u_j T) = \frac{\partial}{\partial x_j}\left[\left(\lambda + c_p \frac{\mu_t}{\sigma_{h,t}}\right)\frac{\partial T}{\partial x_j}\right] \tag{3.3}$$

The source term S_i differs among the chapters. In Chapters 4 and 5, the annulus is treated using an effective thermal-conductivity model, and no natural-convection forces arise; therefore, $S_i = 0$. In contrast, Chapter 6 includes buoyancy-driven laminar natural convection within a hydrogen-filled annulus, and the gravitational body-force term $S_i = \rho g_i$ is added to the momentum equation. Thus, buoyancy effects appear only in Chapter 6 and are absent in Chapters 4 and 5. The flow in the HTF is fully turbulent. Both the k–ϵ turbulence model with enhanced wall treatment and the k–ω turbulence model were initially tested for the geometries of interest at medium-to-high Reynolds numbers. The differences between the two models in terms of receiver outer surface temperature and pressure gradient were found to be negligible. Based on numerical stability and predictive accuracy, the k–ω turbulence model was selected. In particular, the Shear Stress Transport (SST) formulation was adopted due to its improved near-wall resolution and widespread validation for similar receiver configurations reported in the literature [90–95].

The SST model solves transport equations for the turbulent kinetic energy k and specific dissipation rate ω, given by

$$\frac{\partial(\rho k)}{\partial x_i} = \frac{\partial}{\partial x_j}\left(\Gamma_k \frac{\partial k}{\partial x_j}\right) + G_k - Y_k + G_b \tag{3.4}$$

$$\frac{\partial(\rho \omega)}{\partial x_i} = \frac{\partial}{\partial x_j}\left(\Gamma_\omega \frac{\partial \omega}{\partial x_j}\right) + G_\omega - Y_\omega + G_{\omega b} \tag{3.5}$$

The buoyancy-related production terms G_b and $G_{\omega b}$ are activated only when buoyancy forces are present (Chapter 6) and are disabled in Chapters 4 and 5.

Heat conduction in the solid receiver tube, glass envelope, and annular space (if only conduction is concerned, like in Chapters 4 and 5) is governed by the steady conduction equation

$$\frac{\partial}{\partial x_j}\left(\lambda\frac{\partial T}{\partial x_j}\right) = 0 \tag{3.6}$$

The annulus is treated differently depending on the study objectives. In Chapters 4 and 5, the annulus contains still air but is solved through an effective thermal conductivity. In Chapter 4, only a single value of effective thermal conductivity is considered at atmospheric pressure. In Chapter 5, the effective thermal conductivity is evaluated over a range from full vacuum to atmospheric pressure. Therefore, only conduction is considered in the model.The Navier–Stokes equations are therefore disabled, and only radiative heat exchange and conduction are solved. Chapter 5 additionally considers non-vacuum conditions using an effective thermal-conductivity model to represent free-molecular conduction at low pressures and combined conduction–convection behavior at higher pressures. In Chapter 6, two annulus atmospheres are modelled: (i) a vacuum state in which only the energy equation and radiative exchange are solved, and (ii) a hydrogen-filled annulus at 1 mbar, where laminar natural convection occurs. For the hydrogen case, the full laminar momentum and energy equations are solved, including buoyancy forces, and the continuum assumption is validated by a Knudsen number of the order of 10^{-3}.

Radiative heat transfer between the receiver tube and the glass envelope is included in all simulations through the Surface-to-Surface (S2S) radiation model [61, 83, 96], with temperature-dependent emissivity applied to the receiver's selective coating.

The numerical solution strategy is identical across all chapters: a coupled pressure–velocity algorithm is employed, second-order upwind discretisation is applied to all transport equations, and simulations are continued until all residuals fall below 10^{-6}. This modelling framework ensures consistency while allowing the physics specific to each chapter—fins, annulus pressure, hydrogen ingress, and full-length thermal development—to be represented accurately.

3.3.1 Boundary conditions

The boundary conditions used in this thesis follow a consistent structure across Chapters 4, 5, and 6, with modifications applied depending on whether a periodic domain (Chapter 4 and Chapter 5) or a full-length receiver (Chapter 6) is simulated. A schematic representation of the boundary conditions and the characteristics of the domains on a cross-section of the receiver can be seen in Figure 3.2, and the complete boundary-condition framework is defined as follows:

- Inlet and outlet of the HTF in the receiver
  - **Chapters 4 and 5:** Periodic boundary conditions are imposed for momentum, energy, and turbulence equations [97], representing a thermally fully developed flow within a short computational domain equal to one outer tube diameter. Chapter 4 uses mass flow rates in the range 0.4043–1.213 kg/s with a bulk temperature of 600 K, whereas Chapter 5 employs a mass flow rate of 1.75 kg/s and bulk temperatures of 500 K, 600 K, and 700 K.
  - **Chapter 6:** A physical inlet–outlet configuration is applied. Inlet conditions prescribe a constant mass flow rate ($\dot{m}$) and temperature (T_{in}), with mass flow rates of 3, 4, 5, and 6 kg/s and inlet temperatures ranging from 290 °C to 390 °C (in 20 °C increments). The outlet uses a pressure outlet boundary condition.
- Receiver tube walls
  - **Inner wall (all chapters):** Coupled thermal boundary condition with no-slip velocity and conjugate heat transfer between HTF and solid tube.
  - **Outer wall (all chapters):** Coupled thermal boundary condition. The non-uniform heat flux (LS-3 profile, see Figure 4.4(d) for a qualitative distribution) is applied via ANSYS Fluent's Thin-Wall model using a user-defined expression (UDE) [98]. The heat flux is expressed as the product of the direct normal irradiance

(DNI) and a function of the local concentration ratio (LCR) [33], as illustrated in Figure 4.4(c).

For Chapters 4 and 5, a single value of DNI $= 1000\ \mathrm{W/m^2}$ is used. In Chapter 6, two different irradiance levels are analysed, namely DNI $= 850\ \mathrm{W/m^2}$ and DNI $= 1000\ \mathrm{W/m^2}$, to investigate the impact of varying solar input on receiver thermal behaviour.

The LCR distribution was adopted from the optical simulation of the LS-3 collector performed by Wang *et al.* [33], who used a Monte Carlo Ray Tracing (MCRT) model validated for the DISS project. Their model accounted for mirror reflectance (≈ 0.94), glass transmittance (≈ 0.96), and receiver absorptance (≈ 0.96), reproducing the realistic non-uniform flux distribution along the receiver circumference. In this study, the normalized LCR profile from that work is directly imposed through the relation

$$q''(\alpha) = \mathrm{LCR}(\alpha) \times \mathrm{DNI} \tag{3.7}$$

which provides a physically consistent and computationally efficient representation of the LS-3 flux pattern.

The radiative exchange with the glass cover inner wall is accounted for using the Surface-to-Surface (S2S) radiation model [96, 99]. For Chapters 4 and 5, the emissivity of the receiver's outer wall, denoted by ε_r, is modeled as a temperature-dependent function of the outer surface temperature T_{ro} [100]:

$$\varepsilon_r = 0.05599 + 1.039 \times 10^{-4}\, T_{ro} + 2.249 \times 10^{-7}\, T_{ro}^{-2} \tag{3.8}$$

For Chapter 6, the outer surface of the receiver tube is coated with a material whose emissivity varies with temperature, as shown in Eq. 6.2.

- Annulus and solid Domain ends
  - Adiabatic walls (zero heat flux) at both ends of the annulus, receiver tube, and glass cover [15].
- Glass cover walls

- **Inner wall (all chapters):** Coupled thermal boundary condition between the solid glass and annulus. Radiative exchange with the receiver tube is included via S2S. The glass emissivity is taken as $\epsilon_g = 0.86$.
- **Outer wall (all chapters):** Mixed convection–radiation boundary condition. The emissivity of the glass cover, ϵ_g, is 0.86. The ambient temperature, T_{amb}, is 298 K (for Chapters 4 and 6) and 288 K, 298 K, and 308 K (for Chapter 5). The sky temperature, T_{sky}, is 8 K lower than the ambient temperature.

  In Chapters 4 and 5, only forced convection (the effect of wind) is considered, while in Chapter 6, both forced and natural convection (no wind) are considered.

  The following correlation is used for the natural convection (without wind) heat transfer coefficient h_w [101]

  $$h_w = \left(0.48\,\mathrm{Ra}_{D_{go}}^{0.25}\right)\frac{\lambda_a}{D_{go}} \tag{3.9}$$

  where λ_a is the air thermal conductivity at ambient temperature and $\mathrm{Ra}_{D_{go}}$ is the Rayleigh number for air based on the glass cover outer diameter and calculated as

  $$\mathrm{Ra}_{D_{go}} = g\beta_a \Delta T \frac{D_{go}^3 \rho^2 c_{p,a}}{\mu_a \lambda_a} \tag{3.10}$$

  where β_a is the thermal expansion coefficient, ΔT is the temperature difference between the ambient temperature T_{amb} and the glass cover temperature T_{go}, and ρ_a, $c_{p,a}$, μ_a are the air thermal properties at ambient temperature.

  Instead, the following correlation was used for the forced convection (with wind) heat transfer coefficient h_f [59]

  $$h_f = 4\,u_w^{0.58}\,D_{go}^{-0.42} \tag{3.11}$$

  where u_w is wind speed. For Chapter 4, u_w is 2.5 m/s; for Chapter 5, u_w is 2.5 and 4.5 m/s; and for Chapter 6, u_w is 5 and 10 m/s.

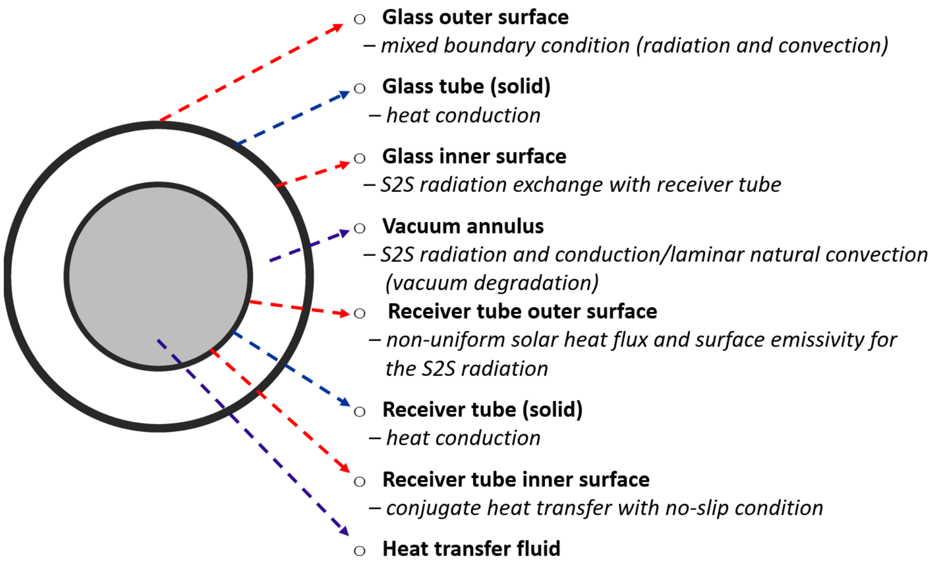

FIGURE 3.2: Schematic representation of the computational domains and applied boundary conditions for the receiver cross-section.

3.3.2 Processing of numerical data

In this thesis, the numerical data obtained from the CFD simulations are processed using a consistent set of definitions for all quantities of interest. The simulations provide the HTF bulk temperatures, receiver and glass wall temperatures, pressure drop or pressure gradient, and the total heat transfer rate. These results form the basis for evaluating flow characteristics, heat-transfer performance, and thermal losses.

As a common practice in literature [32, 54, 56], the Reynolds number is defined conventionally without considering the fins, if any, i.e. using the absorber inner diameter D_{ri},

$$\mathrm{Re} = \frac{4\,\dot{m}}{\pi\, D_{ri}\, \mu_f} \tag{3.12}$$

The Darcy friction factor is evaluated from the pressure loss,

$$f = \frac{(\Delta p/L)D_{ri}}{\rho u_{in}^2/2} \tag{3.13}$$

where L is the computational length, equal to one tube diameter in Chapters 4 and 5, and the full receiver length in Chapter 6.

The energy balance equation for the receiver can be written in terms of losses as

$$Q_{loss} = Q_{tot} - Q_u = Q_{rad} + Q_{cond} \tag{3.14}$$

where Q_{tot} is the total heat flux imposed on the outer surface of the receiver tube. The useful heat Q_u is the part of Q_{tot} that is transferred through the receiver and delivered to the heat transfer fluid (HTF). The remaining heat, defined as the total heat loss Q_{loss}, is therefore equal to the difference between the total heat flux and the useful heat transferred to the HTF. The heat losses consist of radiative losses Q_{rad} and conductive losses Q_{cond}.

The average inner convective heat transfer coefficient is calculated, in accordance with the prevailing approach proposed in the existing literature [55, 56, 59, 62, 86], as

$$h_i = \frac{Q_u}{A_{ri}\left(T_{ri} - T_b\right)} \tag{3.15}$$

where A_{ri} is the area of the inner actual surface of the receiver, T_b is the average fluid temperature within the computational domain computed as the mean of the inlet and outlet temperatures, and T_{ri} is the average temperature on the inner actual surface of the receiver. It should be noted that A_{ri} represents the actual inner surface area of the receiver, i.e., the contact area between the heat transfer fluid and the solid material of the receiver. This heat transfer area also includes any extended surfaces provided by internal fins, when present. Therefore, the definition accounts for fins in the sense that the total heat exchange area includes the additional extended surface. However, the fin efficiency, defined as the ratio between the heat flow transferred through the fin and the maximum heat flow that would be transferred by an isothermal fin at the same temperature as its base, is not included in the definition of h_i. The use of the classical fin efficiency concept is difficult to justify in this context, since the heat flux is not uniform. As a result, the temperature at the base of the fins varies significantly depending on their circumferential position. For this reason, the effect of thermal conduction within the fins, i.e., their efficiency, is incorporated into the overall heat transfer coefficient defined below.

In real applications, the main focus is on the overall performance of the receiver. Since thermal losses, which reduce the useful heat load Q_u, depend on the outer temperature of the receiver T_{ro}, a novel approach is proposed in this work by defining the average heat transfer coefficient h_o referred to the outer surface of the receiver tube

$$h_o = \frac{Q_u}{A_{ro}\left(T_{ro} - T_b\right)} \tag{3.16}$$

where A_{ro} is the outer surface area, and T_{ro} is the average temperature on the outer surface of the receiver. It must be pointed out that h_o should be regarded as an equivalent convection coefficient since it also includes the effects of the solid wall and, if any, the fins on the overall thermal resistance. From a theoretical perspective, this approach is similar to the one used to define the overall heat transfer coefficient in heat exchangers [102].

Accordingly, the inner Nusselt number Nu_i is defined as

$$\mathrm{Nu}_i = \frac{h_i D_{ri}}{\lambda_f} \tag{3.17}$$

while the overall Nusselt number Nu_o is defined as

$$\mathrm{Nu}_o = \frac{h_o D_{ro}}{\lambda_f} \tag{3.18}$$

where, λ_f is the thermal conductivity of the fluid.

Different solutions can be compared using a performance evaluation criterion PEC for equal pumping power [103], calculated with both inner and overall Nusselt numbers

$$PEC_i = \frac{\left(\mathrm{Nu}_i/\mathrm{Nu}_{i,0}\right)}{\left(f/f_0\right)^{1/3}} \tag{3.19}$$

$$PEC_o = \frac{\left(\mathrm{Nu}_o/\mathrm{Nu}_{o,0}\right)}{\left(f/f_0\right)^{1/3}} \tag{3.20}$$

where $\mathrm{Nu}_{i,0}$ and $\mathrm{Nu}_{o,0}$ represent the inner and overall Nusselt number of smooth tubes, while f and f_0 represent the friction factors for the finned tubes and smooth tubes, respectively.

As will be shown later in Chapter 4, the proposed h_o, Nu_o and PEC_o are found to be a more appropriate basis for performance evaluation due to the non-uniform temperature distribution on the receiver circumference.

Finally, another key parameter is the maximum circumferential temperature difference at the absorber outer wall, ΔT_{max}, which is calculated as follows

$$\Delta T_{max} = T_{ro,max} - T_{ro,min} \tag{3.21}$$

where $T_{\mathrm{ro,\,max}}$ and $T_{\mathrm{ro,\,min}}$ are the maximum and minimum outer wall temperatures, respectively.

This unified post–processing framework ensures that the numerical results from both the periodic finned-receiver study (Chapter 4) and the full-length receiver analysis (Chapter 6) are interpreted consistently while preserving the distinctions required by their differing physical objectives.

Chapter 4

Thermal Performance of Longitudinally Finned Receivers

In this chapter, longitudinal fins were examined as a simple and cost-effective method for augmenting heat transfer within the receiver tube of the PTC system. However, due to the inherently non-uniform heat flux distribution along the receiver circumference, the positioning of these fins significantly influences thermal performance, but this aspect has not been thoroughly explored in the literature. This chapter systematically investigates the effects of the location, as well as height and number of fins, and clarifies the distinct roles of fins positioned on the different halves of the receiver tube. Furthermore, a novel performance evaluation metric was proposed, offering a more representative basis for comparison than the conventional approach commonly adopted in the literature.

More specifically, computational fluid dynamics simulations are employed to assess the thermal performance of receivers equipped with rectangular-profile fins across a range of Reynolds numbers from $20,000$ to $60,000$. The numerical model was validated against experimental data from the literature. Results from configurations with 2, 4, 6, and 8 fins reveal that optimal thermal management was achieved by placing shorter fins in regions of higher heat flux and longer fins in areas of lower heat flux. The most effective configuration yields a 45.6% enhancement in the overall Nusselt number and an 18.0% reduction in heat losses compared to a smooth receiver. These findings offer valuable insights for the design of more efficient parabolic trough receivers, contributing to improved thermal performance and reduced risk of tube deformation and failure in linear collectors.

4.1 System description

Figure 4.1 presents a cross-sectional schematic of a parabolic trough solar collector (PTC), which comprises a parabolic reflective surface and an absorber tube positioned along its focal line. To enhance heat transfer to the heat transfer fluid (HTF) and improve the system's reliability, longitudinal fins are incorporated into the receiver tube. In this chapter, a numerical investigation is conducted on the receiver tube configuration of the well-established Luz System Three (LS-3) PTC system [104, 105]. As illustrated in Fig. 4.2(a), the receiver tube has an inner diameter D_{ri} of 66 mm and an outer diameter D_{ro} of 70 mm. The surrounding glass envelope features an inner diameter D_{gi} of 109 mm and an outer diameter D_{go} of 115 mm.

The non-uniform distribution of heat flux across the PTR induces a circumferential temperature gradient. Specifically, the lower half of the receiver is subjected to concentrated solar radiation reflected by the parabolic

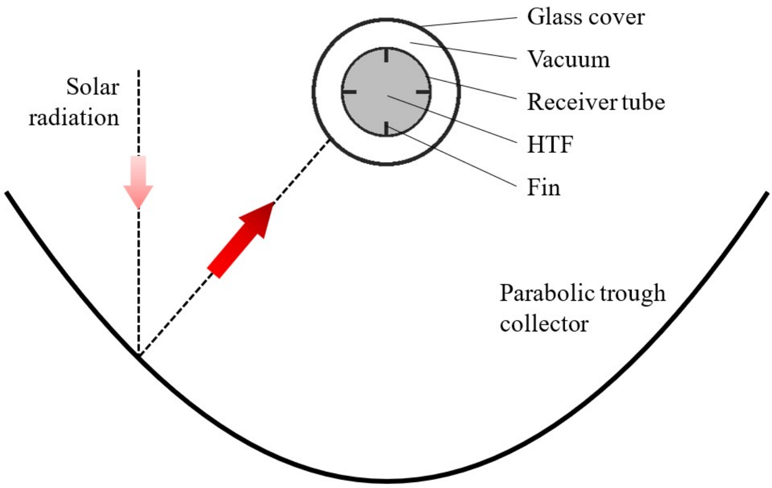

FIGURE 4.1: Cross-section of a parabolic trough collector with inner fins.

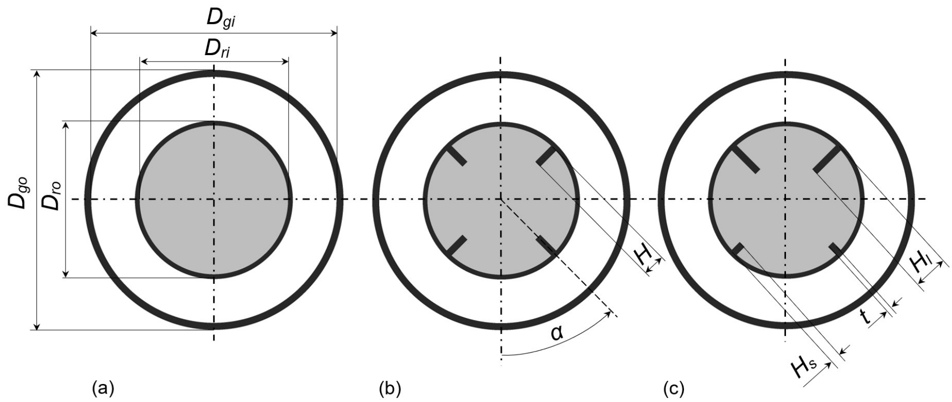

FIGURE 4.2: Parabolic Trough Receiver geometry: (a) smooth tube, (b) tube with equal length fins, and (c) tube with fins of different heights in the upper and lower half.

mirror, resulting in significantly higher heat flux, whereas the upper half is exposed only to direct solar radiation. The primary objective of this chapter is to numerically assess the influence of internal longitudinal fins within the PTR tube on mitigating thermal gradients and enhancing overall thermal performance. As the fins may be unevenly distributed around the circumference of the tube, the exact position of each fin can be identified by the fin angle α, defined as in Fig. 4.2(b). Three different fin heights will be investigated and will be referred to as medium (H), shorter (H_s) and longer (H_l), as shown in Fig. 4.2(b) and (c). Only fins of identical thickness $t = 3$ mm are subjected to analysis, as the fin height plays a more significant role than its thickness [62].

Table 4.1 provides a comprehensive overview of the geometrical parameters (number of fins N, fin heights H, H_s and H_l, and the list of fin angles α) for all the fifteen configurations analyzed. The corresponding cross-sections are illustrated in Fig. 4.3.

The rationale for selecting the investigated configurations is discussed in detail later in the chapter. As illustrated, five primary receiver configurations were numerically analyzed: a smooth tube (used as the reference case), and tubes equipped with two, four, six, and eight internal longitudinal fins. To gain deeper insight into the thermal behavior of the fins located in the upper (cooler) and lower (hotter) regions of the receiver, and to mitigate the

TABLE 4.1: Geometrical parameters of all configurations analyzed. The fin thickness t is always equal to 3 mm.

Case	N	H (mm)	H_s (mm)	H_l (mm)	α (°)
Smooth	–	–	–	–	–
2FCase1	2	10	–	–	$-45, 45$
2FCase2	2	10	–	–	$-135, 135$
4FCase1	4	10	–	–	$-90, 0, 90, 180$
4FCase2	4	10	–	–	$-135, -45, 45, 135$
4FCase3	4	–	5	15	$-135, -45, 45, 135$
4FCase4	4	–	5	15	$-135, -45, 45, 135$
6FCase1	6	10	–	–	$-120, -60, 0, 60, 120, 180$
6FCase2	6	10	–	–	$-150, -90, -30, 30, 90, 150$
6FCase3	6	10	–	–	$-150, -90, -45, 45, 90, 150$
6FCase4	6	–	5	15	$-150, -90, -45, 45, 90, 150$
8FCase1	8	10	–	–	$-157.5, -112.5, -67.5, -22.5,$ $22.5, 67.5, 112.5, 157.5$
8FCase2	8	10	–	–	$-135, -90, -45, 0, 45, 90, 135, 180$
8FCase3	8	–	5	15	$-135, -90, -45, 0, 45, 90, 135, 180$
8FCase4	8	–	5	15	$-135, -90, -45, 0, 45, 90, 135, 180$

formation of thermal hot spots, several sub-configurations were defined for each fin count. Each configuration, except the smooth tube, is designated using the nomenclature 'N FCase n', where N represents the number of fins and n is the number of sub-cases that differ in fin position and height. In the case of the two-fin configuration, 2FCase1 and 2FCase2 feature fins of the same height H but on the lower or upper half of the tube, respectively. For the four-fin configuration, 4FCase1 and 4FCase2 have a uniform distribution of fins around the circumference of the tube, yet with a different alignment with respect to the vertical direction. 4FCase3 and 4FCase4 feature fins of different heights on the lower and upper halves of the tube. For 4FCase3 the fins are longer (height H_l) on the bottom and shorter (height H_s) on the top, and vice versa for 4FCase4. The fin distributions in cases 6FCase2 and 8FCase2 are obtained by rotating those of cases 6FCase1 and 8FCase1, respectively. In case 6FCase3, the fins on the bottom side have a slightly different angle than in case 6FCase2. Cases 6FCase4, 8FCase3, and 8FCase4

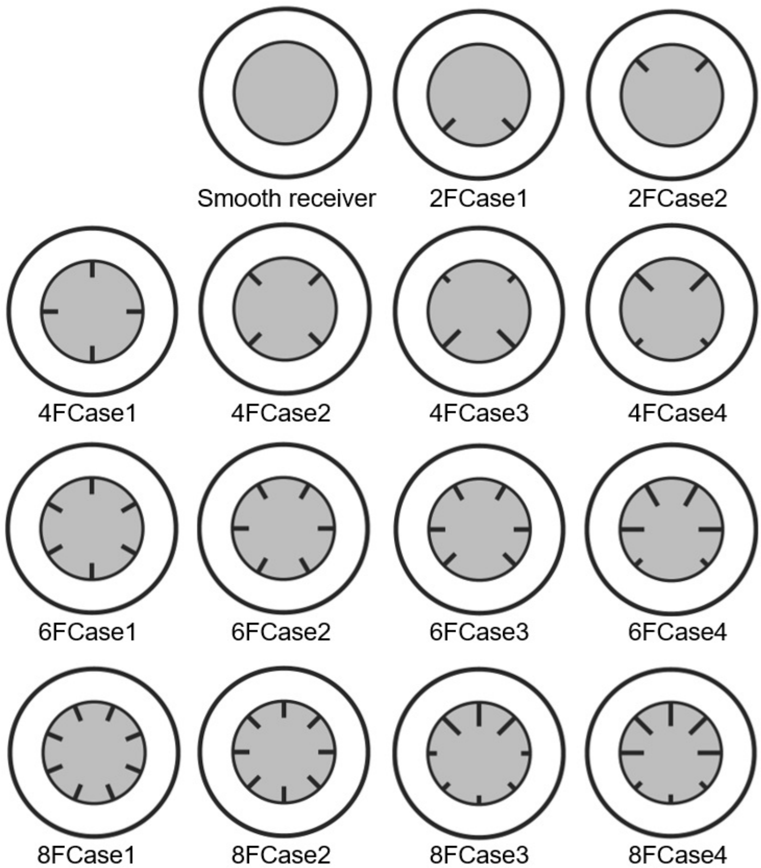

FIGURE 4.3: Cross-sectional geometries of all analyzed receiver configurations.

all feature longer fins on the top and shorter ones on the bottom. 8FCase3 and 8FCase4 only differ in the number of long and short fins: five short and three long for 8FCase3 and three short and five long for 8FCase4.

Sytherm 800 oil, stainless steel, air, and Pyrex are the HTF, receiver tube, annular space, and glass cover material, respectively. The thermophysical properties of these materials are listed in Table 4.2, where density ρ, specific heat c_p, thermal conductivity λ, and viscosity μ are provided. In this chapter, the temperature dependence of the HTF properties is not taken into account to focus the analysis on the effect of fin position and size without the influence of other parameters. The thermophysical properties of Syltherm 800 oil are estimated at a temperature of 600 K, based on available literature data [56]. Only conduction in the annular space is considered, using the thermal conductivity of air at an atmospheric condition [80].

TABLE 4.2: Thermophysical properties of HTF, receiver tube, annular space, and glass cover materials.

Material	ρ (kg/m^3)	c_p (J/kg K)	λ (W/m K)	μ_f (Pa s)
Syltherm oil	640	2133	0.0773	0.00039
Stainless steel	8030	502.48	24.92	
Air			0.02551	
Pyrex	2230	900	1.2	

In practical applications, PTR tubes are typically of considerable length. After a short distance from the entrance, the flow reaches a fully developed state, wherein the velocity and dimensionless temperature fields no longer change. Therefore, to limit the numerical effort, the computational domain can be limited to a very small portion of the tube, as shown in Fig. 4.4(a), with length L provided that periodic inlet-outlet boundary conditions [32, 61] are applied at the ends of the fluid. In this chapter, L is assumed to be equal to the outer diameter of the receiver tube D_{ro}, as depicted in Fig. 4.4(a) where only the solid domains, i.e., receiver tube and glass cover, are shown. The periodic boundary conditions are shown in Fig. 4.4(b).

It is important to acknowledge that, under real operating conditions, parameters such as direct normal irradiance (DNI), wind speed, and ambient temperature exhibit significant diurnal and seasonal variability, which can influence both thermal performance and heat losses. In this chapter, however, a steady-state approach is adopted, with constant values for these parameters selected based on previous analyses [54–56, 106]. This assumption allows for the isolation of the effects of fin geometry and positioning on the thermal behavior of the receiver. Despite this simplification, the findings retain general applicability: configurations that demonstrate superior performance under the assumed conditions are expected to maintain their relative advantage across a range of environmental scenarios.

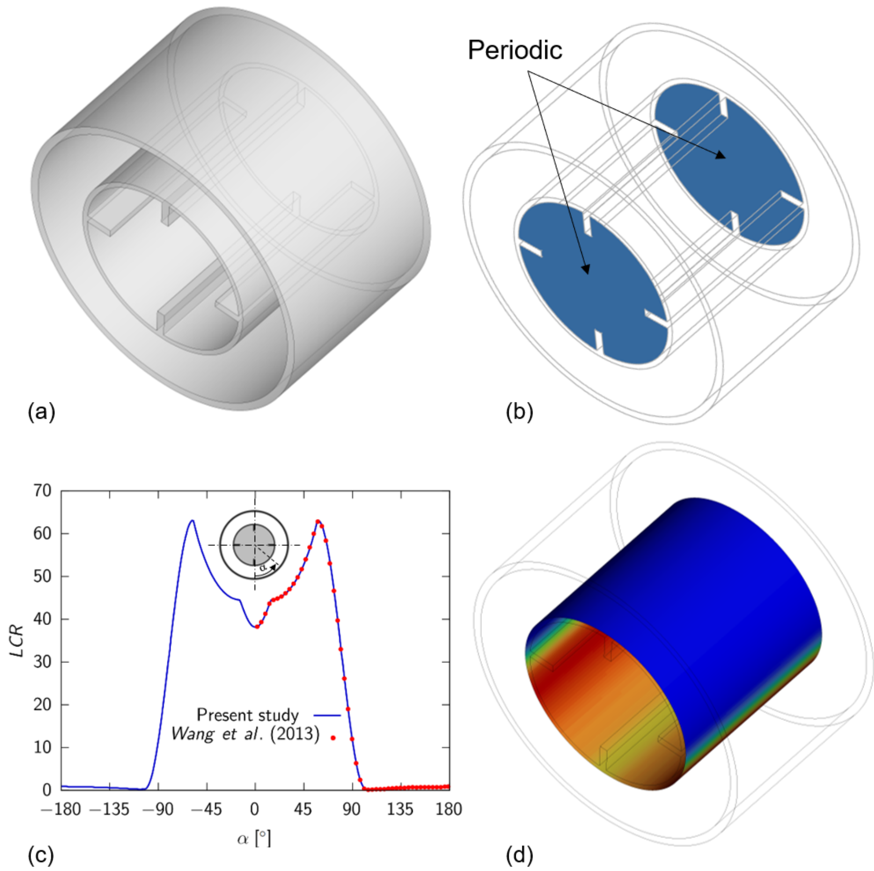

FIGURE 4.4: (a) Solid parts of the computational domain, (b) periodic inlet-outlet, (c) local concentration ratio, and (d) qualitative distribution of the heat flux imposed on the outer wall of the receiver (red: maximum heat flux; blue: minimum heat flux).

4.2 Numerical approach

A detailed description of the governing equations, turbulence modelling, numerical schemes, and radiation treatment adopted in this work is provided in Chapter 3. The present section therefore summarizes and focuses on the specific modelling choices relevant to the analyses presented in this chapter.

The numerical investigation is carried out using the commercial CFD software ANSYS Fluent 2025R1 [107]. The analysis involves the solution of a coupled conjugate heat-transfer problem, including forced convection in the heat transfer fluid, heat conduction within the solid subdomains (namely the steel receiver tube and the glass cover), and combined conduction and radiation heat transfer between the facing surfaces in the annular space. The thermophysical properties are assigned according to the specific subdomain in which the governing transport equations are solved.

The flow of the heat transfer fluid is assumed to be steady-state, fully developed, and fully turbulent. Syltherm 800 is modelled as an incompressible and Newtonian fluid with constant thermophysical properties evaluated at the representative operating temperature. Turbulence effects are accounted for using a Reynolds-averaged formulation of the governing equations.

All simulations are performed under fully turbulent flow conditions, and the k–ω turbulence model in its Stress Transport (SST) formulation was selected.

Although the annular space between the receiver tube and the glass cover is treated as a fluid region, it is assumed to contain still air but solved through effective thermal conductivity. Consequently, fluid motion in this region is neglected, and a zero-velocity field is imposed. Heat transfer within the annulus and within the solid subdomains is therefore governed by heat conduction, while radiative heat exchange between the receiver outer surface and the inner surface of the glass cover is modelled using the Surface-to-Surface (S2S) radiation approach.

Pressure–velocity coupling is handled using the coupled solution scheme, and second-order upwind discretization is employed for all transport equations. The numerical simulations are considered converged when the residuals of all solved equations are reduced below 10^{-6}.

4.2.1 Grid independence and model validation

To ensure the reliability of the results, a mesh independence test has been first carried out to select the appropriate grid structure and size. Then, to prove the reliability of the CFD model, the numerical results have been compared with literature data.

Grid independence test

Five hexahedral conformal meshes have been created for the case with eight identical fins (8FCase2) using the Ansys meshing tool. The number of elements in each mesh has been progressively increased and is equal, from the coarsest to the finest mesh, to 29,330, 55,644, 119,616, 245,950, and 544,284, respectively. The receiver outer wall average temperature T_{ro} and the pressure gradient $\Delta p/L$ are then computed for each mesh at the highest Reynolds number as shown in Fig. 4.5(a). The solution is deemed to be mesh-independent when the maximum variation in the aforementioned parameters is less than 0.1%. For this reason, the final mesh used for the simulations is the one with 245,950 elements.

The quality of the mesh was assessed using standard metrics. With an average cell skewness of 0.26 and an average orthogonality quality of 0.87, the mesh meets the requirements for accurate CFD simulations. For the largest values of the Reynolds number $\mathrm{Re} = 60,000$ investigated, the maximum value of the dimensionless distance from the wall y^+ was 1.39, while the average value was 1.01, which is consistent with the adopted turbulence model.

The 2D mesh on a generic cross-section of the computational domain being used to generate the 3D mesh by axial sweep is shown in Fig. 4.5(b).

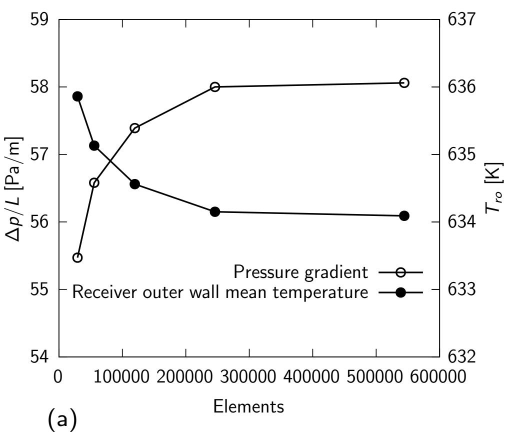

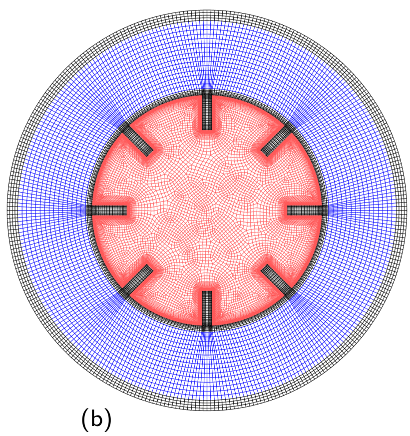

FIGURE 4.5: (a) Grid independence test results for $\mathrm{Re} = 60,000$ and (b) detail of the final mesh on a generic cross-section of the computational domain.

The mesh for the HTF subdomain is colored red, while that for the annular space is colored blue. The meshes for the solid regions, i.e., the receiver tube and the glass cover, are colored black. Similar grid resolutions have been used for the cases where the fin number is different.

The simulations were performed in parallel mode using 8 CPU cores (12th Gen Intel® Core™ i7-12700, 2.10 GHz). A representative steady-state case required 629 s (≈ 0.175 h) of wall-clock time, corresponding to approximately 1.4 core-hours. These results indicate that the proposed approach is computationally efficient and suitable for parametric studies.

Numerical model validation

The numerical model has been validated with respect to both smooth and finned receivers. First, the following correlations are used to validate the friction factor and the Nusselt number for a smooth tube

- Blasius correlation [108]

$$f = 0.3164\mathrm{Re}^{-0.25} \tag{4.1}$$

- Gnielinski correlation [109]

$$\mathrm{Nu} = \frac{\left(\frac{f}{8}\right)(\mathrm{Re} - 1000)\,\mathrm{Pr}}{1 + 12.7\left(\frac{f}{8}\right)^{0.5}\left(\mathrm{Pr}^{\frac{2}{3}} - 1\right)} \tag{4.2}$$

The comparison between the numerical results and the correlation data is shown in Fig. 4.6(a) for the friction factor f_0 and in Fig. 4.6(b) for the Nusselt number $\mathrm{Nu}_{i,0}$. The agreement is very good and the mean deviation for the friction factor and Nusselt number is equal to 0.1% and 1.6%, respectively.

Subsequently, the numerical results obtained for the longitudinally finned receiver configurations were validated through comparison with the experimental data reported by Jensen and Vlakancic [52]. Their model, primarily focused on small and thin fins with equal height, provides a well-validated basis for evaluating pressure drop and heat transfer in tubes with internal fins in the case of uniform heat flux. The comparison of the friction factor f and Nusselt number Nu_i for the eight equal fin height receiver

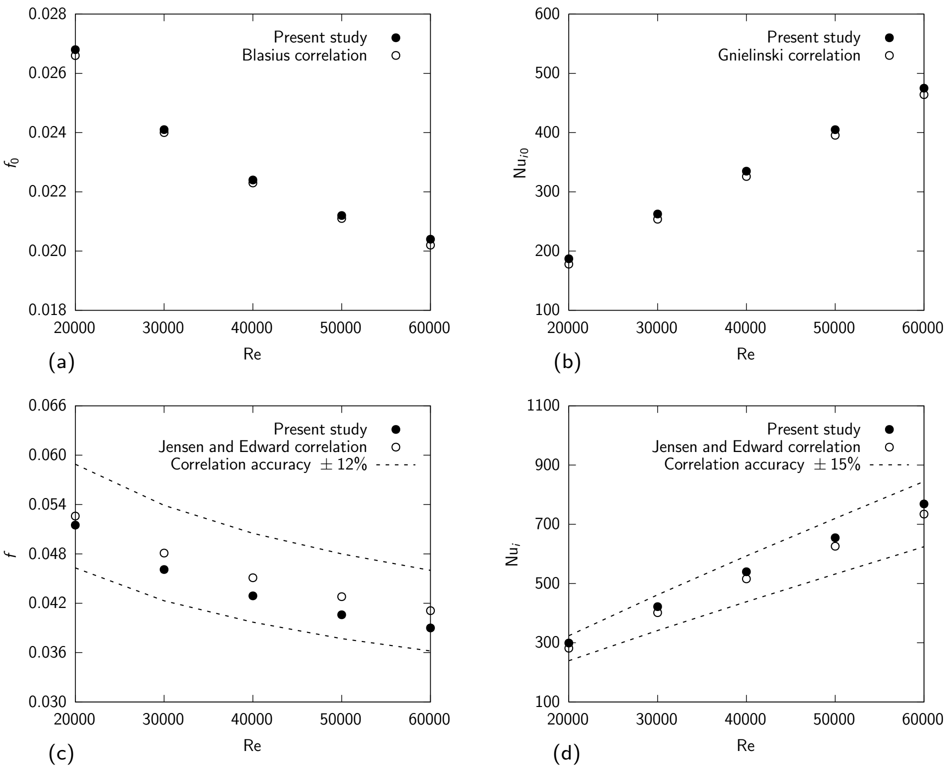

FIGURE 4.6: Validation of numerical results: (a) friction factor for the smooth receiver, (b) Nusselt number for the smooth receiver, (c) friction factor for the finned receiver 8FCase2, and (d) Nusselt number for the finned receiver 8FCase2.

geometry corresponding to that of case 8FCase2 is shown in Fig. 4.6(c) and (d), respectively. The numerical results concerning the solar parabolic receiver with internal fins align closely with those predicted by the theoretical framework of [52], with an average deviations of 4.3% for the friction factor and 5.0% for the Nusselt number, well within the correlation accuracy, thus proving the reliability of the adopted physical and numerical models.

Finally, the full numerical model including the effect of the glass cover, has been validated with the experimental data from Burkholder and Kutscher

[69] for a smooth 2008 PTR70 parabolic trough receiver. The numerical results in terms of heat loss per unit length of the receiver agree well with the experimental ones, with an average deviation of 6.2%, as shown in Fig. 4.7. This comparison provides additional confidence in the real-world applicability of the model.

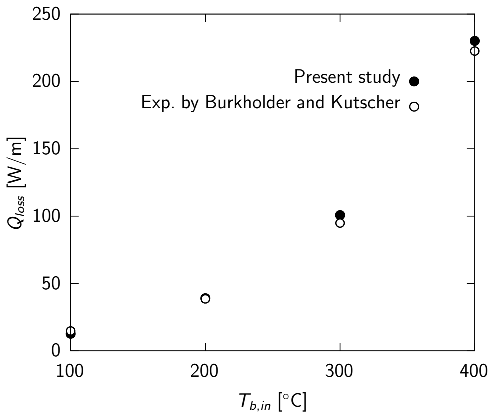

FIGURE 4.7: Validation of numerical results: heat loss per unit length of the receiver Q_{loss} for different HTF inlet temperatures $T_{b,in}$.

4.3 Results and discussion

The fifteen receiver geometries illustrated in Fig. 4.3 are subjected to numerical analysis over a range of Reynolds numbers from $20,000$ to $60,000$. The results are presented in the following subsections and are categorized into qualitative and quantitative analyses. The qualitative analysis includes velocity and temperature contour plots, as well as temperature distributions on the external surfaces of both the receiver and the glass envelope. The quantitative analysis encompasses key performance indicators such as maximum surface temperatures, friction factor, Nusselt number, performance evaluation criteria, and heat losses.

4.3.1 Velocity and temperature contours

The heat transfer performance depends on both the velocity and temperature fields in the receiver. Figure 4.8 displays a three-dimensional visualization of the HTF axial velocity field at the middle section of the computational domain for all geometries, evaluated at the intermediate mass flow rate $\dot{m} = 0.8086$ kg/s corresponding to Re $= 40,000$. The axis of the tube is shown in black with a dash-dotted line. As can be seen, the axial velocity distribution for the smooth receiver is axisymmetric, and the velocity goes from zero at the wall to the maximum values at the center of the cross-section. For all other geometries, the velocity profile exhibits indentations corresponding to the fins and, since the cross-section decreases as the number of fins increases, the maximum velocity at the center of the tube increases. For a symmetrical distribution of fins of equal length (cases 4FCase1, 4FCase2, 6FCase1, 6FCase2, 6FCase3, 8FCase1, and 8FCase2), the point of maximum velocity is always located at the center of the cross-section. If the fins are placed (case 2FCase1) or are longer (case 4FCase3) on the lower half of the tube, the point of maximum velocity moves away from the axis in the upward direction, while if the fins are placed (case 2FCase2) or are longer (cases 4FCase4, 6FCase4, 8FCase3, and 8FCase4) on the upper half of the tube, the point of maximum velocity moves away from the axis in the downwards direction. As shown in Fig. 4.8, the configuration 8FCase4 exhibits both the highest axial velocity magnitude among all cross-sections and the most pronounced downward displacement of the velocity peak, indicating a significant influence of fin geometry and placement on flow distribution. The temperature contours and some axial velocity iso-profiles at the middle section of the computational domain are presented in Fig. 4.9 for all cases and Re $= 40,000$. The annular zone and the glass cover are not shown in the figure to improve clarity. As can be observed, the number and location of fins have a significant impact on the flow field, which in turn affects the temperatures within the HTF and receiver tube. The highest temperature values are observed in the lower half of the receiver, which is subjected to the most intense heat flux, as shown in Fig. 4.4(d). To gain a deeper understanding of the distinct heat transfer mechanisms associated with the fins located on the upper and lower halves of the receiver tube, it is instructive to examine the simplified case involving two fins. Although this configuration holds limited practical relevance, it provides valuable physical insight into the underlying thermal behavior of the system. The

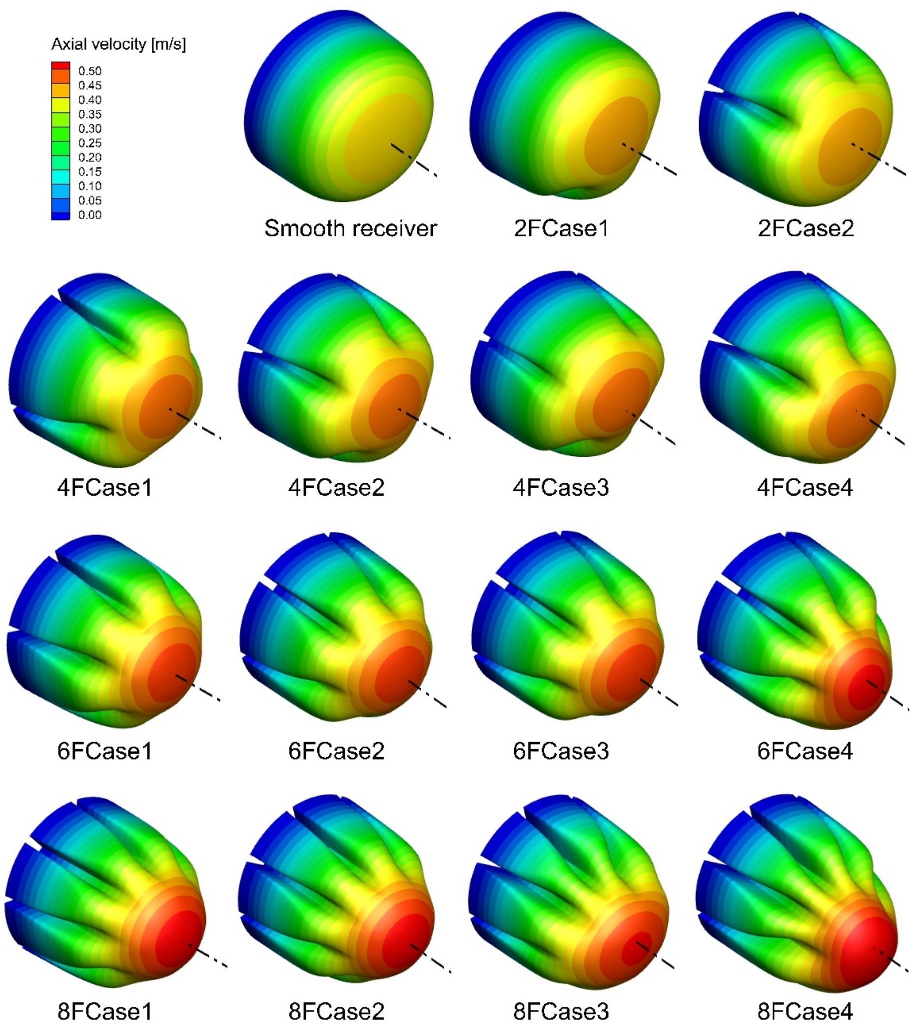

FIGURE 4.8: Axial velocity contours on the middle section of the computational domain for all receiver geometries and $\mathrm{Re} = 40,000$.

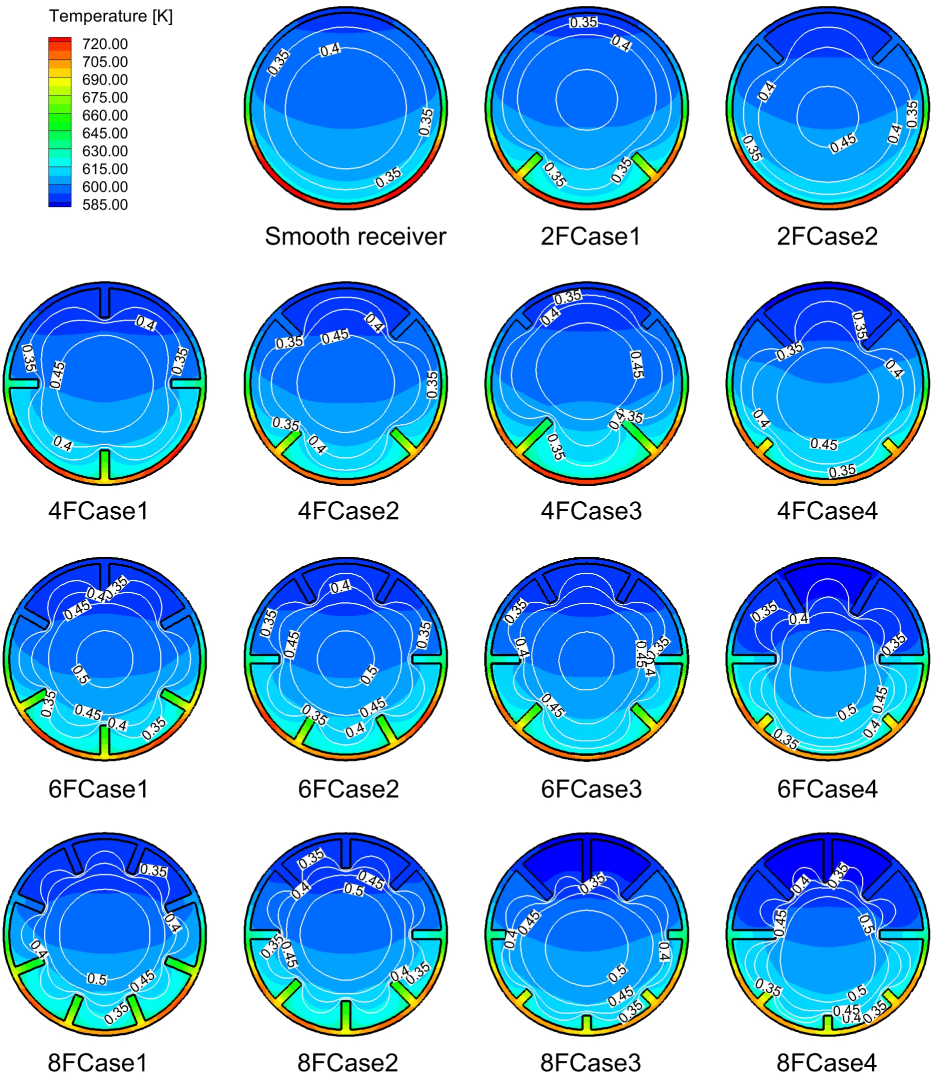

FIGURE 4.9: Temperature contours and velocity iso-lines on the middle section of the computational domain for all receiver geometries and Re $= 40,000$.

fins on the lower half (see case 2FCase1) exhibit large temperature gradients, suggesting a high conductive heat transfer, which helps reduce local hot spots in the receiver. On the contrary, the fins on the upper half (see case 2FCase2) have temperatures that are very close to that of the surrounding fluid, implying a very low heat flux and, therefore, a negligible local thermal effect. As previously observed in Fig. 4.8, the presence of longer fins on the upper half of the receiver tube redirects the high-velocity region of the heat transfer fluid flow toward the lower half. This redistribution enhances local convective heat transfer on the lower side, which is subjected to a higher heat flux. In essence, while the fins on the upper half of the receiver have minimal thermal impact, they play a crucial role in promoting convective transport by steering the bulk fluid toward the thermally stressed region, as illustrated by the axial velocity contours in Fig. 4.9. By strategically combining and balancing these effects, overall heat transfer performance can be significantly improved. This is demonstrated in configurations featuring more than two fins, specifically, cases 4FCase4, 6FCase4, 8FCase3, and 8FCase4, where the use of longer fins on the upper half and shorter fins on the lower half not only mitigates local hot spots but also reduces circumferential temperature non-uniformity along the receiver wall. Finally, for a symmetrical distribution of equal length fins (cases 4FCase1, 4FCase2, 6FCase1, 6FCase2, 6FCase3, 8FCase1, and 8FCase2), it can be seen that placing the fins at $\alpha = \pm 45^\circ$ (cases 4FCase2, 6FCase3, and 8FCase2), i.e., close to the angular position of the maximum heat flux values, reduces maximum temperatures.

4.3.2 Comparisons between the smooth receiver and cases 2FCase2 and 4FCase2

The following subsection provides a quantitative analysis to support the qualitative observations discussed previously. Table 4.3 reports the average temperatures of the finned inner surface T_{ri} and of the outer surface T_{ro} of the receiver for three Reynolds numbers and three receiver configurations: the smooth tube (reference), 2FCase2 (two fins on the upper half), and 4FCase2 (i.e., 2FCase2 with two additional symmetric fins on the lower half). The left portion of the table presents temperatures calculated over the lower half of the receiver, where approximately 92% of the total heat load is concentrated due to the imposed non-uniform heat flux distribution shown in Fig. 4.4(c), while the right portion shows values averaged over the entire receiver surface.

TABLE 4.3: Average temperatures on the finned inner surface T_{ri} and outer surface T_{ro} of the receiver for configurations Smooth, 2FCase2 and 4FCase2, three different Reynolds numbers and for the lower half (left side) or the entire (right side) receiver.

		lower half		entire receiver	
		T_{ri} (K)]	T_{ro} (K)	T_{ri} (K)	T_{ro} (K)
$\mathrm{Re} = 20,000$	Smooth	778.03	780.47	694.77	696.07
	2FCase2	771.32	773.97	674.07	690.98
	4FCase2	747.43	760.10	674.64	682.91
$\mathrm{Re} = 40,000$	Smooth	707.72	710.33	654.97	656.33
	2FCase2	703.72	706.50	642.73	653.67
	4FCase2	687.74	699.92	642.90	650.00
$\mathrm{Re} = 60,000$	Smooth	677.95	680.63	638.99	640.37
	2FCase2	675.26	678.10	630.33	638.67
	4FCase2	663.39	674.67	630.49	636.77

Since the heat flux imposed on the outer surface of the receiver has the same non-uniform distribution across all cases, a lower surface temperature (either inner or outer) indicates a higher local heat transfer coefficient, as defined by equations (3.15) and (3.16). As shown in the left portion of Table 4.3, 2FCase2 exhibits lower surface temperatures on the lower half compared to the smooth tube, implying enhanced local convective heat transfer. This supports the earlier qualitative conclusion that, although fins on the upper half have limited direct thermal impact, they effectively redirect the high-velocity HTF region toward the lower half, thereby improving heat transfer where it is most needed. A comparison between 2FCase2 and 4FCase2 further highlights the benefit of adding fins to the lower half. The additional fins in 4FCase2, positioned in the region of highest heat flux, exhibit large temperature gradients and lead to higher local heat transfer coefficients, as evidenced in Table 4.3 by the further reduction in both T_{ri} and T_{ro} on the lower half.

The right-hand side of Table 4.3 provides insight into why the average outer surface heat transfer coefficient, h_o, introduced in Subsection **??**, is a more appropriate metric for evaluating overall receiver performance. While the average inner surface temperature T_{ri} is nearly identical for 2FCase2 and 4FCase2, suggesting similar internal convective performance, this can be misleading. The true indicator of thermal efficiency is the outer surface temperature, which governs thermal losses. As will be further demonstrated in Subsection 6.3.4, 4FCase2 consistently exhibits lower T_{ro} values across all Reynolds numbers, confirming reduced thermal losses. This underscores the importance of using the overall heat transfer coefficient h_o and the corresponding Nusselt number Nu_o as the primary performance indicators.

4.3.3 Temperature profiles and maximum temperatures

As previously discussed, the non-uniform heat flux distribution induces circumferential temperature gradients in both the receiver tube and the surrounding glass envelope. These gradients can lead to increased thermal losses, structural deformation of the receiver, potential damage to the glass cover, and a reduction in its operational lifespan. Figure 4.10 illustrates the temperature profiles at the outer surface of the receiver and the glass cover, evaluated at the mid-plane of the computational domain for a Reynolds number of $40,000$. The smooth tube configuration, included as a reference in all plots (black curve), consistently exhibits higher surface temperatures compared to finned configurations. In Figures Fig. 4.10(a) and Fig. 4.10(b), distinct valleys in the temperature profiles correspond to the locations of the fins, indicating enhanced local heat transfer. This feature is not observed on the outer surface of the glass cover, as shown in Fig. 4.10(c) and Fig. 4.10(d). As the number of fins increases, the circumferential temperature variation decreases significantly for both the receiver and the glass envelope. Notably, Figures 4.10(a) and 4.10(b) demonstrate that 2FCase1, with fins positioned on the lower (high-flux) half of the receiver, outperforms 2FCase2, where fins are placed on the upper (cooler) half. Nevertheless, 2FCase2 still achieves lower surface temperatures than the smooth tube, confirming the beneficial effect of fins even when placed on the cold side. Configurations featuring asymmetric fin heights, such as 4FCase4, 6FCase4, 8FCase3, and 8FCase4, not only reduce peak temperatures but also improve circumferential temperature uniformity. These findings are consistent with the observations presented in Subsection 6.3.1, reinforcing the importance of strategic fin placement.

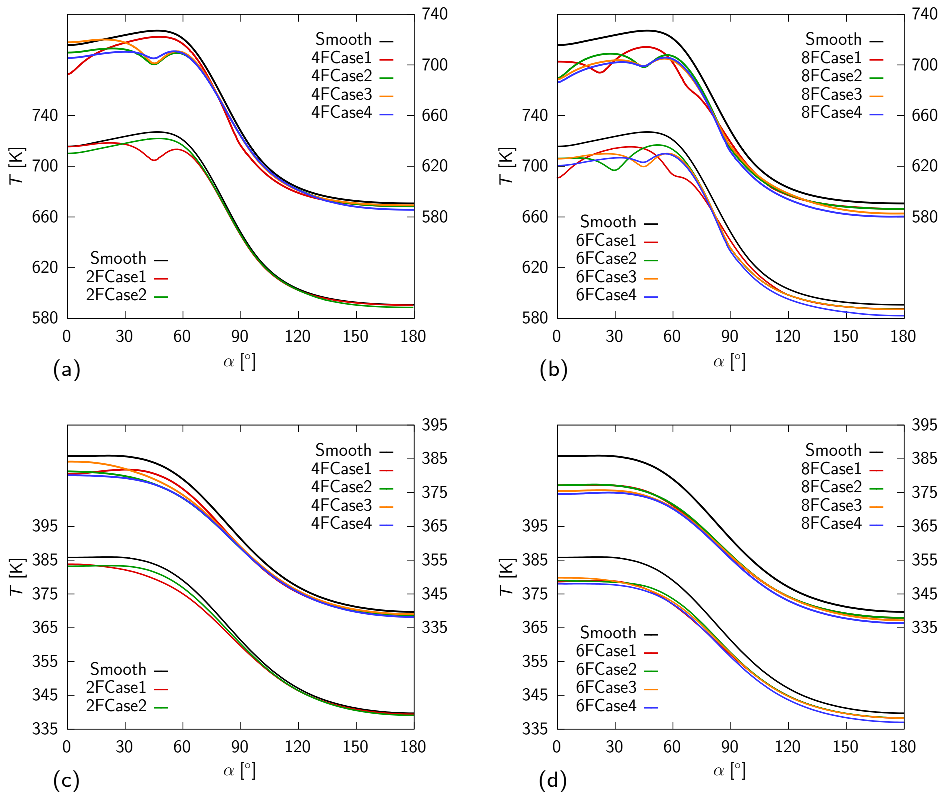

FIGURE 4.10: Circumferential temperature distributions for all receiver geometries and Re = 40,000: (a), (b) receiver outer wall; (c), (d) glass-cover outer wall.

The maximum temperature T_{max} on the outer wall of the receiver is reported in Fig. 4.11 as a function of the Reynolds number. As illustrated in the results, the maximum temperature within the receiver decreases with increasing Reynolds number and with the addition of internal fins. Across all configurations and Reynolds numbers analyzed, finned receivers exhibit a reduction in maximum temperature ranging from 5.6 K to 36.2 K compared to the smooth tube case. This substantial decrease is particularly promising, as it contributes to mitigating the risk of thermal deformation in the receiver tube, thereby enhancing structural integrity and operational reliability in practical applications.

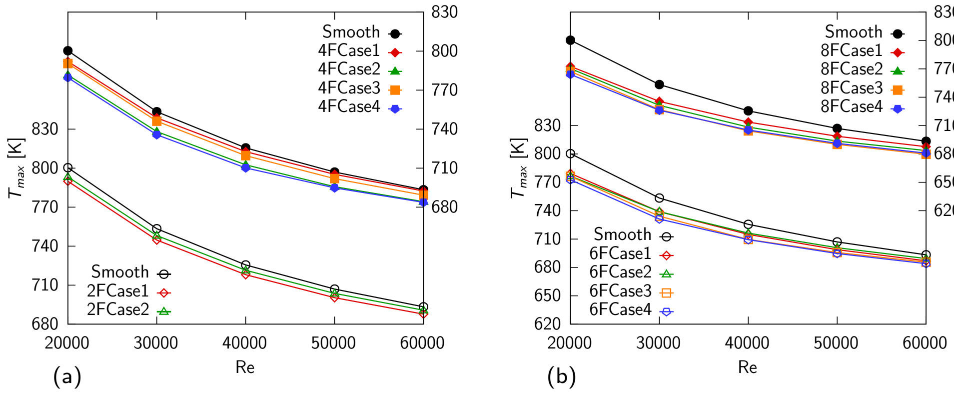

FIGURE 4.11: Maximum temperature T_{max} on the outer wall of the receiver versus Reynolds number.

4.3.4 Performance parameters

The effect of inner longitudinal fins in PTR tubes on pressure drop and heat transfer is illustrated in Fig. 4.12, where the friction factor f and the Nusselt number Nu are reported as a function of the Reynolds number.
The addition of fins always leads to an increase in the friction factor, as can be seen in Fig. 4.12(a) and (b). The increment in the friction factor, compared to the smooth receiver, remains nearly constant at each Reynolds number. It should be noted that in some pairs of cases, the friction factor is exactly the same since the receiver tube is merely rotated around its axes and the thermophysical properties are kept constant (see, for example, 4FCase3 and 4FCase4 or 6FCase1 and 6FCase2).

As discussed in Subsection 3.3.2, heat transfer is evaluated not only in terms of the inner Nusselt number Nu_i, as is commonly reported in the literature, but also with reference to the overall Nusselt number Nu_o. Both Nu_i and Nu_o exhibit an increasing trend with rising Reynolds number and fin count, as illustrated in Fig.4.12 (c)-(f). In the specific case of configurations with two fins, Figure 4.12 (c) shows that Nu_i is markedly higher for configuration 2FCase2 (fins located on the cold side) compared to 2FCase1 (fins on the hot side), which behaves similarly to a smooth tube. However, this apparent enhancement in 2FCase2 is misleading, as it primarily results from the fins being at a temperature nearly equal to that of the surrounding fluid,

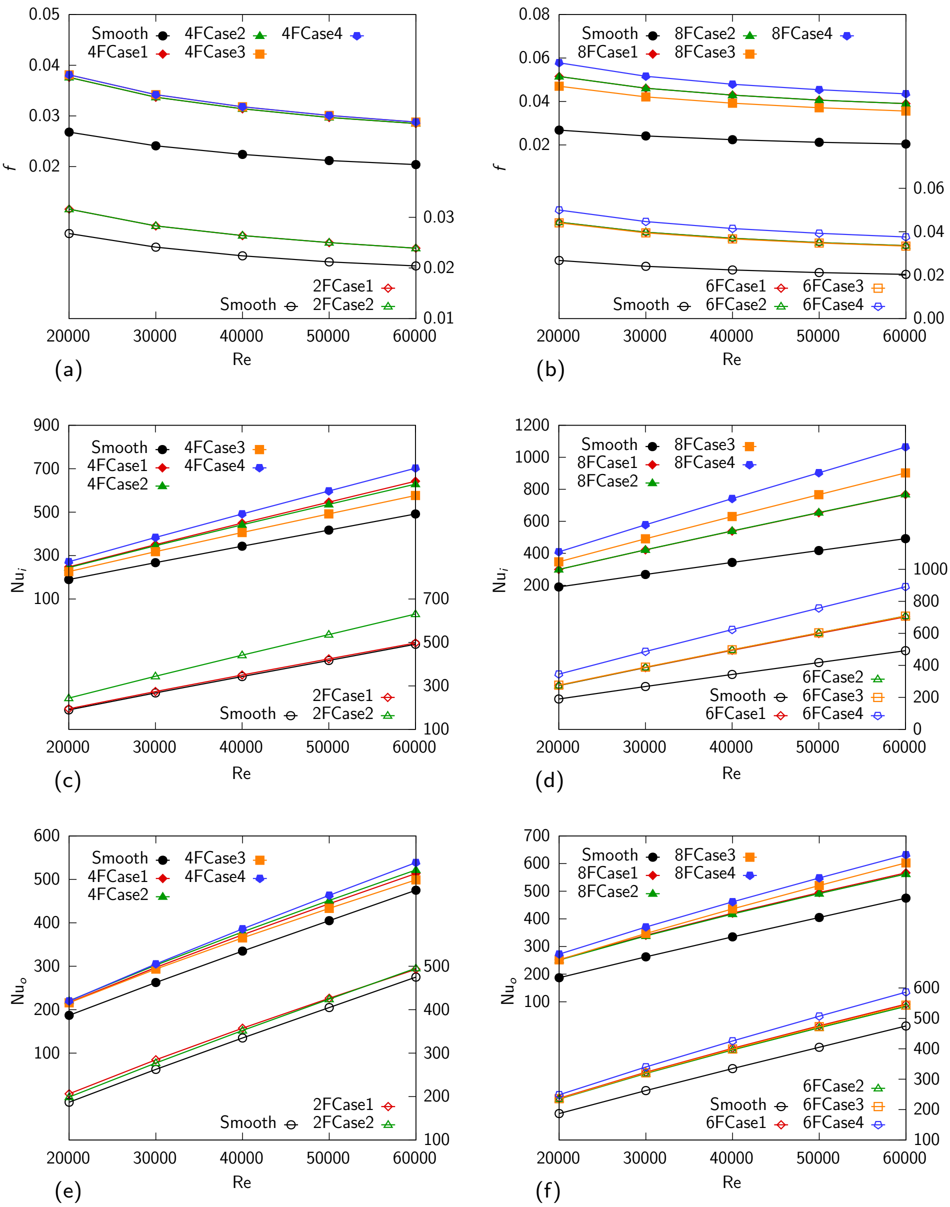

FIGURE 4.12: Variation of f, Nu_i, and Nu_o with Re for all the cases considered.

as previously discussed. This effect results in a significantly reduced area-weighted average temperature T_{ri} on the inner surface of the receiver, which in turn leads to increased values of the convective heat transfer coefficient h_i and the inner Nusselt number Nu_i, as defined in Equations (3.15) and (3.17). However, given that the overall thermal performance of the receiver is primarily influenced by thermal losses from its external surface, the overall Nusselt number Nu_o is a more appropriate metric for evaluation. This parameter inherently accounts for the thermal effect of the fins. As already mentioned in Subsection 3.3.2, the classical definition of fin efficiency is of limited usefulness in the present context, where the heat flux is not uniform. To support this statement, the thermal efficiency of the fins was evaluated for two configurations: 2FCase1 (fins located on the hot/lower side) and 2FCase2 (fins located on the cold/upper side) for an intermediate value of Re = 40,000. This was achieved by performing numerical simulations in which only the thermal conductivity of the fins was artificially set to a very high value (2000 W/mK), effectively approximating infinite conductivity. This approach allowed the estimation of the heat flux exchanged by an isothermal fin, while maintaining a non-uniform receiver temperature consistent with the actual heat flux distribution. The fin efficiency was then calculated as the ratio between the heat flow exchanged with the real fin conductivity and that obtained in the infinite-conductivity case. The resulting efficiencies were 80.2% for 2FCase1 (fins on the hot side) and 78.7% for 2FCase2 (fins on the cold side). These two values are very similar, which is not surprising. In both configurations, the fins have identical geometry and material properties, and the flow field around them is the same, since the simulations neglect gravity effects and temperature-dependent properties. However, the overall thermal impact of the fins differs significantly between the two cases. As already observed for 2FCase2, the temperature of the fins, and consequently the temperature at their base, is very close to that of the surrounding fluid. Therefore, their contribution to heat transfer is negligible, despite their thermal efficiency being comparable to that of the fins in 2FCase1. In contrast, in 2FCase1 the fins operate at a much higher temperature relative to the surrounding fluid, leading to a substantially greater thermal effect.

As illustrated in Fig. 4.12(e), configurations 2FCase1 and 2FCase2 exhibit similar behavior in terms of Nu_o, and both demonstrate superior performance compared to the smooth tube. These findings support the conclusion that, under conditions of non-uniform heat flux and asymmetric fin distribution, performance assessment should be based on the overall Nusselt number, as proposed in this chapter, rather than solely on the inner Nusselt number, as is commonly done in the literature. Regarding fin length, Figure Fig. 4.12(e) shows that configuration 4FCase4, featuring shorter fins on the lower half and longer fins on the upper half of the receiver, outperforms 4FCase3, which has the opposite fin arrangement, despite both configurations exhibiting the same friction factor. This improvement can be attributed to the increased thermal efficiency resulting from shorter fins on the hot side, which outweighs the corresponding reduction in heat exchange area. Additionally, longer fins on the cold side promote the displacement of the high-velocity zone of the heat transfer fluid flow toward the hot region, further enhancing thermal performance. Consistent trends are observed in Figs. 4.12(e) and (f), where the highest overall Nusselt numbers are associated with configurations featuring shorter fins on the lower half and longer fins on the upper half. Specifically, for configurations 4FCase4, 6FCase4, and 8FCase4, the average enhancements in Nu_o are 15.4%, 27.7%, and 38.6%, respectively.

Although the addition of fins enhances the Nusselt number, it also leads to an increase in the friction factor and, consequently, in the required pumping power. To account for both thermal and hydraulic performance, two performance evaluation criteria are considered: PEC_i, based on the inner Nusselt number and defined by Equation (3.19), as shown in Fig. 4.13(a) and (b), and PEC_o, based on the overall Nusselt number and defined by Equation (3.20), as shown in Fig. 4.13(c) and (d). These two metrics can yield significantly different assessments of performance, as exemplified by the previously considered two-fin example. From Fig. 4.13(a), it is evident that the configuration with fins on the cold side (2FCase2) substantially outperforms the configuration with fins on the hot side (2FCase1), a result attributable to the higher inner Nusselt number arising from a lower area-weighted average temperature, as previously discussed. As shown in Fig. 4.13(c), configuration 2FCase1 generally yields the best overall performance, with the exception of the highest Reynolds number considered. Given that the primary focus is on the overall thermal performance of the receiver, and considering that thermal losses are governed by the temperature of the external surface, the performance evaluation should be based on PEC_o. In contrast, reliance on the internal criterion PEC_i may lead to misleading conclusions. Finally, while PEC_i remains relatively constant across the range of Reynolds numbers, PEC_o exhibits a decreasing trend as the Reynolds number increases.

One possible explanation for these trends lies in the Reynolds analogy, which suggests a proportional relationship between heat transfer and friction factor in internal flows. This analogy appears to hold for the inner Nusselt number Nu_i, and the friction factor f, both of which exhibit similar dependence on the Reynolds number Re. However, when evaluating overall performance, where the effect of fin efficiency is incorporated into the overall Nusselt number Nu_o, this relationship no longer holds, and the behavior of Nu_o with respect to Re changes. For large-scale solar thermal applications, this implies that at a constant pumping power, the relative

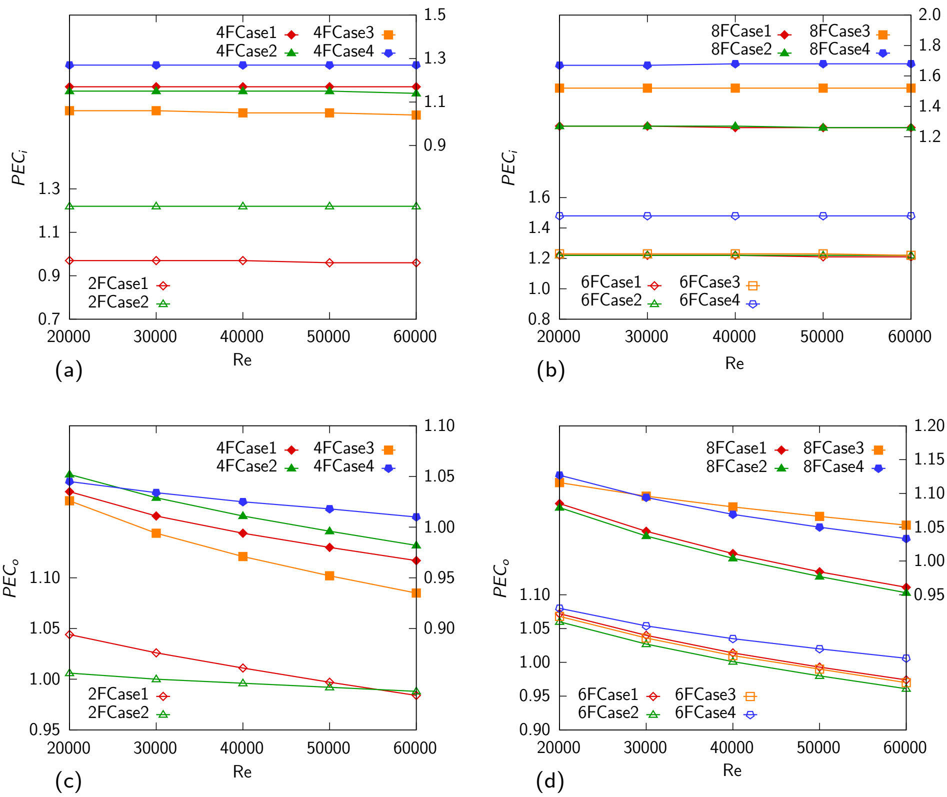

FIGURE 4.13: Variation of PEC_i and PEC_o with Re.

advantage of finned receivers over smooth ones diminishes as the mass flow rate, and thus the Reynolds number, increases.

At low Reynolds numbers, the values of the external performance evaluation criterion PEC_o exceed unity, reaching a maximum of 1.14 for configuration 8FCase4. However, as the Reynolds number increases, PEC_o values progressively decline and eventually fall below 1. Despite this reduction, configurations such as 4FCase4, 6FCase4, and 8FCase4 still offer significant advantages, including lower peak temperatures within the receiver and, as will be demonstrated in the following subsections, reduced thermal losses.

4.3.5 Heat losses

Heat losses Q_{loss} negatively impact the thermal performance of parabolic trough receiver (PTR) tubes by reducing the net radiative heat transfer to the heat transfer fluid (HTF). Maintaining a high-quality vacuum in the annular space between the absorber tube and the glass envelope is essential to minimize these losses. However, in the presence of air infiltration, as assumed in this chapter and described in Section 3.3, heat losses occur due to both radiation and conduction through the air in the annulus. Under the boundary conditions considered, conductive losses are estimated to be approximately one-sixth of the radiative losses. The total heat loss is ultimately dissipated to the ambient environment via forced convection and radiation from the outer surface of the glass envelope. Table 4.4 presents the heat losses per unit length for both smooth and finned receiver configurations across a range of Reynolds numbers.

As the Reynolds number increases from $20,000$ to $60,000$, heat losses decrease for all configurations, primarily due to the reduction in the temperatures of both the absorber tube and the glass envelope. At a fixed Reynolds number, finned receivers consistently exhibit lower heat losses compared to the smooth tube, with greater reductions observed as the number of fins increases. Among the finned configurations, those with longer fins on the upper half and shorter fins on the lower half of the receiver (i.e., 4FCase4, 6FCase4, and 8FCase4) demonstrate superior overall performance, as discussed in previous sections. The most significant reductions in heat loss are observed at the lowest Reynolds number, with decreases of 9.3%, 14.0%, and 18.0% for 4FCase4, 6FCase4, and 8FCase4, respectively, relative to the smooth tube configuration.

TABLE 4.4: Heat losses per unit length Q_{loss} [W/m] for smooth and finned receiver tubes at different Reynolds numbers.

Case | Re $\rightarrow$	20,000	30,000	40,000	50,000	60,000
Smooth	830.3	671.1	593.6	548.3	518.1
2FCase1	777.0	642.4	576.5	537.3	511.3
2FCase2	800.8	653.6	581.4	539.2	511.1
4FCase1	763.3	634.5	570.5	532.5	507.0
4FCase2	748.7	624.7	563.6	527.3	503.0
4FCase3	759.4	634.9	572.7	535.3	510.2
4FCase4	753.1	623.8	560.5	523.5	499.0
6FCase1	721.2	608.7	552.9	519.6	497.2
6FCase2	727.4	613.4	556.7	52.7	499.8
6FCase3	725.6	611.4	554.9	521.1	498.5
6FCase4	713.9	600.9	545.2	512.2	490.1
8FCase1	698.6	595.7	544.5	513.8	493.0
8FCase2	701.3	597.7	546.2	515.2	494.2
8FCase3	701.3	591.7	538.1	506.4	485.3
8FCase4	681.7	580.9	531.0	501.3	481.3

4.4 Conclusions

This chapter presents a comprehensive numerical investigation of a parabolic trough solar receiver tube equipped with longitudinal fins, focusing on the effects of varying the position, number, and length of the fins. The key novelties of this work, in comparison to previous studies in the field, are summarized as follows:

- The novel concept of asymmetrically distributed fins, both in terms of height and circumferential position, is introduced to enhance the thermal performance of the receiver under non-uniform heat flux conditions.
- The distinct heat transfer mechanisms associated with fins located on the upper (high heat flux) and lower (low heat flux) halves of the receiver tube are analyzed in detail, highlighting their different contributions to overall performance.

- A novel approach to evaluating the overall performance of finned receiver tubes subjected to non-uniform heat flux is proposed. This method proves more effective in identifying the best fin configurations than the common approach found in the literature.

The major findings of this chapter can be summarized as follows:

- To minimize peak temperatures and circumferential temperature gradients in both the absorber tube and the glass envelope, it is recommended to place fins in regions subject to higher local heat fluxes.

- Fins located on the lower half of the receiver, where the heat flux is higher, enhance conductive heat transfer. Conversely, fins on the upper (colder) half of the receiver promote the displacement of the high-velocity region of the HTF flow toward the lower half, thereby increasing local convective heat transfer. By strategically combining these effects, i.e., using longer fins on the upper half and shorter fins on the lower half, both conductive and convective heat transfer can be effectively enhanced.

- For the best-performing configurations, i.e., 4FCase4, 6FCase4, and 8FCase4, the maximum improvements in the overall Nusselt number relative to the smooth tube case were 17.6%, 33.0%, and 45.6%, respectively. The corresponding peak values of the external performance evaluation criterion were 1.03, 1.08, and 1.14.

- Compared to the smooth tube, the maximum reductions in peak temperature were 20.8 K, 27.7 K, and 36.2 K for 4FCase4, 6FCase4, and 8FCase4, respectively. Additionally, the maximum reductions in heat loss for these configurations were 9.3%, 14.0%, and 18.0%, respectively.

Longitudinal fins represent a simple, cost-effective, and easily manufacturable solution that can be readily implemented in practical parabolic trough receivers. As demonstrated in this chapter, when fins are strategically positioned and dimensioned, particularly with varying lengths on the upper and lower halves of the receiver, they can significantly enhance thermal performance. The findings presented herein offer valuable insights for improving the efficiency of parabolic trough receivers, thereby reducing the risk of structural deformation and contributing to the extension of the operational lifespan of linear solar collector systems.

Chapter 5

Effect of Vacuum Level on Heat Losses in Smooth and Finned Parabolic Trough Receivers

This chapter presents a comprehensive numerical analysis of heat loss in smooth and longitudinally finned Parabolic Trough Receiver (PTR) tubes under different vacuum levels. The finned receiver configuration examined in this chapter aligns with the optimal design outlined in Chapter 4, named as 8FCase3. This design has been shown to enhance internal heat transfer, reduce the circumferential temperature difference, and minimise heat losses. The coupled heat transfer model described in Chapter 3 was employed to investigate the effects of different vacuum levels and different atmospheric conditions on total heat loss for different inlet bulk temperatures $T_{b,in}$ (500 K, 600 K, and 700 K). An effective thermal-conductivity model for air in the annular region, spanning full vacuum to atmospheric conditions, was used in the analysis. The results show that heat loss increases significantly with higher annulus pressure and heat transfer fluid inlet temperature. Although radiation loss remains roughly constant, conduction loss increases dramatically. Using longitudinal fins reduces the temperature of the receiver and the temperature of the glass cover, and lowers overall heat loss by 9%. This study focuses on the importance of controlling the vacuum level and PTR design in solar thermal concentrator systems (CSTs) to improve thermal performance and reduce operating costs.

5.1 System description and identification of heat losses

This chapter represents an extension of the analysis presented in Chapter 4, focusing specifically on the influence of vacuum level on the thermal losses of parabolic trough receivers. While Chapter 4 addressed internal heat-transfer enhancement using optimized longitudinal fin configurations under non-uniform solar flux, the present chapter investigates how different vacuum conditions in the annular space affect the overall heat-loss behaviour of both smooth and finned receivers.

The schematics of the smooth and longitudinally finned PTRs investigated in this chapter are shown in Figure 5.1 (a) and (b), respectively. The inner diameter of the receiver tube D_{ri} is 66 mm, while its outer diameter D_{ro} is 70 mm; the inner diameter of the glass cover D_{gi} is 109 mm, while its outer diameter D_{go} is 115 mm. The receiver is made of steel, the glass cover material is Pyrex and the heat transfer fluid is the commercial Syltherm 800. The thermophysical properties of these materials are listed in Table 5.1, where ρ is density, c_p is specific heat, λ is thermal conductivity and μ is viscosity.

Heat transfer in the PTR occurs as the total solar radiation Q_{tot} reaches the outer surface of the receiver tube, passing through the glass cover and the annular region. The useful fraction of heat Q_u is then transferred by conduction in the receiver tube and finally by convection to the heat transfer fluid. Heat losses, equal to $Q_{loss} = Q_{tot} - Q_u$, are the sum of radiation heat loss $Q_{loss,rad}$ and conduction heat loss $Q_{loss,cond}$ in the annular space between

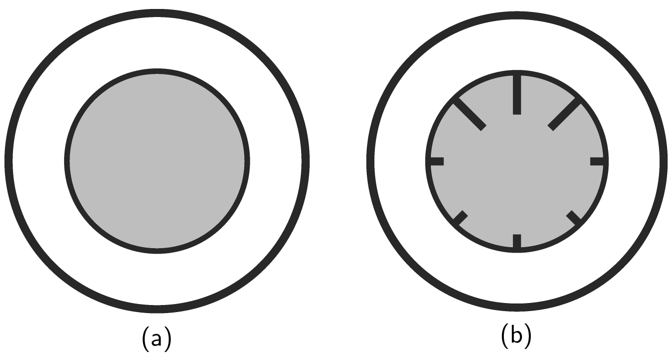

FIGURE 5.1: Different receiver tubes: smooth (a) and finned (8FCase3) (b).

TABLE 5.1: Thermophysical properties of HTF, receiver tube, and glass cover.

Domain	ρ (kg/m^3)	c_p (J/kg·K)	λ (W/m·K)	μ (Pa·s)
Stainless steel	8030	502.48	24.92	
Pyrex	2230	900	1.2	
Syltherm oil ($T_{b,in}$=500 K)	747.2	1962	0.0961	8.4e-4
Syltherm oil ($T_{b,in}$=600 K)	640	2133	0.0773	3.9e-4
Syltherm oil ($T_{b,in}$=700 K)	640	2133	0.0773	3.9e-4

the receiver tube and the glass cover. Heat losses are then transferred to the environment by conduction through the glass cover and finally by convection and radiation, as illustrated in Figure 5.2.

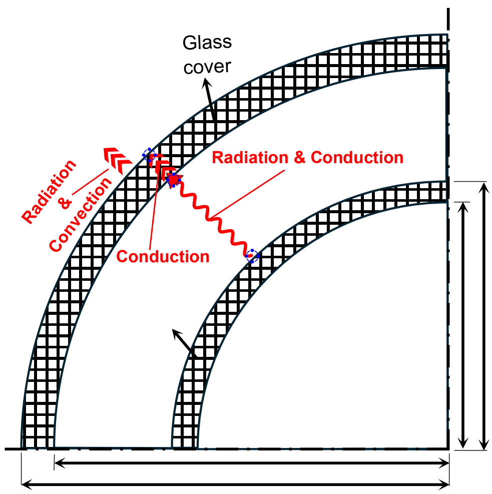

FIGURE 5.2: Schematic of heat losses in the PTR.

As mentioned above, heat losses Q_{loss} are largely dependent on the heat transfer phenomena taking place in the annular space between the receiver tube and the glass cover. The annular space is typically evacuated to 0.0001 torr (0.0133 Pa). At this vacuum level, heat losses are mainly due to radiation, while conduction heat loss is negligible. However, as the pressure in the annular space increases, the heat loss due to molecular conduction $Q_{loss,cond}$ increases significantly and natural convection can also arise, while the radiation loss $Q_{loss,rad}$ remains almost constant. The energy balance equation for the receiver can be written as

$$Q_{loss} = Q_{tot} - Q_u = Q_{loss,rad} + Q_{loss,cond} \tag{5.1}$$

5.2 Numerical Analysis

A detailed description of the governing equations, turbulence modelling, numerical schemes, and radiation treatment adopted in this work is provided in Chapter 3. The present section therefore, summarizes and focuses on the specific modelling choices relevant to the analyses presented in this chapter, where the numerical investigation of a parabolic trough receiver was carried out using ANSYS Fluent 2025R1. In real PTSC systems, the PTR tubes are very long as they are welded in series to absorb solar energy and achieve the required temperature. In this work, to save computational time, only a small portion of the system of length L equal to D_{ro} was investigated by imposing periodic inlet-outlet boundary conditions. The heat transfer fluid, Syltherm 800, was assumed to be incompressible and Newtonian with constant thermophysical properties, as discussed in the previous section. The second-order upwind scheme was adopted for the discretisation of the governing equations and the SST $k-\omega$ model was employed as the HTF flow is fully turbulent. The numerical solution employs a coupled pressure-velocity scheme. The annular space between the receiver tube and the glass cover was considered as a fluid domain, although it still contains air (zero velocity) at low pressure. The heat transfer in this region, due to conduction and convection, was taken into account by an effective conductivity, as explained in the following subsection. Finally, radiative heat transfer between the receiver tube and the glass cover was modelled using the Surface-to-Surface (S2S) radiation approach. The simulations were considered to have reached convergence when the residuals were less than 10^{-6}.

5.2.1 Effective thermal conductivity model

A simple but effective method of avoiding the need to calculate the flow field in the annular region of the PTR filled with air or other gases at different pressures is to impose a zero velocity field, thereby solving a simple conduction problem, and defining an equivalent or effective thermal conductivity k_{eff} that includes both the effects of conduction and, if relevant, natural convection. The present study considers air in the annulus at various pressures ranging from 0.001 torr to 760 torr (i.e. from 0.00013 kPa to 100 kPa). The model for calculating effective thermal conductivity, based on gas type and pressure, was implemented in the Engineering Equation Solver (EES) software [110].

If the pressure is lower than 1 torr ($\simeq$ 0.1 kPa), the effective thermal conductivity is defined as [111]

$$k_{eff} = \frac{D_{ro} \cdot h_{ro,gi} \cdot \ln\left(\frac{D_{gi}}{D_{ro}}\right)}{2} \tag{5.2}$$

where $h_{ro,gi}$ is the heat transfer coefficient by free molecular convection at $T_{ro,gi}$ = $(T_{ro}$+$T_{gi})/2$ which is defined as

$$h_{ro,gi} = \frac{k_{std}}{\frac{D_{ro}}{2}\ln\left(\frac{D_{gi}}{D_{ro}}\right) + b \cdot \lambda \cdot \left(\frac{D_{ro}}{D_{gi}} + 1\right)} \tag{5.3}$$

In the above equation, k_{std} is the thermal conductivity of air at room temperature, b is an interaction coefficient and λ is the mean-free-path of a molecule calculated as follows

$$\lambda = \frac{2.331 * E(-20) \cdot (T_{ro,gi} + T_0)}{P \cdot \delta^2} \tag{5.4}$$

where P is the pressure in the annulus and δ is the molecular diameter.

If the pressure in the annular space is greater than 1 torr ($\simeq$ 0.1 kPa), the effective thermal conductivity includes the effects of both conduction and natural convection and is defined as [112]

$$k_{eff} = 0.386 \cdot k \left(\frac{\mathrm{Pr}}{0.861 + \mathrm{Pr}}\right)^{\frac{1}{4}} \cdot \mathrm{Ra}_c^{\frac{1}{4}} \tag{5.5}$$

where k is the molecular thermal conductivity at $T_{ro,gi}$. Both the Prandtl number Pr and the Rayleigh number Ra_c of the annular cavity depend on the pressure through density.

5.2.2 Validation

The hexahedral conformal meshes used throughout the computational domain for smooth and finned receivers share the same characteristics as those used in Chapter 2. As the glass cover and the vacuum annulus are also considered in this study, a new mesh independence test has been performed. The number of elements in each mesh has been increased by 50% compared to the previous one. The receiver's mean outer surface temperature and the pressure gradient were monitored. The solution was considered to be mesh-independent when the maximum variation in the above parameters was less than 0.1%. The final meshes used for the simulations consist of 165,740 and 236,310 elements for the smooth and the finned receiver, respectively.

The heat loss data, including the effect of the vacuum cavity, were validated here for different pressures in the annulus cavity against those reported by Forristal [80] for a parabolic trough receiver with the following operative conditions: HTF temperature of 350°C, volumetric flow rate of 140 gpm, DNI equal to 950 W/m^2, wind speed of 1 m/s, and ambient temperature of 35°C. The numerical results agree well with those obtained using the Forristal model, as shown in Figure 5.3. The mean deviation for the heat loss per unit length is equal to 4.7%. Slightly higher differences

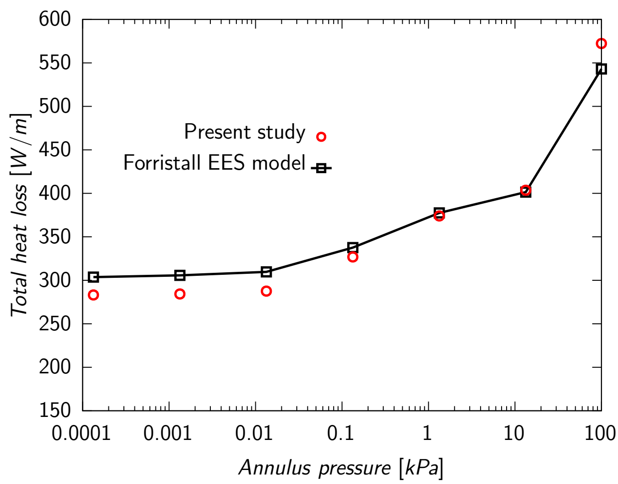

FIGURE 5.3: Validation of heat loss data for different annulus pressures.

were observed at very low annulus pressures. It should be noted that the present study is based on a multidimensional CFD model developed in ANSYS Fluent, whereas the Forristall model is a one-dimensional analytical formulation. Under near-vacuum conditions, heat transfer becomes dominated by radiation and rarefied gas conduction, making the predicted losses sensitive to the modelling approach. However, heat losses at full vacuum are significantly lower overall, so the slightly larger relative difference does not have a substantial practical impact. At higher pressures, the heat losses increase considerably, but the discrepancy between the two models becomes much smaller.

5.3 Results and discussion

The two receiver geometries in Figure 5.1 (a) and (b) were numerically analysed in the hypothesis of air in the vacuum region at pressures ranging from 0.00013 kPa to 100 kPa.

The temperature distributions at the middle section of the computational domain of the receiver for different inlet bulk temperatures $T_{b,in}$ and annular space pressures are shown in Figure 5.4. For a given $T_{b,in}$, at a lower vacuum region pressure only radiation loss occurs and the glass temperature is lower compared to that at a higher annulus pressure, where the effective conductivity becomes larger. As can be seen, adding fins reduces the receiver outer surface temperature T_{ro}, further reducing the glass temperature. Glass and receiver tube temperatures are obviously higher at higher $T_{b,in}$.

Figure 5.5 shows the receiver and glass cover outer surface temperatures at $T_{b,in}$ = 600 K. It is observed that as pressure increases, the receiver's outer surface temperature decreases very little, but the glass temperature increases much more at higher pressure. Since it depends on effective thermal conductivity, as pressure increases, the effective thermal conductivity increases, which increases heat conduction between the receiver's outer surface and the glass cover.

Figure 5.6 shows the fraction of radiation and conduction heat losses in the annulus for different pressures and for two values of the HTF upstream mean bulk temperature $T_{b,in}$ = 500, 600 K, and 700 K. The figure refers to a smooth tube; however, almost similar results are obtained for the finned case. At lower vacuum pressures, radiation is dominant, and conduction heat

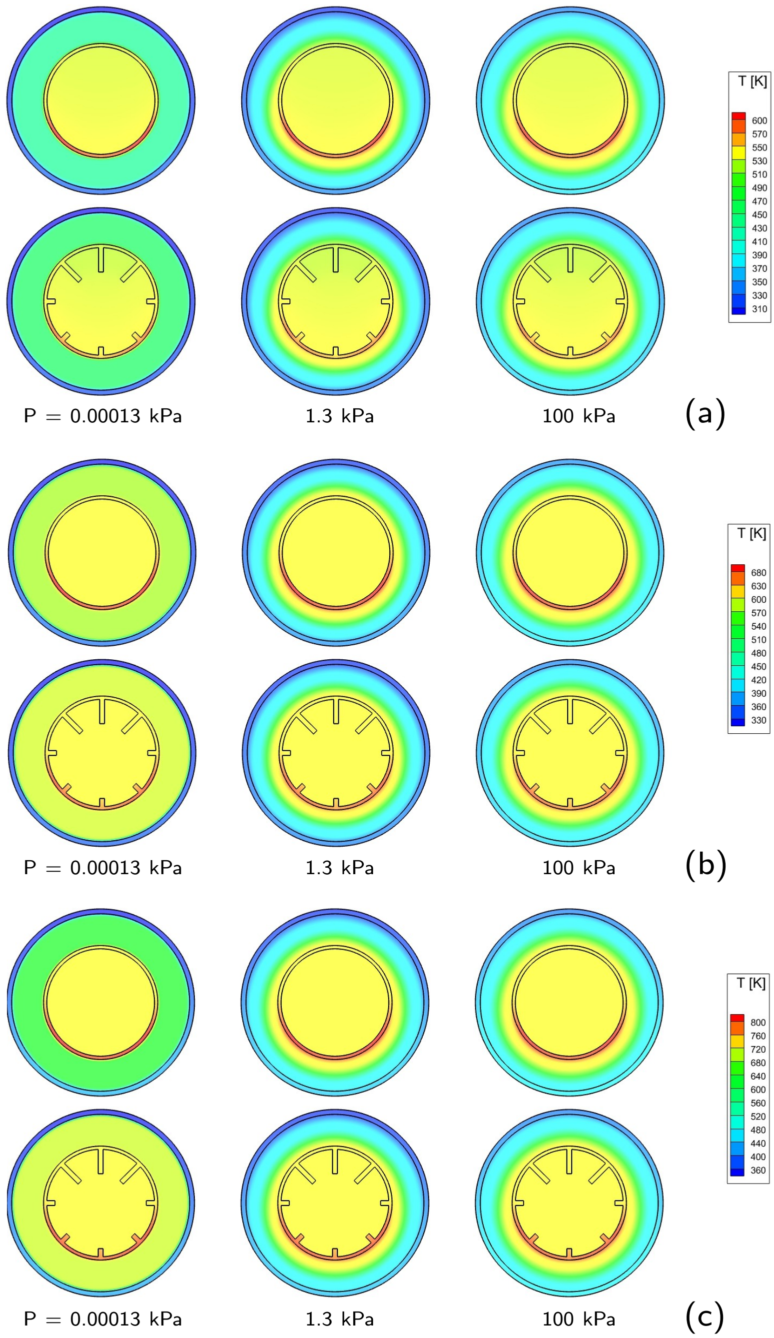

FIGURE 5.4: Temperature contours for different annulus pressures: (a) $T_{b,in}$ = 500 K, (b) $T_{b,in}$ = 600 K, and (c) $T_{b,in}$ = 700 K.

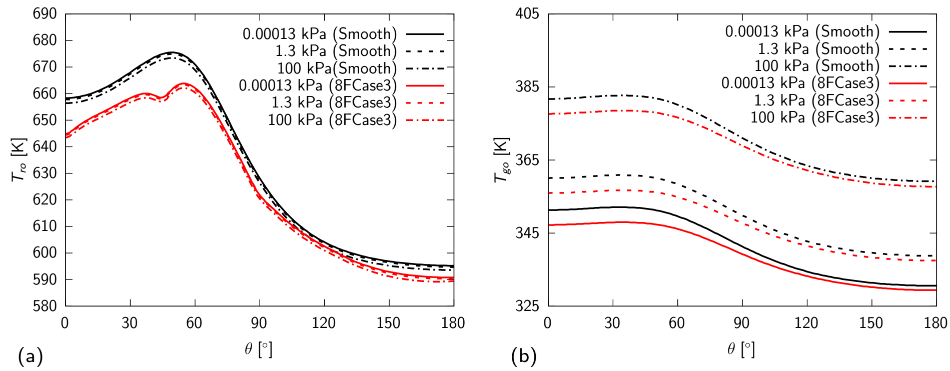

FIGURE 5.5: Receiver and glass cover outer surface temperature (T_{in} = 600 K).

loss is almost negligible. As the pressure increases, the fraction of radiation heat loss decreases and, due to the effect of higher effective conductivity, the fraction of conduction heat loss increases. As expected, as $T_{b,in}$ increases, the fraction of radiation heat loss increases due to the higher temperature of the receiver tube, and the fraction of conduction heat loss decreases.

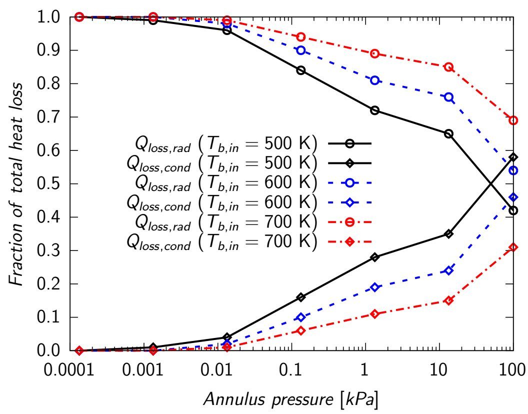

FIGURE 5.6: Fraction of radiation and conduction heat losses in the annulus for different pressures.

Total heat loss Q_{loss}, radiation heat loss $Q_{loss,rad}$, and conduction heat loss $Q_{loss,cond}$ per unit length of receiver are presented in Figure 5.7 for smooth and finned tubes and at different vacuum pressures and bulk upstream

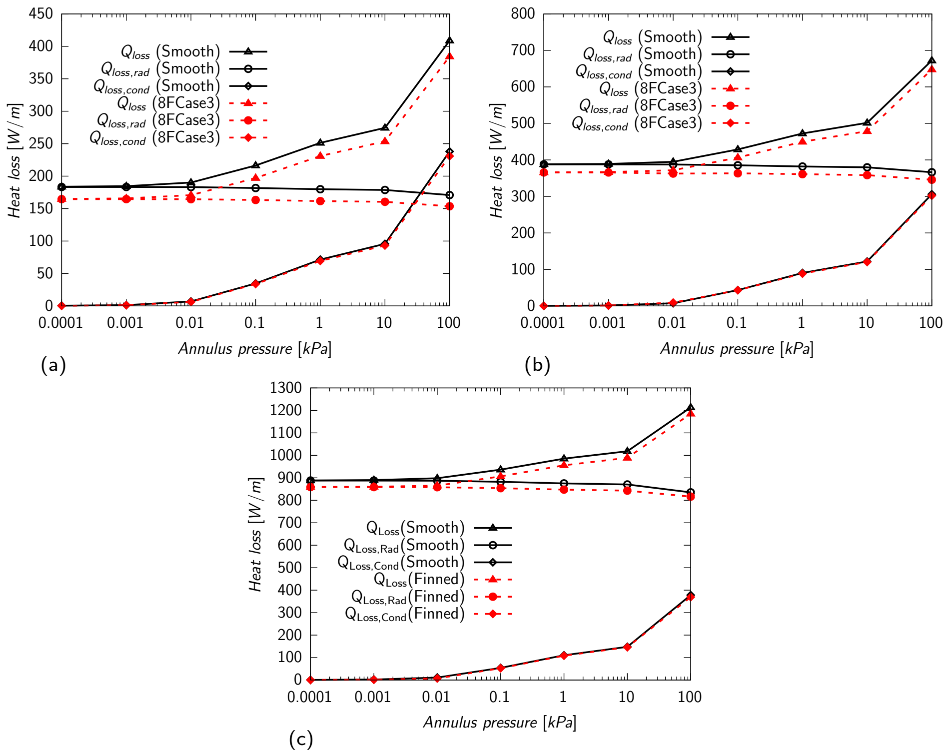

FIGURE 5.7: Heat loss per unit length for different pressures: (a) $T_{b,in}$ = 500 K, (b) $T_{b,in}$ = 600 K, and $T_{b,in}$ = 700 K.

temperatures $T_{b,in}$. For a given HTF bulk upstream temperature, as the annulus pressure increases, the heat loss due to molecular conduction and natural convection increases significantly, while the radiation loss remains almost constant. As expected, heat loss increases with increasing HTF upstream temperature. The addition of fins (red dashed lines in Figure 5.7) reduces the total heat loss, but this effect is mainly due to the reduction in radiation loss, while conduction loss remains almost the same. The average reduction in total heat loss for the finned receiver compared to the smooth one is 9%, 5.2%, and 3 .2% for $T_{b,in}$ = 500 K, 600 K, and 700 K, respectively.

Finally, Tables 5.2 and 5.3 show the effect of different atmospheric conditions (ambient temperature T_{amb} equal to 288 K and 308 K, wind speed v_w equal to 2.5 m/s and 4.5 m/s) on heat losses and glass/receiver outer surface temperatures under various vacuum conditions for smooth and finned receivers, respectively, at $T_{b,in}$ = 500 K.

TABLE 5.2: Heat loss per unit length and glass/receiver outer surface temperatures for smooth receiver at different atmospheric conditions.

v_w (m/s)	T_{amb} (K)	P (kPa)	Q_{loss} (W/m)	$Q_{loss,rad}$ (W/m)	T_{ro} (K)	T_{go} (K)
2.5	288	0.00013	185.9	185.7	545.8	309.3
		1.3	256.4	182.4	545.2	316.9
		100	420.0	173.3	543.8	335.9
2.5	298	0.00013	183.4	183.3	545.8	318.3
		1.3	251.3	179.9	545.2	325.5
		100	408.9	170.9	543.9	343.4
2.5	308	0.00013	180.7	180.7	545.9	327.3
		1.3	246.0	177.3	545.3	334.0
		100	397.6	168.1	544.0	350.9
4.5	288	0.00013	187.0	187.0	545.8	304.5
		1.3	260.0	184.3	545.2	310.7
		100	433.6	176.1	543.7	326.7
4.5	298	0.00013	184.7	184.7	545.8	313.8
		1.3	254.9	181.7	545.2	319.7
		100	421.7	173.7	543.8	334.8
4.5	308	0.00013	182.0	182.0	545.8	323.2
		1.3	249.4	179.0	545.3	328.6
		100	409.9	171.0	543.9	342.9

Results indicate that for a given wind speed, heat loss is higher at lower ambient temperatures, and for a given ambient temperature, heat loss increases with increasing wind speed. The effect of ambient temperature is slightly higher than that of wind speed, but both are smaller than that of pressure in the annular region. Comparing Tables 5.2 and 5.3 it can again be concluded that finned receiver tubes can effectively reduce heat losses.

TABLE 5.3: Heat loss per unit length and glass/receiver outer surface temperatures for finned receiver (8FCase3) at different atmospheric conditions.

v_w (m/s)	T_{amb} (K)	P (kPa)	Q_{loss} (W/m)	$Q_{loss,rad}$ (W/m)	T_{ro} (K)	T_{go} (K)
2.5	288	0.00013	167.0	167.0	536.2	307.0
		1.3	236.0	164.0	535.7	314.4
		100	395.6	156.0	534.5	333.1
2.5	298	0.00013	164.7	164.6	536.2	316.1
		1.3	231.0	161.6	535.7	323.1
		100	384.4	153.6	534.6	340.6
2.5	308	0.00013	162.0	162.0	536.3	325.2
		1.3	225.7	159.0	535.8	331.7
		100	373.0	151.0	534.7	348.2
4.5	288	0.00013	168.0	168.0	536.2	302.7
		1.3	239.3	165.6	535.7	308.7
		100	408.3	158.6	534.5	324.4
4.5	298	0.00013	165.7	165.7	536.2	312.1
		1.3	234.1	163.1	535.7	317.7
		101.325	396.4	156.3	534.5	332.5
4.5	308	0.00013	163.1	163.1	536.2	321.5
		1.3	228.9	160.6	535.8	326.8
		100	384.4	153.7	534.6	340.7

5.4 Conclusions

The study described in this chapter investigates the effect of annular region pressure, inlet heat transfer fluid bulk temperature, and atmospheric conditions on heat loss in the parabolic trough receiver. The results show that conduction heat loss is very small at lower vacuum pressures, with radiation being the dominant phenomenon. However, as the pressure in the annular space increases, the proportion of radiation heat loss to total heat loss decreases due to the significant conduction heat loss. Heat loss with air in the annular region at atmospheric pressure is almost double that at full vacuum. The addition of fins successfully reduces the outer surface temperature of the receiver, minimising mainly radiation loss. The total heat loss is reduced by 9% in comparison with the smooth receiver. It was also observed that atmospheric conditions also play a role, as heat loss increases with wind speed and lower ambient temperatures.

Chapter 6

Effect of Vacuum Degradation on Heat Losses in Parabolic Trough Collector Receivers

In this chapter, the thermal performance of linear evacuated receivers designed for parabolic trough collector (PTC) systems was investigated under varying operating conditions. A parametric thermal analysis was performed for a stainless steel receiver tube with Therminol® VP-1 as the heat transfer fluid. This fluid can produce low-boiling-point compounds, including hydrogen, which permeate through the absorber wall into the evacuated annulus between the absorber and the glass envelope of the receivers. Two annulus conditions were evaluated: a fully evacuated state (10^{-2} mbar) and hydrogen-filled environment (1 mbar). Additionally, the impact of wind speeds (5 and 10 m/s) on key performance parameters was assessed under two extreme operating conditions. Key metrics included temperature and velocity profiles, circumferential temperature gradients, convective heat transfer coefficients, and heat losses. Simulations covered mass flow rates of 3-6 kg/s (in 1 kg/s increments), inlet temperatures from 290 °C to 390 °C (in 20 °C steps), and direct normal irradiance levels of 850 and 1000 W/m^2. Results revealed how these annulus conditions and wind effects influence thermal performance. Hydrogen presence increased heat losses by up to 3 times compared to the evacuated case, with glass temperatures peaking at 142.5 °C. Increasing the mass flow rate from 3 to 6 kg/s reduced the absorber tube's maximum circumferential temperature difference from 39.4 °C to 23.5 °C, with different annulus conditions showing diminished impact on this parameter at higher flow rates. Heat losses increased under windy conditions, whereas the glass temperature decreased significantly, especially for the hydrogen-filled annulus.

6.1 Problem Description and Model Setup

In the previous chapters, the thermal performance of PTC receivers was analysed by progressively incorporating increasing levels of physical realism. Chapter 4 focused on internal heat transfer enhancement using longitudinal fins under circumferentially non-uniform heat flux, employing periodic computational domains to identify optimal fin configurations. Chapter 5 subsequently investigated the influence of vacuum degradation on heat losses in both smooth and finned receivers, analysing radiative and conductive mechanisms over a wide range of annulus pressures.

Although the analyses in Chapter 5 provided fundamental insight into the effect of vacuum degradation, the use of periodic receiver sections and uniform axial conditions does not allow the investigation of several key phenomena observed in real solar thermal plants. In particular, axial temperature variations, buoyancy-driven gas motion in the annulus, wind–receiver interaction, and hydrogen-specific thermal effects cannot be adequately captured using simplified or periodic models. To overcome these limitations, the present extends the previous work to a full-length commercial receiver operating under realistic conditions.

This chapter investigates the effect of hydrogen-induced vacuum degradation on the thermal behaviour and heat losses of a parabolic trough receiver with a total length of 4.06 m. Hydrogen is considered explicitly as the annulus gas, as it is the dominant species responsible for vacuum degradation in operating plants due to thermal decomposition of the HTF and subsequent permeation through the absorber tube wall. As the getter materials become saturated, hydrogen accumulation leads to a progressive loss of vacuum quality, significantly enhancing conductive and convective heat transfer across the annulus.

The three-dimensional conjugate heat-transfer numerical model described in Chapter 3 was to simulate the coupled heat-transfer mechanisms governing receiver performance, simultaneously accounting for:

- turbulent forced convection of the HTF inside the absorber tube,
- heat conduction through the absorber tube and the glass envelope,
- radiative heat transfer across the annular gap,
- gas conduction and natural convection within the annulus under hydrogen-filled conditions,
- external convective heat losses influenced by wind speed.

A schematic representation of the parabolic trough receiver geometry, including the absorber tube, annular region, and glass envelope, together with the principal heat-transfer paths considered in the model, is shown in Figure 6.1, and detailed parameters of the receiver tube model are provided in Table 6.1. The computational domain corresponds to a full-scale commercial receiver, allowing the evaluation of axial temperature development along the absorber and glass envelope.

The non-uniform circumferential heat-flux distribution imposed on the outer surface of the absorber tube is illustrated in Figure 6.2. As shown, the lower half of the receiver is subjected to significantly higher heat flux due to reflected solar radiation from the parabolic mirror, while the upper half receives primarily direct solar irradiation. This realistic flux distribution is essential for accurately predicting circumferential temperature gradients and their interaction with vacuum degradation effects.

Two annulus conditions are analysed:

1. an *ideal vacuum* condition, representing a fully functional receiver in which radiative heat transfer dominates across the annulus, and
2. a *hydrogen-filled annulus*, representing degraded vacuum conditions in which gas conduction and natural convection contribute significantly to total heat losses.

By combining full-length geometry, hydrogen-specific thermophysical properties, and realistic boundary conditions, this modelling framework enables a comprehensive assessment of axial and circumferential thermal behaviour, receiver heat losses, and the interaction between vacuum degradation and external environmental effects under operating conditions representative of commercial parabolic trough power plants.

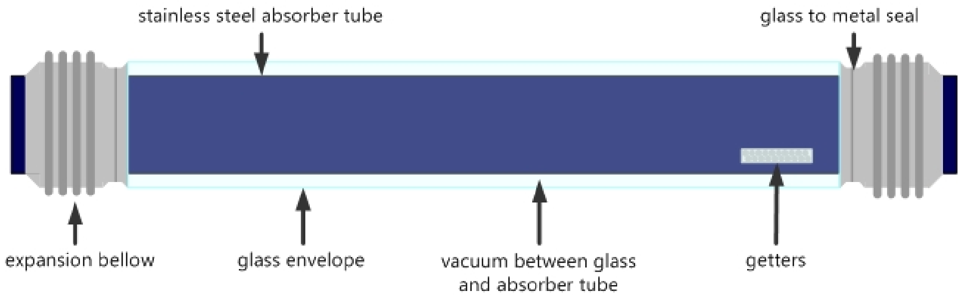

FIGURE 6.1: Schematic of a solar receiver for a parabolic trough collector.

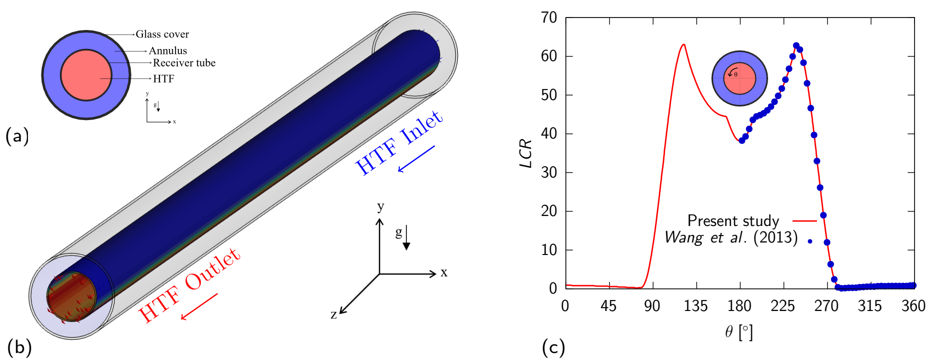

FIGURE 6.2: (a) Cross section of a receiver tube, (b) receiver tube with qualitative heat flux distribution, and (c) heat flux profile.

Commercial PTC solar power plants widely use a eutectic mixture of biphenyl and diphenyl oxide as the heat transfer fluid due to the favorable thermodynamic properties of this synthetic thermal oil. The main materials relevant for the study and their thermophysical properties are discussed in the following subsection.

TABLE 6.1: Solar receiver tube model: main geometrical parameters and operating conditions.

Parameter & Value	
Inner diameter of the receiver tube, D_{ri} (m)	0.066
Outer diameter of the receiver tube, D_{ro} (m)	0.070
Inner diameter of the glass cover, D_{gi} (m)	0.114
Outer diameter of the glass cover, D_{go} (m)	0.120
Length, L (m)	4.06
Inlet HTF temperature, T_{in} (°C)	290, 310, 330, 350, 370, 390
Mass flow rate, $\dot{m}$ (kg/s)	3, 4, 5, 6
Direct normal irradiance, DNI (W/m^2)	850, 1000

6.1.1 Material properties

Receiver

The absorber tube of commercial receivers for PTCs is generally made of stainless steel (grades 316 or 321), which is commonly used in PTC receivers due to its corrosion resistance, mechanical strength, durability, and excellent performance across a wide temperature range. Furthermore, it serves as a chemically and thermally stable substrate for the deposition of selective coatings, which are essential for enhancing the optical efficiency of these solar receivers. The temperature-dependent thermal conductivity of stainless steel λ_r can be evaluated as [113]:

$$\lambda_r = 0.0153 \cdot T_r + 14.775 \tag{6.1}$$

where T_r is the absorber tube temperature in K.

The outer surface of the absorber tube is coated with a material that has a temperature-dependent emissivity given by [113]:

$$\epsilon_{ro} = 0.062 + 2 \cdot 10^{-7} \cdot (T_{ro} - 273.15)^2 \tag{6.2}$$

The glass envelope surrounding the absorber tube is made of borosilicate glass, with a thermal conductivity λ_g of 1.2 W m^{-1} K^{-1} and an emissivity ϵ_g of 0.86.

Annulus material

To model the atmosphere in the annulus space between the absorber tube and the glass tube, two different scenarios are considered in the study: vacuum and low-pressure atmosphere with hydrogen. For hydrogen in the annular space, the density was based on the ideal gas law, and other properties were calculated using the kinetic theory model [114] provided by the CFD software used, i.e. ANSYS Fluent, to analyze conduction and natural convection effects.

Heat Transfer Fluid (HTF)

Therminol® VP-1 was used as the HTF circulating through the receiver tube, as it is widely used in the majority of operating CSP plants worldwide, with an installed capacity exceeding 4.5 to 5 GWe [115]. It is a commercially available eutectic mixture of diphenyl oxide and biphenyl, commonly employed in PTC solar power plants, and is marketed under several trade names, including Dowtherm® A, Therminol® VP-1, etc [116, 117]. It operates effectively up to 400 °C [118].

Due to its low viscosity over the liquid-phase range, it enables efficient heat transfer. However, in environments where ambient temperatures drop below 12 °C, heat tracing is recommended to prevent solidification. The fluid remains thermally stable under normal operating conditions, but overheating may result in the formation of solid deposits on heating exchange surfaces. Additionally, degradation products -such as hydrogen and other low boilers-may accumulate in the vapor phase over time as the fluid ages, even under normal operating conditions. Therefore, proper circulation rates and control of pressure and temperature are essential. The temperature-dependent thermo-physical properties of Therminol® VP-1 are provided in the manufacturer's datasheets [119]. In this study, piecewise polynomials expressions are employed to model these properties for use in simulations and thermal analysis [113].

For the temperature range $285.15\,\mathrm{K} \leq T \leq 698.15\,\mathrm{K}$, the following expressions are considered for the specific heat capacity $c_{p,f}$ (in $\mathrm{J\,kg^{-1}K^{-1}}$), density ρ_f $(\mathrm{kg\,m^{-3}})$, and thermal conductivity λ_f $(\mathrm{W\,m^{-1}\,K^{-1}})$ of the HTF:

$$c_{p,f} = 2.125 \cdot 10^3 - 11.017 \cdot T + 0.049862 \cdot T^2 - 7.7663 \cdot 10^{-5} \cdot T^3 + 4.394 \cdot 10^{-8} \cdot T^4 \tag{6.3}$$

$$\rho_f = 1.4386 \cdot 10^3 - 1.8711 \cdot T + 2.737 \cdot 10^{-3} \cdot T^2 - 2.3793 \cdot 10^{-6} \cdot T^3 \tag{6.4}$$

$$\lambda_f = 0.14644 + 2.0353 \cdot 10^{-5} \cdot T - 1.9367 \cdot 10^{-7} \cdot T^2 + 1.0614 \cdot 10^{-11} \cdot T^3 \tag{6.5}$$

Additionally, for the temperature range $373.15\,\mathrm{K} \leq T \leq 698.15\,\mathrm{K}$, the following expression is valid for the dynamic viscosity μ_f $(\mathrm{mPa \cdot s})$ of the HTF:

$$\mu_f = 23.165 - 0.1476 \cdot T + 3.617 \cdot 10^{-4} \cdot T^2 - 3.9844 \cdot 10^{-7} \cdot T^3 + 1.6543 \cdot 10^{-10} \cdot T^4 \tag{6.6}$$

6.2 Numerical solution method

A detailed description of the governing equations, turbulence modelling, numerical schemes, and radiation treatment adopted in this work is provided in Chapter 3. The present section therefore, summarizes and focuses on the specific modelling choices relevant to the receiver configurations and annular conditions analysed in this chapter. In this study, ANSYS Fluent 2025R1 [98] is employed to perform three-dimensional, steady-state numerical simulations of heat transfer and fluid flow in a parabolic trough receiver. The analysis considers fully developed, incompressible turbulent flow of the heat transfer fluid inside a smooth circular receiver tube. Therminol® VP-1 is used as the working fluid, with temperature-dependent thermophysical properties to accurately capture high-temperature operating conditions.

Turbulence effects in the receiver tube are modelled using the Shear Stress Transport (SST) k–ω model, which provides improved near-wall resolution and reliable prediction of adverse pressure-gradient flows.

The governing transport equations in the annular region between the absorber tube and the glass cover depend on the residual gas composition and pressure. Under high-vacuum conditions, heat transfer in the annulus is dominated by radiation, while conductive and convective contributions become negligible due to the very low gas density. As the annulus pressure increases, conduction and buoyancy-driven convection may contribute to heat transfer. In the present study, two annular atmosphere conditions are analysed: a low-pressure vacuum condition of 10^{-2} mbar and a hydrogen-filled annulus at a pressure of 1 mbar.

For the vacuum case, the annular region is modelled by solving only the energy equation, with fluid flow effects neglected. For the hydrogen-filled annulus, buoyancy-induced natural convection is taken into account. Since the Rayleigh number remains below 1.0×10^8, the flow in the closed annulus is modelled as laminar, and turbulence modelling is disabled in this domain [61]. Under the operating conditions investigated, the Knudsen number based on the annular gap thickness is of the order of 10^{-3}, confirming the validity of the continuum hypothesis.

Radiative heat transfer between the outer surface of the receiver tube and the inner surface of the glass cover is modelled using the Surface-to-Surface (S2S) radiation approach. This model allows the evaluation of radiative exchange between diffuse-grey surfaces and is appropriate for evacuated and low-pressure annular conditions [61, 96].

Heat conduction is solved within the solid domains, namely the stainless steel receiver tube and the borosilicate glass cover. Thermophysical properties are assigned according to the specific material of each domain. In the annular region, where the flow is laminar or suppressed, all turbulence-related terms are omitted.

Pressure–velocity coupling is handled using a coupled solution algorithm, and second-order upwind schemes are employed for the discretization of the governing transport equations. The numerical simulations are considered converged when the residuals of all solved variables fall below 1×10^{-6}.

6.2.1 Grid independence analysis and model validation

Grid independence analysis

To ensure numerical accuracy, five hexahedral meshes with increasing refinement (coarse, with 895,230 elements, to fine, with 3,093,000 elements), were generated using the ANSYS Meshing tool. The meshes were evaluated at one of the operational conditions: inlet temperature T_{in} = 390 °C and maximum mass flow rate $\dot{m}$ = 6 kg/s. The height of the first element on the inner wall of the HTF domain was kept constant across all meshes at 9.8 μm. For the maximum flow rate investigated, this ensured maximum and average dimensionless wall distances y^+ of 3.4 and 2.3, respectively, both consistent with the adopted turbulence model. As shown in Figure 6.3 (a), both key global output parameters (e.g., pressure drop ΔP and average temperature on the outer glass surface $T_{go,avg}$) and a local parameter (e.g., maximum temperature on the outer receiver surface $T_{ro,max}$) showed negligible variation beyond Mesh 4. The maximum temperature on the external surface of the glass was also monitored to assess mesh adequacy for estimating radiative exchange. Similar monotonic behaviors, like those shown in Figure 6.3 and not reported here for brevity, were observed for other global and local parameters, such as HTF outer temperature, average temperature on the outer receiver surface, and maximum outer glass surface temperature, with variations between Mesh 4 and Mesh 5 smaller than 0.08%. Consequently, Mesh 4, which contains 2.61 million elements, was selected as the optimal balance between computational cost and result accuracy. A detailed cross-sectional view of Mesh 4 is provided in Figure 6.3 (b). In the final mesh, the growth rate in the HTF region between the wall and the channel core, where a uniform size mesh was applied, was set to a low value of 1.08 to capture flow structures even away from the wall accurately. The simulations were performed in parallel mode using 8 CPU cores (12th Gen Intel® Core™ i7-12700, 2.10 GHz). A representative steady-state case required 2941 s ($\approx$ 0.82 h) of wall-clock time, corresponding to approximately 6.5 core-hours. These results indicate that the proposed approach is computationally efficient and suitable for parametric studies.

Subsequent validation of the Mesh 4 results against experimental and analytical data is presented in Section 6.2.1.

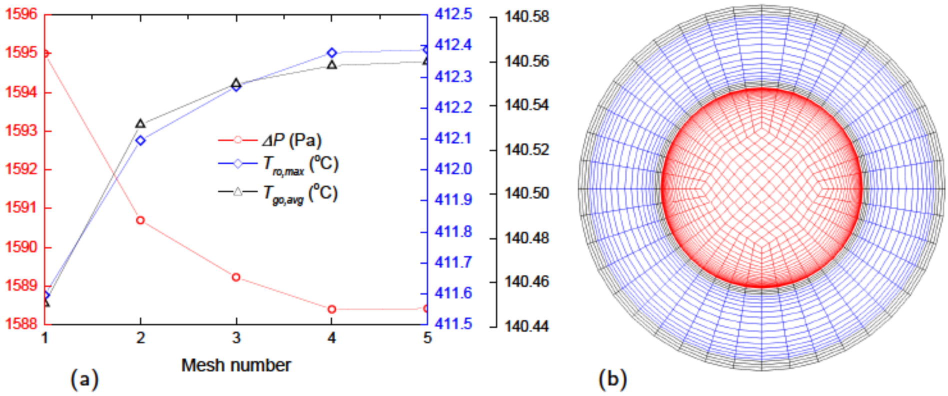

FIGURE 6.3: (a) Grid independence test results; (b) cross-sectional detail of the final mesh for the receiver.

Numerical model validation

The numerical results of the developed parabolic trough receiver model were validated using both empirical correlations and experimental data. First, the pressure drop, expressed in terms of the friction factor, was validated using the Petukhov correlation [120], as shown in Figure 6.4 (a). Similarly, the heat transfer coefficient, characterized by the Nusselt number, was validated using the Gnielinski correlation [109], as shown in Figure 6.4 (b). The mean deviations were 0.96% for the friction factor and 1.4% for the Nusselt number, both of which are low values that further confirm the validity and reliability of the developed model.

Subsequently, the CFD model results were further validated by comparison with laboratory experimental data obtained at the Plataforma Solar de Almería (PSA)-CIEMAT and the National Renewable Energy Laboratory (NREL) [69]. Heat loss (Q_{loss}) and glass cover temperature (T_{go}) were validated under vacuum conditions, as shown in Figure 6.5. As can be seen, the numerical results closely match the experimental data. The mean deviations were 5.5% for heat loss and 3.1% for glass temperature, both of which are low values that further confirm the validity and reliability of the developed model. More details of experimental setups are shown in subsection 2.2.1.

In addition to the vacuum condition, the CFD model was also validated for cases with hydrogen present in the annulus. Experimental data from the

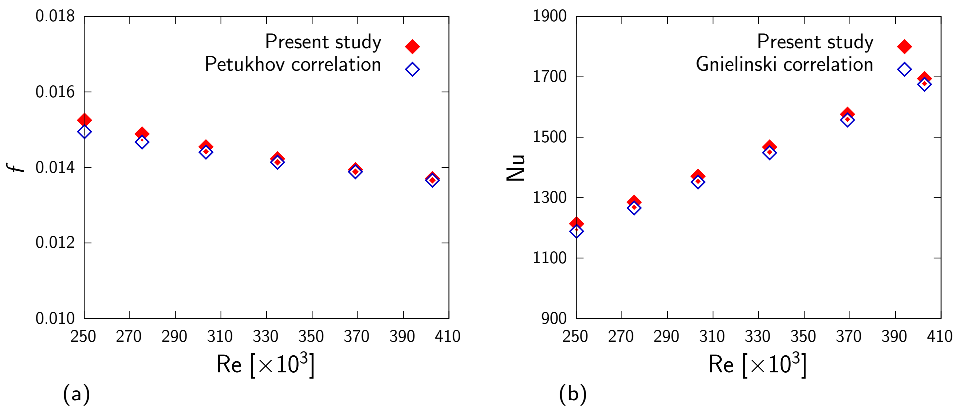

FIGURE 6.4: Validation of CFD numerical results compared to correlation results : (a) friction factor, and (b) Nusselt number.

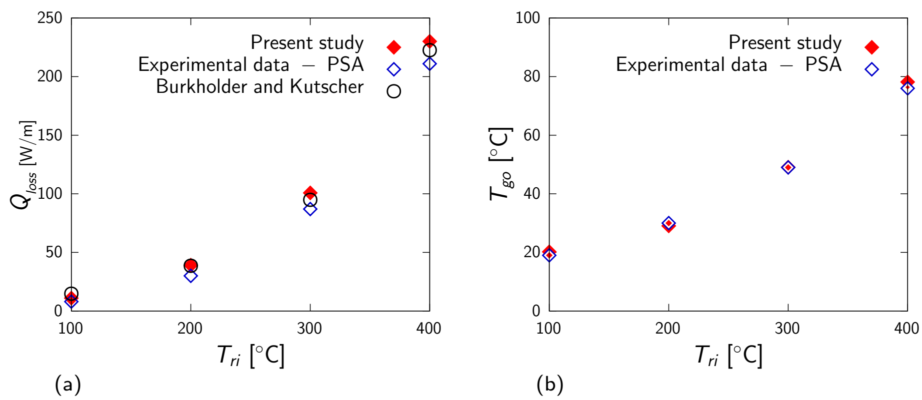

FIGURE 6.5: Validation of CFD numerical results compared to experimental data under vacuum condition: (a) heat loss, and (b) glass cover temperature.

Plataforma Solar de Almería (PSA) [121] and the Forristall EES model [80] were used for comparison. Figure 6.6 shows the variation of heat loss (Q_{loss}) and glass cover temperature (T_{go}) with receiver inner wall temperature under hydrogen conditions. The mean deviation for heat loss was 11.2% with respect to the PSA data and 9.7% with respect to the Forristall model.

For the glass temperature, the mean deviation was 15.5% with respect to the PSA data and 6.7 % with respect to the Forristall model. These results confirm that the developed CFD model provides a reliable prediction of the receiver's thermal performance even under non-vacuum (hydrogen) conditions.

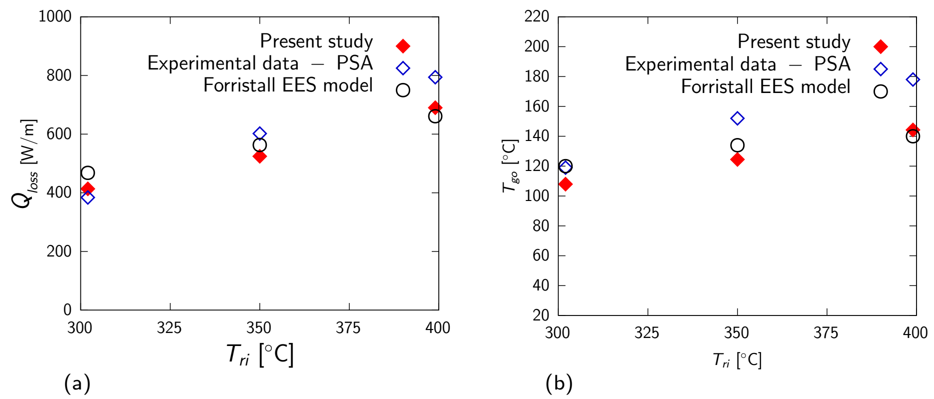

FIGURE 6.6: Validation of CFD numerical results compared to experimental data under hydrogen condition: (a) heat loss, and (b) glass cover temperature.

It is worth noting that the slightly higher deviation observed for the hydrogen-filled annulus compared to the vacuum case can be attributed to the complex and dynamic behavior of hydrogen within the annulus. Unlike vacuum conditions, where heat transfer is dominated by radiation, the presence of hydrogen introduces additional convective and conductive heat transfer mechanisms that are highly sensitive to local pressure, temperature, and gas composition. Furthermore, unsteady hydrogen flow within the glass envelope may occur due to the gradual release or re-absorption of hydrogen by the getter materials, which are affected by the instantaneous getter temperature and hydrogen pressure. These factors make it more challenging to reach a steady-state condition experimentally, contributing to the observed discrepancies. Despite these complexities, the CFD model successfully reproduces the overall heat-loss trends, demonstrating good predictive capability under hydrogen-filled operating conditions.

6.3 Results and discussion

The numerical results are presented and discussed below. First, the HTF, absorber, and glass cover temperatures, velocity contours, and velocity vectors are shown under the defined operating conditions. Next, the temperature profiles of the absorber and glass tubes are presented. Finally, the heat losses for both conditions of the receiver tube — vacuum and hydrogen in the annulus — are discussed.

6.3.1 Temperature, velocity contours, and velocity vectors

Figure 6.7 presents detailed temperature contours at the outlet cross-section of the receiver for mass flow rates of 3 and 6 kg/s under two different annulus conditions: (a) vacuum and (b) hydrogen-filled. The contours illustrate both the temperature distribution inside the absorber tube and the corresponding thermal response of the glass envelope, each displayed with its own temperature scale. These temperature ranges provide important insight into the thermal behavior of the receiver and the degree of heat loss occurring through the annulus.

In a vacuum (Figure 6.7a), the glass envelope remains relatively cold, with temperatures ranging from around 342.1 K to 349.5 K. This small temperature range indicates that minimal heat is transferred from the absorber tube to the glass surface. This is what we would expect when the annular gap is evacuated, as this cuts off conductive and convective heat transfer mechanisms. The temperature of the glass along the edge changes only slightly. The lower part of the glass envelope is somewhat warmer because it radiates heat to the hotter absorber surface below. The absorber tube, on the other hand, remains much hotter, with temperatures reaching over 690 K depending on the mass flow rate. These high absorber temperatures demonstrate the effectiveness of the receiver when a proper vacuum is maintained.

On the other hand, the temperature profile of the hydrogen-filled annulus (Figure 6.7b) is very different. The temperature of the glass envelope is now between 411.2 K and 423.1 K, a significant increase compared to the vacuum scenario. This is due to the greater thermal conductivity of hydrogen and conductive and convective heat transmission across the annulus. Consequently, more heat flux reaches the glass envelope, causing

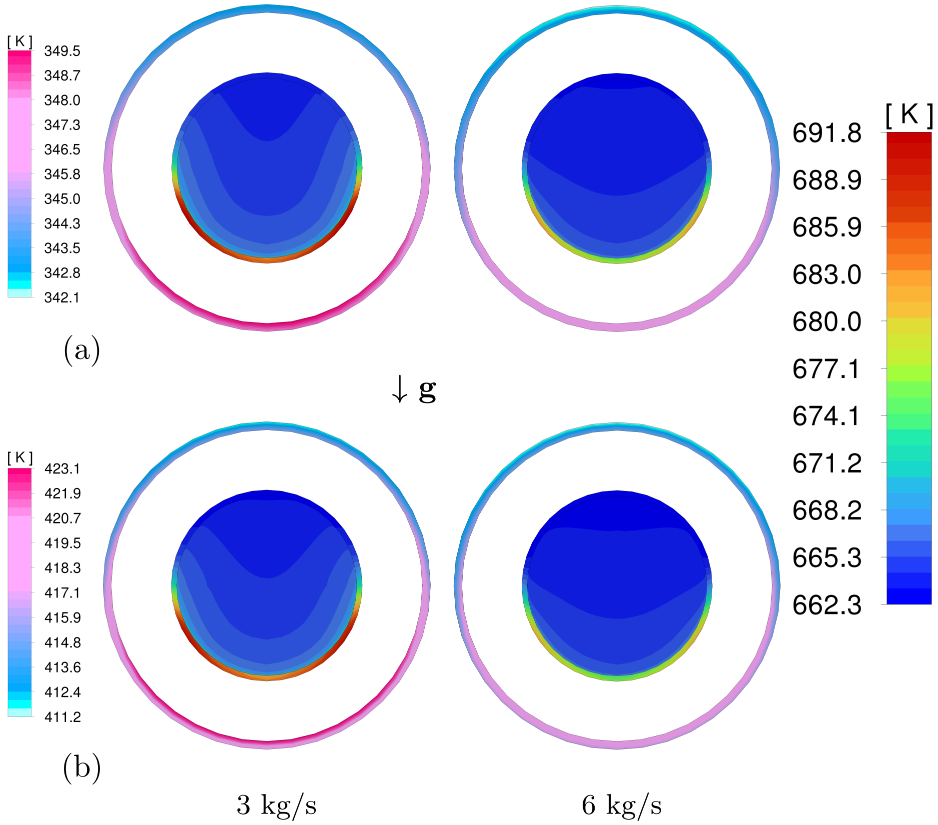

FIGURE 6.7: Temperature contours at the outlet of the absorber tube for T_{in} = 390 °C and DNI = 850 W/m^2: (a) vacuum in the annulus; (b) hydrogen in the annulus.

it to become extremely warm. The temperature range of the glass is also wider than in the vacuum scenario. This means that the circumferential gradients are stronger, as the hydrogen-filled annulus moves due to buoyancy. This behaviour demonstrates that the annulus is less effective at insulating, resulting in the receiver losing more heat.

The influence of mass flow rate is present in both annulus conditions but is less dominant than the effect of the annular medium itself. At a mass flow rate of 3 kg/s, the absorber tube temperature is higher, which enhances radiative exchange with the glass envelope. Increasing the flow rate to

6 kg/s cools the absorber tube by improving convective heat transfer to the HTF, thereby slightly reducing the glass-envelope temperature within each respective temperature scale. Nevertheless, the magnitude of this change is small compared to the temperature rise caused by hydrogen infiltration. Even at the higher mass flow rate, the glass temperature in the hydrogen case remains significantly above that of the vacuum case.

Overall, the temperature ranges shown in Figure 6.7 make it clear that the thermal performance of the receiver is greatly affected by the conditions of the annulus gas. In the vacuum case, radiative heat loss is probably the most important mechanism of heat transfer because the glass temperatures are low (342–349 K). This enables the absorber to maintain higher temperatures, thereby improving the system's performance. Conversely, the substantially higher glass temperatures (411–423 K) in the hydrogen-filled annulus indicate degraded insulation quality, resulting in increased heat losses and lower absorber temperatures. These findings emphasise the importance of maintaining vacuum integrity to optimise receiver efficiency, minimise thermal losses and reduce unnecessary thermal loading on the glass envelope.

The velocity contours at the outlet of the absorber tube for T_{in} = 390 °C and DNI = 850 W/m^2 are shown in Figure 6.8, for mass flow rates of 3, 4, 5, and 6 kg/s. Only the results for hydrogen in the annulus are presented, as internal fluid flow in the absorber tube (represented by the velocity contours) is almost identical for both the vacuum and hydrogen annulus conditions.

This chapter analysed only one position of the receiver tube, with the concentrated heat flux impinging on the receiver from below (the parabola facing the zenith). The direction of gravity is also indicated in the figures. In addition to forced convection, natural convection arises due to the temperature-dependent properties of the HTF. At lower mass flow rates, the fluid velocity is reduced, and the maximum velocity (indicated by a white cross symbol) is observed away from the center of the tube, as shown in Figure 6.8. This behavior is attributed to the combined influence of natural convection effects and weaker turbulent forces on the velocity profile. As the mass flow rate increases, turbulent forces become more dominant, causing the location of the maximum velocity to shift towards the center of the tube.

Figure 6.9 shows the velocity vectors of hydrogen in the closed annulus

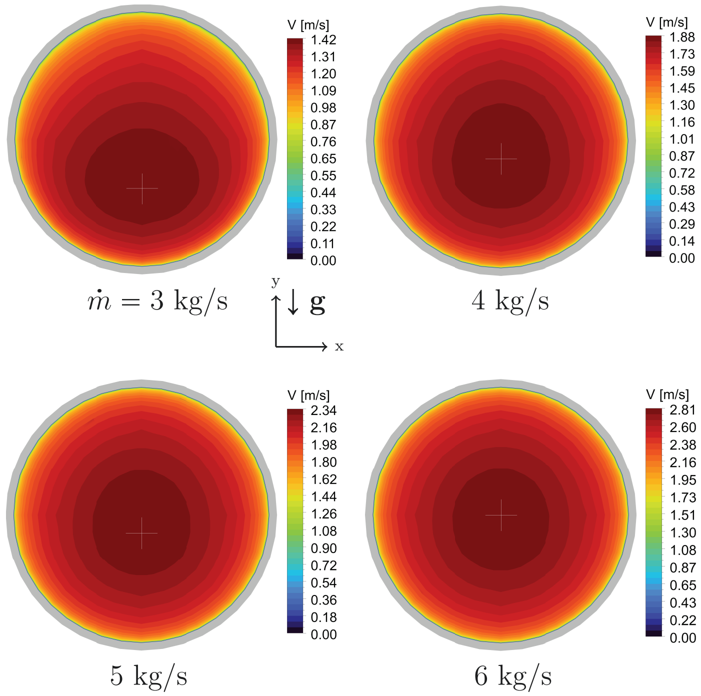

FIGURE 6.8: Velocity contours at the outlet of the absorber tube for T_{in} = 390 °C and DNI = 850 W/m^2.

between the outer surface of the absorber tube and the inner surface of the glass envelope, at both lower and higher inlet temperatures of the HTF, for $\dot{m}$ = 3 kg/s and DNI = 850 W/m^2 in the x-y plane. The flow pattern in the annular space appears mostly symmetric, with one vortex rotating counterclockwise on the left and another rotating clockwise on the right. This buoyancy-driven flow occurs because the outer surface of the absorber tube is hot while the inner surface of the glass envelope is cold. As a result, hydrogen rises along the hot outer surface and descends along the cold inner surface. As expected, the natural convection is more intense for the higher HTF inlet temperature T_{in}.

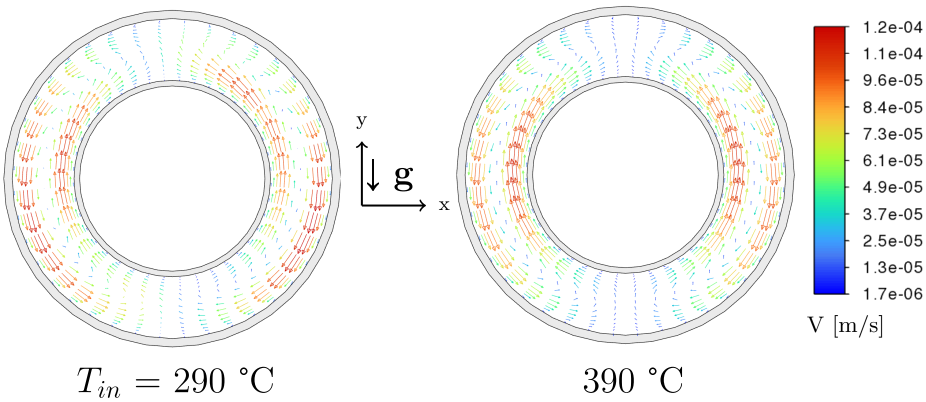

FIGURE 6.9: Velocity vectors in the annulus space filled with hydrogen at a pressure of 1 mbar (cross-section at the end of the receiver tube), with $\dot{m}$ = 3 kg/s and DNI = 850 W/m^2.

6.3.2 Temperature profile of absorber and glass envelope outer surfaces

Figure 6.10 presents the circumferential temperature distribution on the right half of the absorber surface ($180^\circ \leq \theta \leq 360^\circ$) and the corresponding outer surface of the glass tube at T_{in} = 390 °C and DNI = 850 W/m², for annulus conditions of vacuum (10^{-2} mbar) and hydrogen (1 mbar) at z = 3.86 m, i.e. a cross-section close to the receiver outlet. Under vacuum, the absorber surface maintains slightly higher temperatures due to negligible convective heat losses, while the presence of hydrogen slightly reduces the surface temperature due to higher conductive and convective heat transfer. On the glass tube side, hydrogen raises the outer surface temperature to approximately 142 °C, compared to 74°C under vacuum, as a result of increased heat transfer via conduction and convection. This increase in the glass envelope temperature in the presence of hydrogen not only increases heat loss but may also induce high stresses in the glass-to-metal seals of the receiver tube, which could ultimately lead to receiver failure. The average outer surface temperatures of the absorber and glass tubes at varying inlet HTF temperatures and mass flow rates, for both vacuum and hydrogen annulus conditions, are presented in Table 6.2.

TABLE 6.2: Average temperature of outer surface of receiver T_{ro} and glass cover T_{go}.

$\dot{m}$ (kg/s)	T_{in} (°C)	Vacuum		Hydrogen		Vacuum		Hydrogen	
		850 (W/m^2)	1000 (W/m^2)	850 (W/m^2)	1000 (W/m^2)	850 (W/m^2)	1000 (W/m^2)	850 (W/m^2)	1000 (W/m^2)
		$T_{ro,avg}$ (°C)		$T_{ro,avg}$ (°C)		$T_{go,avg}$ (°C)		$T_{go,avg}$ (°C)	
3	290	304.3	306.7	303.0	305.5	47.2	47.7	106.4	107.2
	310	324.0	326.3	322.6	325.1	51.3	51.8	113.1	113.9
	330	343.6	345.9	342.2	344.6	55.8	56.4	119.9	120.8
	350	363.3	365.5	361.8	364.1	60.7	61.4	127.0	127.8
	370	382.9	385.1	381.4	383.7	66.1	66.8	134.2	135.1
	390	402.7	404.8	401.1	403.3	72.1	72.8	141.7	142.5
4	290	301.8	303.7	300.7	302.8	46.7	47.1	105.6	106.3
	310	321.5	323.4	320.4	322.4	50.8	51.2	112.3	113.0
	330	341.2	343.1	340.0	342.0	55.2	55.7	119.1	119.9
	350	360.9	362.7	359.7	361.6	60.1	60.6	126.2	126.9
	370	380.6	382.4	379.4	381.3	65.5	66.0	133.4	134.1
	390	400.4	402.1	399.1	400.9	71.4	72.0	140.9	141.6
5	290	300.1	301.8	299.2	301.0	46.4	46.7	105.1	105.7
	310	319.9	321.5	318.9	320.6	50.4	50.8	111.8	112.4
	330	339.6	341.2	338.6	340.3	54.8	55.3	118.6	119.2
	350	359.4	360.9	358.3	360.0	59.7	60.2	125.7	126.3
	370	379.1	380.6	378.0	379.6	65.1	65.5	132.9	133.5
	390	398.9	400.4	397.7	399.4	70.9	71.4	140.4	141.0
6	290	299.0	300.4	298.1	299.7	46.1	46.5	104.7	105.3
	310	318.7	320.1	317.8	319.4	50.2	50.5	111.4	111.9
	330	338.5	339.9	337.6	339.1	54.6	55.0	118.3	118.8
	350	358.3	359.6	357.3	358.8	59.4	59.8	125.3	125.8
	370	378.0	379.3	377.0	378.5	64.8	65.2	132.5	133.1
	390	397.9	399.1	396.8	398.2	70.6	71.1	140.0	140.6

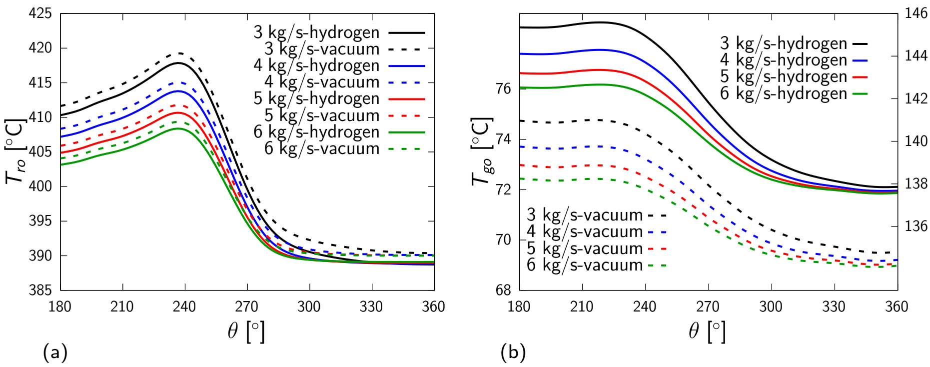

FIGURE 6.10: Temperature profiles on the outer surfaces of the absorber tube (a) and glass envelope (b) at T_{in} = 390°C and DNI = 850 W/m^2.

6.3.3 Maximum circumferential temperature difference on the absorber tube surface (ΔT_{max})

Due to the non-uniform heat flux distribution on the absorber tube, circumferential temperature variations occur along the absorber's periphery. Under normal operating conditions, the maximum allowable temperature difference across the cross-section of the tube should not exceed 50 °C approximately [33].

A low mass flow rate of HTF significantly increases the circumferential temperature difference, leading to potential absorber tube deflection or other failures. Therefore, controlling circumferential temperature gradients of the absorber tube surface is essential in the design and evaluation of a receiver. Table 6.3 presents the circumferential temperature differences, ΔT_{max}, in a receiver tube under vacuum and hydrogen annulus conditions for various mass flow rates, inlet temperatures, and DNI values (850 and 1000 W/m^2). The results indicate, as expected, that ΔT_{max} decreases with increasing mass flow rate and inlet temperature. For example, at 3 kg/s and T_{in} = 290 °C, the maximum ΔT_{max} reaches 39.4 °C, with vacuum, and 39.1 °C, with hydrogen, at DNI = 1000 W/m^2. However, at 6 kg/s, ΔT_{max} drops to 23.5 °C and 23.3 °C, respectively, highlighting the effectiveness of this higher flow rate in increasing the heat transfer rate in the absorber tube wall and, then, in minimizing thermal gradients. These mass flow rates range, as mentioned before, represent working conditions that are typically

TABLE 6.3: Maximum circumferential temperature differences in the absorber tube.

$\dot{m}$ (kg/s)	T_{in} (°C)	Vacuum 850 (W/m^2) ΔT_{max} (°C)	Vacuum 1000 (W/m^2) ΔT_{max} (°C)	Hydrogen 850 (W/m^2) ΔT_{max} (°C)	Hydrogen 1000 (W/m^2) ΔT_{max} (°C)
3	290	33.7	39.4	33.4	39.1
	310	33.0	38.6	32.8	38.3
	330	32.3	37.8	32.1	37.5
	350	31.7	37.0	31.5	36.8
	370	31.1	36.3	31.0	36.2
	390	30.7	35.9	30.6	35.7
4	290	28.6	33.5	28.3	33.2
	310	27.9	32.8	27.7	32.5
	330	27.3	32.1	27.2	31.9
	350	26.8	31.4	26.6	31.2
	370	26.3	30.8	26.1	30.7
	390	25.9	30.4	25.7	30.2
5	290	24.9	29.2	24.7	29.0
	310	24.3	28.6	24.1	28.3
	330	23.8	27.9	23.6	27.7
	350	23.3	27.3	23.1	27.1
	370	22.8	26.8	22.6	26.6
	390	22.4	26.4	22.3	26.2
6	290	22.2	26.0	22.0	25.8
	310	21.6	25.5	21.5	25.3
	330	21.2	24.9	21.0	24.7
	350	20.7	24.4	20.6	24.2
	370	20.3	23.9	20.2	23.7
	390	20.0	23.5	19.8	23.3

set in the operation of solar power plants with PTCs and thermal oil as HTF.

The convective heat transfer coefficient, h_{coef}, at the inner wall of the absorber tube, as shown in Table 6.4, shows a clear increasing trend with both mass flow rate and inlet temperature across all tested conditions. At a constant direct normal irradiance (DNI), increasing the flow rate from 3 to 6 kg/s results in a significant rise in h_{coef}. For instance, at T_{in} = 290 °C and DNI = 850 W/(m$^2 \cdot$ K), h_{coef} increases from 1848.3 to 3206.2 W/(m$^2 \cdot$ K).

TABLE 6.4: Convective heat transfer coefficient (h_{coef}).

$\dot{m}$ (kg/s)	T_{in} (°C)	Vacuum		Hydrogen	
		850 (W/m^2)	1000 (W/m^2)	850 (W/m^2)	1000 (W/m^2)
		h_{coef} (W/m^{2}K)	h_{coef} (W/m^{2}K)	h_{coef} (W/m^{2}K)	h_{coef} (W/m^{2}K)
3	290	1848.3	1856.8	1847.6	1856.3
	310	1888.4	1897.1	1887.7	1896.6
	330	1928.8	1937.8	1928.1	1937.2
	350	1969.2	1978.1	1968.4	1977.6
	370	2006.0	2014.6	2005.2	2014.1
	390	2030.9	2038.4	2030.0	2037.9
4	290	2299.8	2304.5	2299.2	2304.0
	310	2354.3	2358.9	2353.7	2358.3
	330	2408.9	2413.5	2408.3	2412.9
	350	2463.5	2468.0	2462.8	2467.3
	370	2514.0	2517.9	2513.3	2517.1
	390	2550.3	2552.7	2549.4	2551.9
5	290	2755.1	2758.1	2754.8	2757.8
	310	2824.1	2826.9	2823.7	2826.5
	330	2893.0	2895.6	2892.6	2895.2
	350	2961.8	2964.1	2961.4	2963.7
	370	3025.9	3027.4	3025.4	3027.0
	390	3073.4	3073.4	3072.9	3073.0
6	290	3206.2	3208.6	3206.1	3208.4
	310	3289.2	3291.2	3289.0	3291.1
	330	3371.8	3373.6	3371.6	3373.4
	350	3454.2	3455.7	3454.1	3455.5
	370	3531.4	3532.1	3531.2	3531.9
	390	3589.7	3588.9	3589.5	3588.7

Similarly, at a fixed flow rate (e.g., 5 kg/s), raising the inlet temperature from 290 °C to 390 °C increases h_{coef} from 2755.1 to 3073.4 $\mathrm{W/(m^2 \cdot K)}$. This enhancement is attributed to improved convective heat transfer resulting from higher Reynolds numbers and reduced viscosity of Therminol® VP-1 at elevated temperatures. Additionally, the difference in h_{coef} between vacuum (10^{-2} mbar) and hydrogen (1 mbar) annulus conditions remains negligible (typically < 1 $\mathrm{W/(m^2 \cdot K)}$) across all scenarios, indicating that internal convection dominates heat transfer within the absorber tube.

6.3.4 Heat losses

A significant difference in thermal behavior is observed between vacuum and hydrogen annulus conditions, primarily due to the presence (hydrogen) or absence (vacuum) of convective heat transfer in the annulus space between the absorber tube and the glass envelope. Heat losses for both cases, provided in Table 6.5 together with the ratio H_2/Vac between hydrogen and vacuum conditions results, highlight this distinction.

Under vacuum annulus condition, heat losses are significantly lower due elimination of convection, leaving radiation as the dominant loss mechanism. In contrast, introducing hydrogen at 1 mbar enables convective heat transfer, substantially increasing total heat losses. For example, at a mass flow rate of 3 kg/s, an inlet temperature of T_{in} = 390 °C, and DNI = 1000 W/m^2, total heat loss rises from 230.9 W/m (vacuum) to 723.2 W/m (hydrogen), highlighting the critical need to maintain high-vacuum conditions.

Heat losses also increase with inlet temperature across all cases due to higher absorber surface temperatures. Under vacuum, radiation dominates, as evidenced by the rise in Q_{loss} from 100.3 W/m at 290 °C to 226.7 W/m at 390 °C (DNI = 850 W/m^2, $\dot{m}$ = 3 kg/s). Conversely, increasing the mass flow rate slightly reduces heat loss by moderating absorber temperatures. For instance, Q_{loss} decreases from 226.7 W/m at 3 kg/s to 218.2 W/m at 6 kg/s under identical conditions.

Under vacuum, radiation accounts for nearly all heat loss, as confirmed by the near equivalence of total and radiative losses. With hydrogen in the annulus space, however, convection contributes more prominently, slightly reducing radiation's relative share.

6.3.5 Influence of Wind Speed and Operational Envelope

To capture the combined influence of solar input, operating temperature, and flow rate, two representative extreme conditions were further analyzed, considering the effect of the wind speed:

- a low DNI, lower inlet temperature, and higher mass flow rate case (DNI $= 850$ W/m^2, $T_{in} = 290$ °C, $\dot{m} = 6$ kg/s), and
- a high DNI, higher inlet temperature, and lower mass flow rate case (DNI $= 1000$ W/m^2, $T_{in} = 390$ °C, $\dot{m} = 3$ kg/s).

TABLE 6.5: Total heat loss (Q_{loss}) and radiation heat loss (Q_{rad}).

$\dot{m}$ (kg/s)	T_{in} (°C)	Vacuum Q_{loss} (W/m)		Hydrogen Q_{loss} (W/m)		Vacuum Q_{rad} (W/m)		Hydrogen Q_{rad} (W/m)	
		850 (W/m^2)	1000 (W/m^2)	850 (W/m^2)	1000 (W/m^2)	850 (W/m^2)	1000 (W/m^2)	850 (W/m^2)	1000 (W/m^2)
3	290	100.3	102.7	442.6	449.7	100.3	102.6	88.5	90.9
	310	119.2	121.8	489.9	497.4	119.1	121.7	105.7	108.4
	330	140.8	143.8	540.4	548.3	140.7	143.7	125.5	128.6
	350	165.7	169.0	594.3	602.6	165.5	168.8	148.3	151.8
	370	194.2	197.9	651.9	660.7	193.9	197.6	174.5	178.4
	390	226.7	230.9	713.8	723.2	226.4	230.6	204.5	208.9
4	290	98.0	99.9	437.1	443.2	98.0	99.9	86.6	88.6
	310	116.6	118.7	484.2	490.6	116.5	118.6	103.5	105.8
	330	137.9	140.4	534.5	541.2	137.8	140.2	123.1	125.6
	350	162.5	165.2	588.2	595.3	162.2	165.0	145.6	148.5
	370	190.5	193.6	645.6	653.1	190.3	193.3	171.5	174.7
	390	222.7	226.1	707.2	715.2	222.3	225.7	201.2	204.8
5	290	96.5	98.1	433.5	438.8	96.5	98.1	85.3	87.0
	310	114.9	116.7	480.5	486.1	114.8	116.6	102.1	104.0
	330	136.0	138.1	530.6	536.5	135.9	137.9	121.5	123.7
	350	160.3	162.6	584.1	590.4	160.1	162.4	143.8	146.3
	370	188.2	190.8	641.4	648.0	187.9	190.5	169.5	172.3
	390	220.1	222.9	702.8	709.9	219.7	222.6	199.0	202.1
6	290	95.4	96.9	430.9	435.7	95.4	96.8	84.4	85.9
	310	113.7	115.3	477.8	482.9	113.6	115.2	101.1	102.8
	330	134.7	136.5	527.9	533.2	134.5	136.3	120.4	122.3
	350	158.9	160.9	581.3	587.0	158.6	160.6	142.6	144.8
	370	186.6	188.8	638.5	644.5	186.2	188.5	168.1	170.6
	390	218.2	220.8	699.8	706.2	217.8	220.3	197.5	200.3

These two points effectively bound the practical operational envelope of the parabolic-trough receiver and enable evaluation of wind effects under both mild and severe thermal loading conditions.
The wind-sensitivity analysis was performed for wind speeds of 0, 5, and 10 $\mathrm{m\,s^{-1}}$ under both vacuum and hydrogen annulus conditions. The external convective coefficient was modified according to Eq. (3.11), and total losses were recalculated for extreme operating conditions. The results, summarized in Table 5, show that increasing wind speed slightly increases the total heat loss but markedly reduces the glass temperature. This behaviour is more pronounced for hydrogen, where convective coupling in the annular gap is stronger. For example, under hydrogen at $DNI = 1000\,\mathrm{W/m^2}$, $T_{go,\mathrm{avg}}$ decreases from 142.5 °C (no wind) to 70.7 °C (wind speed equal to 10 $\mathrm{m\,s^{-1}}$), while the total linear loss rises from 723 to 851 W/m, which corresponds to an increase of 18%. In contrast, for the vacuum cases, the increase in thermal loss between the no-wind and 10 m/s wind scenarios was less than 4%. Although the increase in Q_{loss} represents a minor efficiency penalty, the significant reduction in T_{go} is beneficial for receiver durability and thermal safety. From this perspective, the assumption of no wind in this work can be considered as conservative.

TABLE 6.6: (Q_{loss}) and ($T_{go,avg}$) under different wind speeds, DNI, and flow rates.

DNI ($\mathrm{W/m^2}$)	u_w (m/s)	T_{in} (°C)	$\dot{m}$ (kg/s)	$T_{go,avg}$ (°C) Vacuum	$T_{go,avg}$ (°C) Hydrogen	Q_{loss} (W/m) Vacuum	Q_{loss} (W/m) Hydrogen
850	0	290	6	46.1	104.7	95.4	430.9
	5			31.6	62.5	98.6	500.3
	10			29.7	52.7	98.9	515.5
1000	0	390	3	72.8	142.5	230.9	723.2
	5			42.5	86.2	237.1	824.6
	10			37.4	70.7	237.8	850.5

6.4 Conclusions

The study described in this chapter presents a comprehensive numerical investigation of the heat transfer and thermal behavior in parabolic trough receivers under realistic operating conditions. The analysis compares vacuum and low-pressure hydrogen environments in the annulus space between the absorber and glass envelope of the receivers. Parametric analysis across mass flow rates (3-6 kg/s), inlet fluid temperatures (290-390 °C), and DNI levels (850-1000 W/m^2) demonstrates the system's sensitivity to these variables. Increasing the mass flow rate from 3 kg/s to 6 kg/s reduces the maximum circumferential temperature difference of the absorber surface (ΔT_{max}) by 40.4%, from 39.4 °C to 23.5 °C (at T_{in} = 290 °C and DNI = 1000 W/m^2). Similarly, higher inlet temperatures enhance absorber's temperature distribution uniformity, further lowering ΔT_{max}.

Temperature contours and velocity profiles reveal that higher mass flow rates lower receiver temperatures and centralize flow patterns due to dominant turbulent forces. Additionally, hydrogen in the annulus slightly lowers absorber surface temperatures while increasing glass envelope temperatures by up to 142 °C through convective and conductive heat transfer.

Heat loss analysis shows hydrogen in the annulus increases thermal losses by 3 times compared to vacuum conditions. For instance, at $\dot{m}$ = 3 kg/s and T_{in} = 390 °C, heat loss rises from 230.9 W/m (vacuum) to 723.2 W/m (hydrogen). These results emphasize the necessity of maintaining high-vacuum conditions to minimize energy dissipation.

Wind-speed analysis further revealed that external flow effects slightly increased total heat losses (up to 18%) while substantially lowering glass envelope temperatures, particularly under hydrogen conditions.

The numerical insights derived in this work enable two practical applications: (a) optimization of mass flow rates and temperature thresholds in commercial PTC plants; and (b) accurate prediction of thermal performance variations in solar fields using thermal oils, particularly during hydrogen permeation events.

Chapter 7

Additional Work: Numerical Modelling of Solar Thermochemical Heat Storage

The global shift toward sustainable energy necessitates the increased utilization of renewable energy sources, such as solar power, to mitigate climate change and stabilize energy supply. However, the intrinsic characteristics of solar energy, including its intermittent and fluctuating nature, pose major technical and economic obstacles to its widespread commercial use. The rapid global adoption of solar thermal plants has increased the need for large-scale, effective thermal energy storage (TES) systems.

This chapter details the additional research conducted during a three-month mobility visit, focusing on the numerical modeling of the CaO and $Ca(OH)_2$ thermochemical energy storage (TCES) system using ANSYS Fluent. Although the primary focus of this PhD work is the thermal performance and optimisation of parabolic trough receivers, thermal energy storage is an equally essential component of modern CSP systems. Efficient storage enables continuous operation, smooths solar intermittency, and significantly enhances the overall performance and dispatchability of PTC plants. For this reason, the study of a reactor-scale TCES system provides an important complementary contribution to the broader objectives of the thesis. The goal of the present work was to develop, implement, and assess a high-fidelity CFD framework capable of simulating the coupled processes of heat transfer, mass transport, and reaction kinetics associated with hydration and dehydration in a reactive packed-bed reactor. User-defined functions (UDFs) were created to integrate experimentally validated kinetic expressions, including the two-regime dehydration behaviour described by Schaube *et al.* [122, 123], directly into the ANSYS Fluent environment. The model predictions were compared with benchmark experimental data and showed strong agreement in terms of temperature rise, reaction progression, and distinctive features such as hotspot formation and cooling fronts. The validated CFD–UDF framework establishes a solid basis for future work on the integration of TCES units into PTC systems.

7.1 Introduction

Thermal storage is essential for ensuring dispatchability and extending energy output beyond daylight hours in CST/CSP plants, like those with parabolic trough collector systems. Despite having reached commercial maturity, traditional thermal energy storage techniques, such as molten salt sensible heat storage, have intrinsic drawbacks, including relatively low energy density, long-term heat losses, and upper working temperature restrictions imposed by fluid stability. Thermochemical energy storage (TCES) is a class of technologies that uses reversible chemical reactions to store heat in chemical bonds. TCES has gained attention as global energy systems strive for greater efficiency and deeper integration of renewable sources.

The $CaO/Ca(OH)_2$ combination is one of the most promising TCES possibilities for mid-temperature storage relevant to parabolic trough applications. This reversible reaction:

$$Ca(OH)_2\,(s) \rightleftharpoons CaO\,(s) + H_2O\,(g)$$

has a favorable equilibrium curve in the 400–550°C region and a high reaction enthalpy of around 100–110 kJ/mol. It also has remarkable material advantages, such as abundance, non-toxicity, and affordability. Solar heat breaks down calcium hydroxide into calcium oxide and steam during dehydration (charging phase; heat is absorbed in the endothermic reaction), and the steam and calcium oxide then react to produce heat at regulated temperatures during hydration (discharging phase: heat is released in the exothermic reaction). The reaction's intrinsic temperature buffering makes stable outlet temperatures possible during discharging, which is highly sought after for thermal power blocks and parabolic trough power cycles.

7.1.1 Historical development and early CSP integration

In earlier work, Ervin [124] conducted a comprehensive study on TCES: a thorough analysis of reversible oxide-hydroxide reactions, such as the $CaO/Ca(OH)_2$ cycle, as a potential source of large-scale solar heat storage. In this work, the basic benefits that continue to drive current research were delineated: (i) high theoretical energy density, (ii) loss-free long-term storage at room temperature, (iii) capacity to transport charged and discharged reactants, and (iv) suitability for high temperatures necessary for effective power cycles. This work emphasized two important points. First, $CaO/Ca(OH)_2$ exhibits favorable thermodynamics. Second, it has a comparatively benign materials profile relative to other thermochemical candidates. These characteristics make it especially attractive for solar heat storage applications. Although the study primarily focused on general material behavior and early experimental programs, it identified $CaO/Ca(OH)_2$ as a promising option for solar-driven storage systems decades before they matured.

Over a decade later, a significant milestone was reached when Brown *et al.* [125] conducted the first comprehensive analysis of integrating $CaO/Ca(OH)_2$ storage with a commercial parabolic trough plant, specifically the SEGS facility in California. Their theoretical model demonstrated that the $CaO/Ca(OH)_2$ cycle could transfer thermal energy from day to night by performing the dehydration reaction during peak sunlight hours and producing steam through hydration when sunlight was unavailable. This system could sustain stable temperatures for the Rankine cycle boiler and reduce the need for fossil fuel backup. This work is widely considered the first rigorous techno-economic study of $CaO/Ca(OH)_2$ storage in a real CSP context. This study was based directly on the thermochemical ideas put forward in earlier foundational work, such as that of [124].

TCES research reached a key turning point thanks to precise kinetic and thermodynamic characterization and controlled trials at the reactor scale. Schaube *et al.* [126] studied high-temperature gas-solid interactions for CSP and said that $CaO/Ca(OH)_2$ was one of the best storage combinations because of its high energy density and good thermodynamic operating window. Their further kinetic investigation yielded commonly utilized equilibrium expressions, reaction enthalpies, and two-regime dehydration kinetics — characterized by chemical control at low conversion, succeeded by diffusion limitation as a CaO product layer develops. These kinetic principles became the usual input for reactor-scale simulations and, more crucially, the basis for the UDF formulas used in modern CFD models.

To assess these kinetics under authentic reactor conditions, Schaube *et al.* [122, 123] conducted a series of direct-contact packed-bed experiments, as shown in the Figure 7.1, achieving finely resolved temperature measurements throughout the bed that identified critical phenomena, including hydration-induced hotspots, dehydration-induced cooling near the inlet, and the advancement of reaction fronts. Their modeling equivalent confirmed reactor-scale simulations with these experiments and showed that accurately modeling steam transport, heat transfer, and surface kinetics was necessary to forecast conversion and temperature profiles. These studies continue to represent the most common approaches for validating new TCES reactor numerical models.

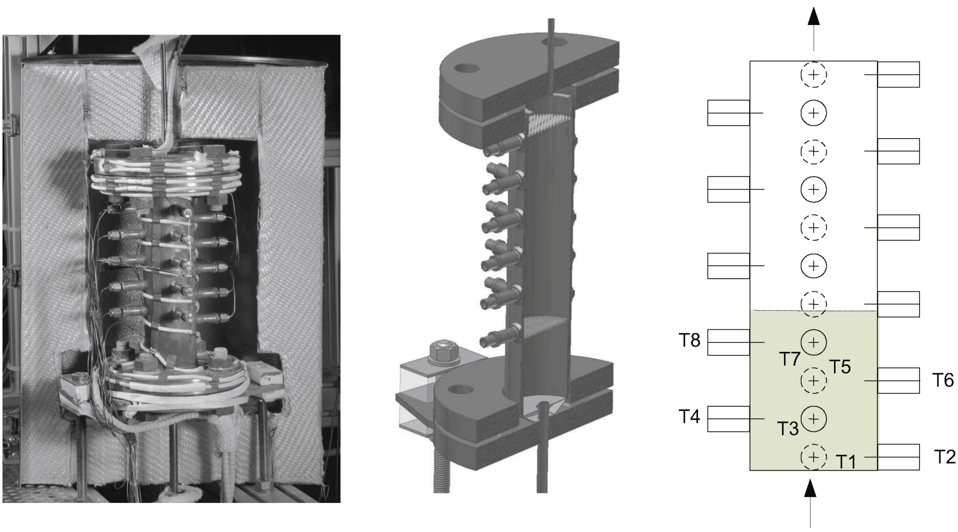

FIGURE 7.1: Reactor with isolation, reactor/reaction chamber, position of thermocouples in the powder bed [122].

As the field progressed, pilot-scale demonstrations validated that the reaction mechanisms identified in laboratory research scaled consistently to kW-level reactors. Linder *et al.* [127] built a kW-scale $CaO/Ca(OH)_2$ reactor and tested the numerical predictions against real data. They showed that the heat penetration, steam distribution problems, and stable multi-cycle operation were all possible under controlled boundary conditions. Around the same time, Yan and Zhao [128] conducted experiments on hydration in fixed beds and measured how strongly reactivity depended on steam partial pressure, initial bed temperature, and material conditioning. They also recorded the impacts of hotspot development and cycle degradation. Further research examined various metal oxide cycles, including Co_3O_4/CoO. Singh *et al.* [129] used computational fluid dynamics (CFD) modelling techniques similar to those now used for calcium-based thermal energy storage systems. This confirmed the effectiveness of multi-physics reactor models for solid–gas thermochemical systems.

Research on the evolution of porosity demonstrated that permeability significantly affects steam transport and that assuming constant porosity can lead to substantial modeling inaccuracies — reaching nearly 20% in certain instances — underscoring the necessity of precise characterization of porous media. Furthermore, sophisticated heat-transfer augmentation methods, such as metal foams and vapor channels, have been demonstrated to increase discharge rates by up to six times. This shows that structural engineering is necessary to overcome the naturally low thermal conductivity of Ca-based materials. Multi-layered reactor designs showed even better temperature uniformity and vapor distribution, which made the reaction move more evenly and higher overall conversion

Reactors were becoming more complex in their design. Luo *et al.* [130] studied fin layouts and showed that the shape, spacing, and surface area of fins had a big effect on thermal spreading and discharge performance. This means that there are clear ways to improve future reactor designs. At a fundamental level, first-principles of reaction kinetics simulations conducted by Cai and Li [131] clarified dehydration mechanisms at the atomic scale and offered mechanistic explanations for empirical kinetic observations, uncovering diffusion barriers and reaction pathways pertinent to enhancing kinetic models employed in reactor simulations.

The latest ideas go beyond only reactor design to include full system integration. Sun *et al.* [132] suggested a dual-reaction TCES cascade that lowers the amount of entropy produced and raises the exergy efficiency, as shown in the Figure 7.2. This opens up new possibilities for how CaO/$Ca(OH)_2$ systems could be built in the future. Yan *et al.* [133] presented a fully integrated CSP–TCES configuration that merges a parabolic trough collector with an advanced thermochemical reactor, as shown in the Figure 7.3. They demonstrated through dynamic simulations that optimizing collector geometry, steam delivery, and reactor thermodynamics can significantly enhance daily conversion and energy output. At the same time, other system-level and techno-economic modeling studies have examined the economic and design trade-offs of TCES integration in CSP plants [134, 135], further supporting the potential of thermochemical energy storage to enhance the performance of next-generation solar thermal power plants.

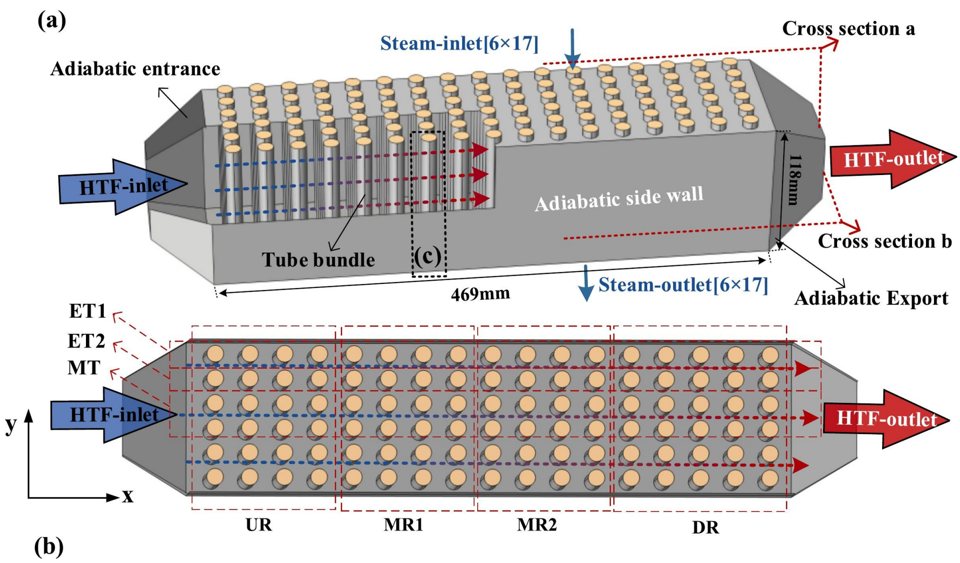

FIGURE 7.2: Structure and exothermic flow of shell-and-tube thermochemical heat storage reactor: (a) 3D structure and (b) top view [132].

The latest research on $CaO/Ca(OH)_2$ thermochemical energy storage shows that accurate prediction of reactor behavior requires models capable of capturing the strong coupling between reaction kinetics, steam transport, porous-media flow resistance, and the highly non-uniform temperature fields that arise during hydration and dehydration. Studies such as [122, 123, 127, 128, 130] consistently demonstrate these interactions. Together, these works show that high-fidelity simulations incorporating validated kinetic laws, multicomponent diffusion, and reaction-enthalpy coupling are essential for reproducing key features in packed-bed reactors, including hydration-induced hotspots, endothermic cooling fronts, and

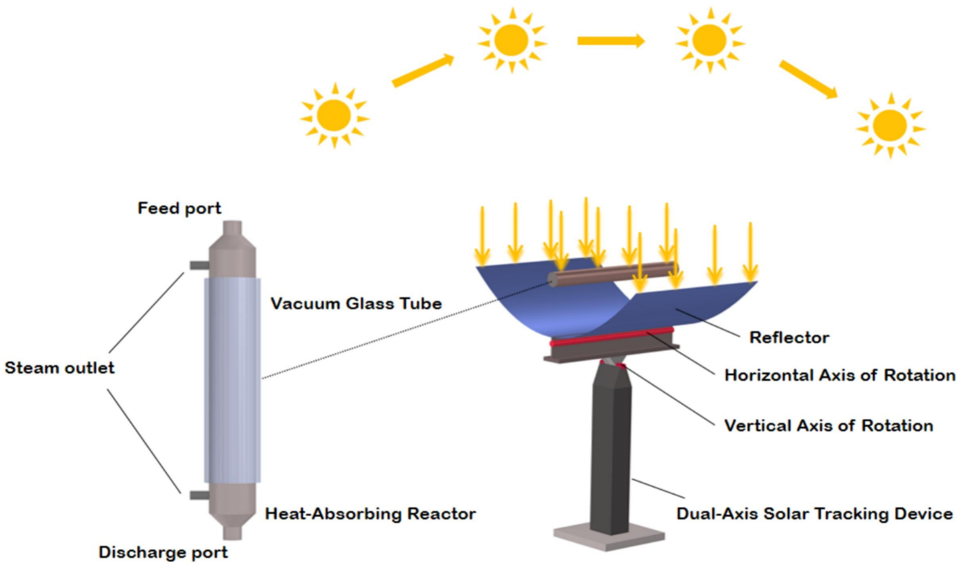

FIGURE 7.3: Schematic diagram of the parabolic trough solar thermal storage system [133].

moving reaction fronts. Based on these requirements, the modeling framework developed in this study incorporates two-regime kinetic expressions [123] into ANSYS Fluent via custom UDFs, allowing local thermochemical rates, species concentrations, and the evolving thermal field to be directly coupled. The CFD–UDF model accurately captures the transient reaction behavior of the reactor when compared with the fixed-bed experiments of [123]. Grounded in experimental data, this approach provides a robust basis for evaluating $CaO/Ca(OH)_2$ storage under CSP-relevant conditions and establishes the necessary link between TCES reactor dynamics and parabolic trough receiver performance within the broader scope of the study.

The next step in this work will be to adapt the validated CFD-UDF modelling method for use in simulating an indirect TCES reactor, which forms part of PTC CSP plants. As previously mentioned, most PTC systems use heat transfer fluids (HTFs), such as synthetic oils or molten salts, to transfer thermal energy to the reactor via an external heat exchanger. This approach contrasts markedly with the direct-exchange fixed-bed configurations commonly examined in laboratory-scale studies. This adds another level of difficulty. In addition to the intrinsic reaction-transport interactions already identified in $CaO/Ca(OH)_2$ systems, the thermal coupling between the HTF loop and the reactive packed bed must be determined. Subsequent research will integrate the simulation framework to include conjugate heat transfer between the HTF channels and the reactive solid domain. This will facilitate the prediction of the effects of HTF temperature, flow rate and heat exchanger geometry on hydration and dehydration rates, thermal front propagation and overall reactor efficiency. Integrating these effects into a single CFD environment will enable the model to evaluate the effectiveness of indirect TCES reactors under real PTC operating conditions and establish a clearer correlation between thermochemical behaviour at the component level and overall plant operation.

In parallel, it will also be important to consider PTC plants that operate in direct steam generation (DSG) mode, as noted by Brown *et al.* [125], where the collector field produces steam directly. A direct TCES reactor is a good option for these systems as it can connect directly to the steam cycle, eliminating the need for an intermediate HTF loop. However, future simulations must consider how these reactors are more susceptible to variations in steam-side pressure, flow distribution and high-pressure operating conditions, as these can significantly impact reaction uniformity and system performance. Incorporating both indirect (HTF-based) and direct (DSG-based) configurations into the modelling process will enable to fully evaluate TCES integration pathways for PTC plants and develop improved reactor designs for the next generation of CSP systems.

The main objectives of this work are

- Develop a numerical model to simulate $Ca(OH)_2$-CaO reaction dynamics using ANSYS Fluent.
- Implement UDFs in ANSYS Fluent for both hydration and dehydration kinetics.
- Validate the simulation results with available experimental data from the literature [122].
- To extend the validated numerical framework toward future application in solar-thermal energy systems, particularly the integration of TCES reactors within the parabolic trough collector system configurations.

7.2 Physical Model

The physical system investigated in this work is a laboratory-scale fixed-bed reactor designed to examine the reversible $CaO/Ca(OH)_2$ thermochemical energy-storage cycle. The reactor is a vertically oriented cylindrical vessel uniformly packed with $Ca(OH)_2$ during dehydration and CaO during hydration. The simulated configuration replicates the geometry and operating conditions reported in the benchmark experiments of Schaube *et al.* [123] and encompasses additional parameters collected during the research mobility period, ensuring full consistency between the CFD domain and the experimental reactor.

The reactor has an internal height of 61 mm and an internal diameter of 55 mm. Owing to the cylindrical symmetry and uniform packing, the reactor is modelled numerically as a two-dimensional axisymmetric domain, as shown in Figure 7.4, which captures all essential radial and axial gradients while reducing computational cost relative to a full 3D model.

The packed bed is treated as a homogeneous porous medium with constant porosity and permeability. The solid phase remains stationary while the gas phase flows through the pore network. A mixture of nitrogen (carrier gas) and water vapour enters at the top of the reactor and exits at the bottom. Two operating modes are simulated:

- **Hydration (discharging):** 3.8 Nl/min N_2 and 120 g/h H_2O at 300 °C (exothermic).
- **Dehydration (charging):** 14.7 Nl/min N_2 and 10 g/h H_2O at 500 °C (endothermic).

In both cases, the outlet pressure is maintained at 2 barg, consistent with the experimental setup. Seven thermocouples positioned along the reactor height provide reference temperature data for validation. Inside the bed, the gas interacts with the solid through the highly exothermic hydration reaction and the strongly endothermic dehydration reaction, leading to moving thermal fronts, hotspots, and cooling regions. These physical features define the behaviour of the $CaO/Ca(OH)_2$ system and form the basis for the mathematical and numerical models that follow.

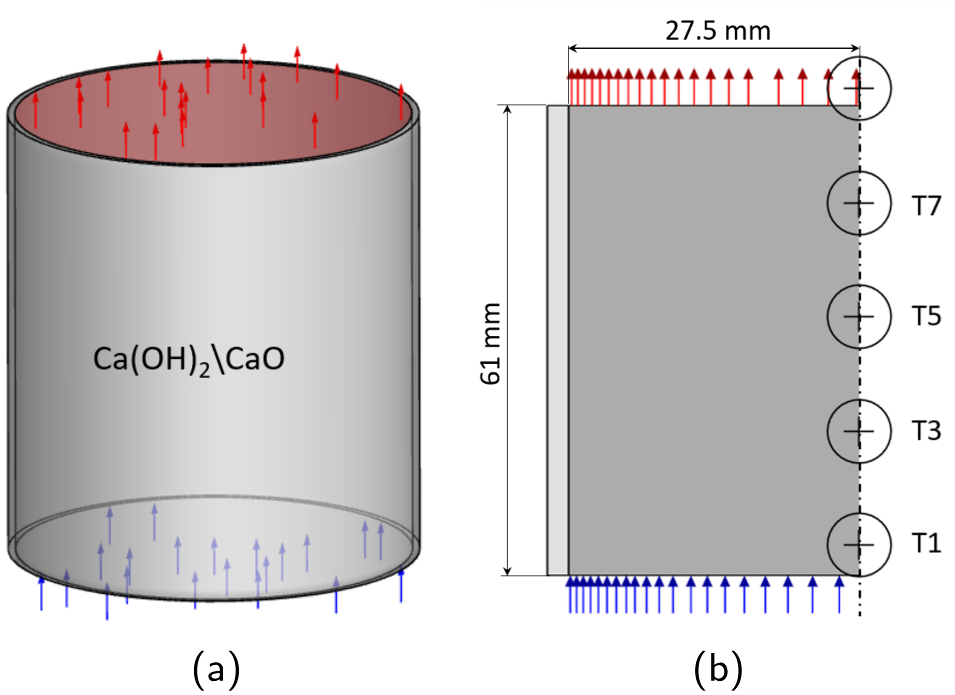

FIGURE 7.4: (a) 3D domain of the reactor; and (b) 2D axisymmetric domain of the reactor.

7.2.1 Numerical Model

The packed-bed reactor was simulated in ANSYS Fluent 2025 R1 using a transient CFD model with chemical reaction implemented via UDFs. The computational domain corresponds to the two-dimensional axisymmetric representation of the cylindrical reactor described in the previous subsection. A structured mesh with fine resolution was generated over the entire computational domain to resolve temperature and species concentration fields adequately; the final grid is shown in Figure 7.5.

The fluid region was defined as a single porous zone with the mixture material (N_2–H_2O–CaO–$Ca(OH)_2$) assigned to the fluid phase and calcium-oxide-solid specified as the solid material in the porous-zone settings. The equilibrium thermal model was used, so that a single energy equation is solved for the combined gas–solid temperature. The porous medium resistance was specified through an effective permeability and a surface-to-volume ratio of $1708.92\,\mathrm{m}^{-1}$, consistent with the particle size and packing conditions of the experimental bed.

The gas phase consisted of a multicomponent mixture of nitrogen (inert carrier gas) and water vapour (reactive species). The species transport model was activated to solve individual conservation equations for H_2O and N_2. Nitrogen was treated as chemically inert, while water vapour participated in the hydration and dehydration reactions. The local steam partial pressure required for the kinetic model was calculated from the local mass fraction of H_2O and the operating pressure.

The reaction kinetics implemented via User-Defined Functions introduced source terms into the governing equations. Specifically, steam consumption or release was applied to the H_2O species equation, while the reaction enthalpy was incorporated as a volumetric heat source term in the energy equation, ensuring full coupling between mass transfer, heat transfer, and chemical reaction.

A pressure-based, transient solver was employed. The governing equations for mass, momentum, energy, and species transport were discretised using a second-order upwind scheme for spatial terms and a first-order implicit scheme for temporal terms. Pressure-velocity coupling was handled using the SIMPLE algorithm. Typical time-step sizes were in the range of 0.01–0.1 s; smaller time steps were adopted during the early stages of the reactions to accurately capture the rapid temperature changes. At each time step, the solution was considered converged when the scaled residuals fell below 10^{-6} for the continuity, momentum, and energy equations, and when monitored temperatures at selected points varied negligibly between subsequent iterations.

The reversible $CaO/Ca(OH)_2$ reaction was activated in the porous zone by enabling the Reaction option and linking the corresponding UDFs.

7.2.2 Governing Equations

The $CaO/Ca(OH)_2$ packed–bed reactor is modeled as a two–dimensional heterogeneous continuum. Gas and solid phases are treated as interpenetrating continua, and mass, momentum, species, and energy equations are solved for each phase. The bed porosity ε is assumed to be constant at 0.6.

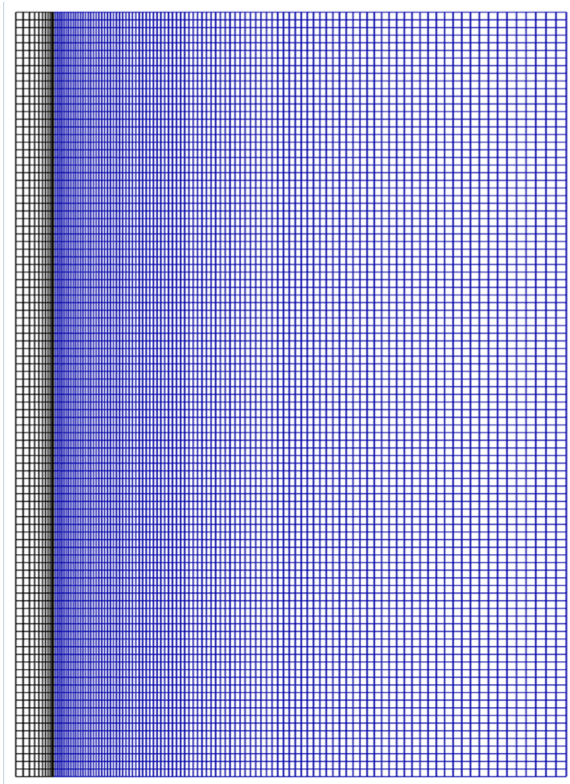

FIGURE 7.5: Meshing of the reactor.

Mass Balances

Solid phase

$$\frac{\partial\left[(1-\varepsilon)\rho_s\right]}{\partial t} = (1-\varepsilon)\, q_R \tag{7.1}$$

where ε is the bed porosity (−), ρ_s is the solid phase density ($\mathrm{kg\,m^{-3}}$), t is time (s), and q_R is the volumetric reaction rate ($\mathrm{kg\,H_2O\,m^{-3}\,s^{-1}}$).

Gas phase

$$\frac{\partial(\varepsilon\rho_g)}{\partial t} + \nabla\cdot(\rho_g\mathbf{v}) = -(1-\varepsilon)\, q_R \tag{7.2}$$

where ρ_g is the gas phase density (kg m^{-3}) and $\mathbf{v}$ is the superficial gas velocity vector (m s^{-1}).

Water vapor species balance

$$\varepsilon\rho_g\frac{\partial Y_{H_2O}}{\partial t}+\rho_g\mathbf{v}\cdot\nabla Y_{H_2O}-\nabla\cdot\left(\rho_g D\nabla Y_{H_2O}\right)=-(1-Y_{H_2O})(1-\varepsilon)\,q_R \quad (7.3)$$

where Y_{H_2O} is the mass fraction of water vapor ($-$) and D is the effective binary diffusion coefficient of H_2O in N_2 (m^2 s^{-1}).

Momentum Balance

Because the Reynolds number in the porous bed is small ($Re_p < 1$), Darcy's law is used:

$$\nabla P=-\frac{\mu_g}{K}\,\mathbf{v} \quad (7.4)$$

where P is the gas pressure (Pa), μ_g is the dynamic viscosity of the gas phase (Pa s), and K is the permeability of the packed bed (m^2).

Energy Balances

Solid phase

$$\begin{aligned}(1-\varepsilon)\rho_s c_{ps}\frac{\partial T_s}{\partial t}&=\alpha^*(T_g-T_s)-\nabla\cdot[-(1-\varepsilon)\lambda_s\nabla T_s]\\&\quad+(1-\varepsilon)q_R\left(\Delta h_R-c_{p,H_2O}(T_s-T_g)\right)\end{aligned} \quad (7.5)$$

where c_{ps} is the specific heat capacity of the solid (J kg^{-1} K^{-1}), T_s and T_g are the solid and gas temperatures (K), α^* is the volumetric heat transfer coefficient (W m^{-3} K^{-1}), λ_s is the thermal conductivity of the solid (W m^{-1} K^{-1}), Δh_R is the reaction enthalpy (J kg^{-1} H_2O), and c_{p,H_2O} is the specific heat capacity of water vapor (J kg^{-1} K^{-1}).

Gas phase

$$\varepsilon\rho_g c_{pg}\frac{\partial T_g}{\partial t}+\rho_g c_{pg}\mathbf{v}\cdot\nabla T_g=\alpha^*(T_s-T_g)+\left(\varepsilon\frac{\partial P}{\partial t}+\mathbf{v}\cdot\nabla P\right)-\nabla\cdot\left(-\varepsilon\lambda_g\nabla T_g\right) \quad (7.6)$$

where c_{pg} is the specific heat capacity of the gas phase ($\mathrm{J\,kg^{-1}\,K^{-1}}$) and λ_g is the gas thermal conductivity ($\mathrm{W\,m^{-1}\,K^{-1}}$).

Reactor wall

$$\rho_{st} c_{p,st} \frac{\partial T_w}{\partial t} = -\nabla \cdot \left(-\lambda_{st} \nabla T_w\right). \tag{7.7}$$

where ρ_{st} is the wall density ($\mathrm{kg\,m^{-3}}$), $c_{p,st}$ is the wall heat capacity ($\mathrm{J\,kg^{-1}\,K^{-1}}$), T_w is the wall temperature (K), and λ_{st} is the wall thermal conductivity ($\mathrm{W\,m^{-1}\,K^{-1}}$).

Effective Thermal Conductivity

The effective conductivity of the porous bed is estimated as follows:

$$\lambda_e = \varepsilon \lambda_g + (1-\varepsilon)\lambda_s = (1-\sqrt{1-\varepsilon})\lambda_{\text{gas}} + (1-\varepsilon)\lambda_s. \tag{7.8}$$

where λ_e is the effective thermal conductivity of the porous bed ($\mathrm{W\,m^{-1}\,K^{-1}}$).

7.2.3 Reaction kinetics implemented via user-defined functions

To accurately reproduce the experimentally validated kinetic behaviour of both processes, the reaction rates were implemented in ANSYS Fluent using user-defined functions (UDFs), as seen in Appendix A. This approach allows the local reaction rate to depend on temperature, steam partial pressure, and solid conversion, a feature not available with the standard ANSYS Fluent reaction models.

Equilibrium vapour pressure

The equilibrium partial pressure of water vapour over the $CaO/Ca(OH)_2$ system is evaluated according to the correlation proposed by Schaube et al.:

$$P_{\text{eq}}(T) = 10^5 \exp\left(-\frac{12845}{T} + 16.508\right) \tag{7.9}$$

where T is the local solid temperature in kelvin.

Local steam partial pressure

Assuming ideal gas behaviour, the local partial pressure of water vapour is calculated as:

$$P_{H_2O} = \frac{\rho \, Y_{H_2O}}{M_{H_2O}} \, R \, T \tag{7.10}$$

where ρ is the gas density, Y_{H_2O} is the mass fraction of water vapour, M_{H_2O} is the molar mass of water, and R is the universal gas constant.

Hydration kinetics

The hydration reaction proceeds when the local steam partial pressure exceeds the equilibrium pressure:

$$P_{H_2O} > P_{eq} \tag{7.11}$$

The pressure driving force is defined as:

$$h_P = \left(\frac{P_{H_2O}}{P_{eq}} - 1 \right)^{n_p} \qquad n_p = 0.83 \tag{7.12}$$

The solid conversion X is defined as the reacted fraction of CaO. The morphology-based conversion function adopted is:

$$g(X) = 3(1 - X) \left[-\ln(1 - X) \right]^{2/3} \tag{7.13}$$

The temperature-dependent reaction rate constant follows an Arrhenius expression:

$$k(T) = \eta_r A_0 \exp\left(-\frac{E_a}{RT} \right) \tag{7.14}$$

where $A_0 = 1.3945 \times 10^4 \, \mathrm{s^{-1}}$, $E_a = 8.95 \times 10^4 \, \mathrm{J\,mol^{-1}}$, and η_r are particle efficiency factors.

The local conversion rate is thus expressed as:

$$\frac{\mathrm{d}X}{\mathrm{d}t} = k(T) \, g(X) \, h_P \tag{7.15}$$

The corresponding surface molar reaction rate supplied to the solver is:

$$r_{\mathrm{hyd}} = \frac{\mathrm{d}X}{\mathrm{d}t}\, Z_0\, \rho_{\mathrm{site}} \tag{7.16}$$

Dehydration kinetics

The dehydration reaction occurs when the local steam partial pressure is lower than the equilibrium pressure:

$$P_{\mathrm{H_2O}} < P_{\mathrm{eq}} \tag{7.17}$$

The pressure driving force for dehydration is expressed as:

$$h_P = \left(1 - \frac{P_{\mathrm{H_2O}}}{P_{\mathrm{eq}}}\right)^{n_p} \qquad n_p = 3 \tag{7.18}$$

Following the Schaube kinetic model, two different kinetic regimes are considered depending on the solid conversion.

For low conversion levels ($X < 0.2$):

$$k_1(T) = A_1 \exp\left(-\frac{E_1}{RT}\right), \qquad f(X) = (1 - X) \tag{7.19}$$

with $A_1 = 1.94 \times 10^{12}\,\mathrm{s^{-1}}$ and $E_1 = 1.88 \times 10^5\,\mathrm{J\,mol^{-1}}$.

For higher conversion levels ($X \geq 0.2$):

$$k_2(T) = A_2 \exp\left(-\frac{E_2}{RT}\right), \qquad f(X) = 2\sqrt{1 - X} \tag{7.20}$$

with $A_2 = 8.96 \times 10^{9}\,\mathrm{s^{-1}}$ and $E_2 = 1.62 \times 10^5\,\mathrm{J\,mol^{-1}}$.

The conversion rate during dehydration is therefore written as:

$$\frac{\mathrm{d}X}{\mathrm{d}t} = k(T)\, f(X)\, h_P \tag{7.21}$$

and the surface molar reaction rate is given by:

$$r_{\mathrm{deh}} = \frac{\mathrm{d}X}{\mathrm{d}t}\, Z_0\, \rho_{\mathrm{site}} \tag{7.22}$$

Volumetric reaction rate

The user-defined functions compute the reaction kinetics in terms of a surface molar reaction rate, r_s, expressed per unit reactive surface area. To couple the reaction kinetics with the species and energy conservation equations, the corresponding volumetric reaction rate q_R is defined as:

$$q_R = a_s\, r_s \qquad [\mathrm{kmol\,m^{-3}\,s^{-1}}] \tag{7.23}$$

where a_s is the specific reactive surface area of the porous bed.

For hydration and dehydration processes, the volumetric reaction rates are therefore written as:

$$q_{R,\mathrm{hyd}} = a_s\, r_{\mathrm{hyd}}, \qquad q_{R,\mathrm{deh}} = a_s\, r_{\mathrm{deh}} \tag{7.24}$$

Coupling with transport equations

The reaction rates defined above are introduced into the numerical model as source terms in the species and energy equations, accounting for water vapour consumption or release and for the associated endothermic or exothermic heat effects. The complete UDF implementations corresponding to these kinetic expressions are reported in Appendix A.

7.3 Simulation Results

The accuracy of the present numerical model was assessed by comparing its predictions with experimental data reported by Schaube *et al.* [123]. In the referenced experiments, the temperature evolution corresponds to a rehydration cycle, characterised by an initial reaction-driven heating phase followed by a cooling phase governed by convective heat removal by the gas flow and heat losses to the surroundings. Figure 7.6 illustrates the comparison between the simulated temperature evolution and the experimental measurements at two representative locations, denoted as T7 and T1.

At location T7, the experimental results show a rapid temperature rise up to approximately 500 °C, followed by a gradual cooling after around 20 minutes. The model reproduces the initial heating phase with good accuracy, capturing both the magnitude and the trend of the experimental data. However, in the cooling region, the simulation tends to overpredict the temperature decay rate, which leads to slightly higher values than those observed experimentally between 30–50 minutes. This discrepancy may be attributed to simplifications in the heat transfer boundary conditions or uncertainties in material properties such as thermal conductivity and heat capacity. For location T1, a similar trend is observed. The model closely follows the sharp initial increase in temperature but slightly underpredicts the cooling rate compared to the experimental data. While deviations are visible during the transient stage, the overall agreement between simulation and experiment remains satisfactory.

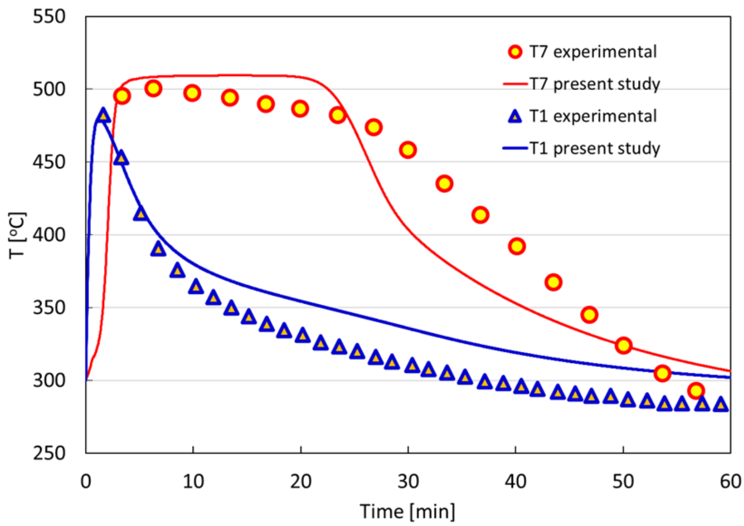

FIGURE 7.6: Validation of numerical results with experimental data.

The simulations provide insights into the spatial and temporal evolution of heat transfer within the system, as will be shown in the following subsections for both hydration and dehydration processes.

7.3.1 Hydration Process

Figure 7.7 shows the temperature contours at different times during the hydration reaction. The inlet is located on the left-hand side, where the reactant gas enters the reactor. At the early stage (10 minutes), the inlet region exhibits a strong temperature rise due to the exothermic nature of the hydration reaction. The hot zone then propagates gradually toward the outlet as the reaction front advances. After 20 minutes, most of the bed is already at elevated temperature, with values above 700 K, indicating intensive reaction activity. As time progresses (30–60 minutes), the system cools down

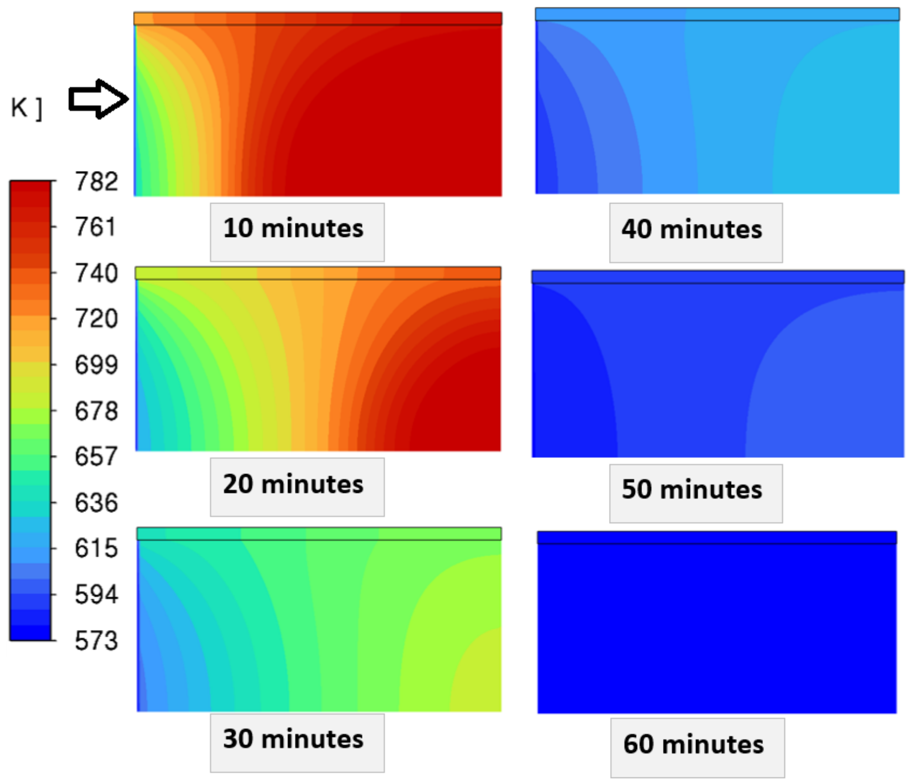

FIGURE 7.7: Temperature distribution at different times during the hydration process. The inlet is on the left-hand side.

and becomes more uniform. By 60 minutes, the reactor approaches thermal equilibrium, with temperatures around 580 K across the entire domain. This behavior confirms that hydration is a strongly exothermic process that leads to rapid temperature buildup near the inlet, followed by a redistribution of heat along the bed until steady conditions are reached.

7.3.2 Dehydration Process

In contrast, Figure 7.8 depicts the transient thermal fields during the dehydration reaction. At the early stage (10 minutes), the temperature near the inlet remains relatively low, since the dehydration process is endothermic and requires heat input. A cold zone is observed near the inlet, which penetrates deeper into the bed as the reaction progresses.

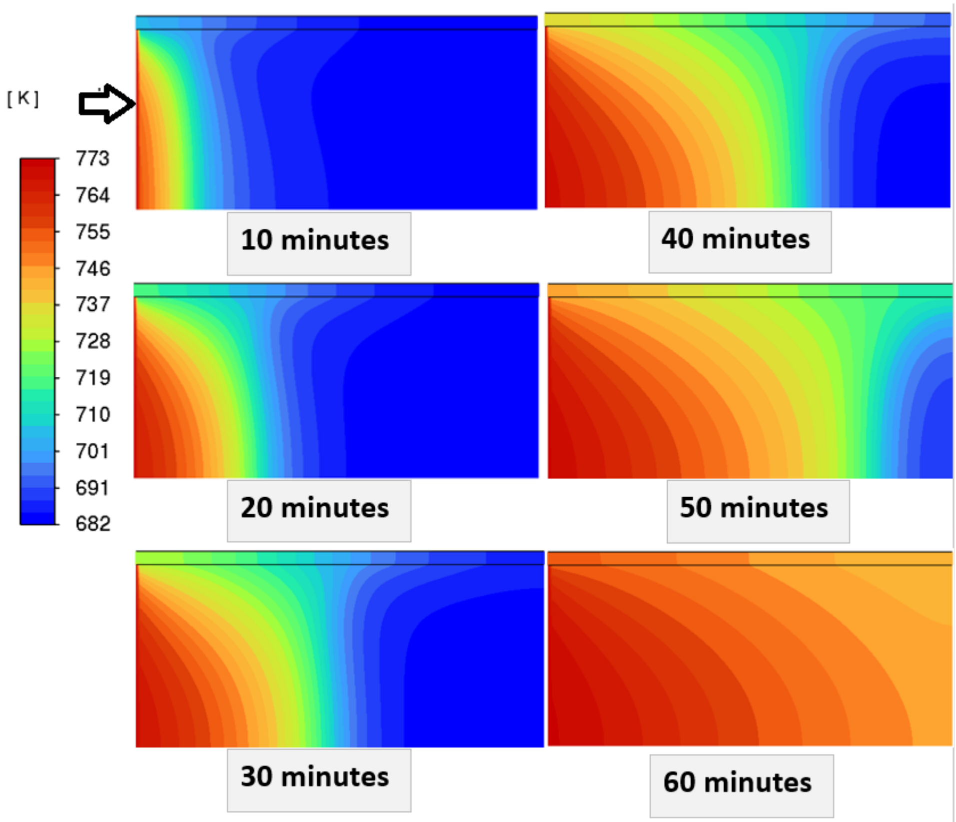

FIGURE 7.8: Temperature distribution at different times during the dehydration process. The inlet is on the left-hand side.

Between 20 and 40 minutes, the temperature gradients become more pronounced, with a significant difference between the inlet (left) and outlet (right) regions. This indicates the strong local cooling effect caused by the endothermic reaction front moving through the bed. After 50 minutes, heat is progressively absorbed throughout the material, and the outlet region becomes dominant in terms of higher temperatures. By 60 minutes, the bed exhibits an almost uniform distribution with elevated temperatures around 760 K, showing that the dehydration front has passed completely through the material.

7.3.3 Comparison of Hydration and Dehydration Behavior

The results highlight the contrasting thermal characteristics of the two processes. Hydration generates heat and results in sharp local hot spots near the inlet, which gradually dissipate as the system equilibrates. Conversely, dehydration consumes heat, leading to a pronounced cooling effect at the inlet and a delayed propagation of the reaction front toward the outlet. These findings emphasize the importance of accounting for the thermodynamic nature of the reaction when designing and optimizing the thermal management strategy of the system.

7.4 Integration of Thermochemical Storage with Parabolic Trough Systems

Although the core focus of this thesis is the thermal–hydraulic optimization of parabolic trough receivers, improving receiver performance alone does not guarantee enhanced plant-level performance. Modern concentrating solar power systems require not only efficient solar energy collection but also reliable dispatchability. In this context, thermal energy storage becomes a crucial system-level component that determines the overall effectiveness and flexibility of parabolic trough plants.

The work presented in Chapters 3–6 addresses receiver-scale challenges, including non-uniform heat flux, internal heat transfer enhancement, vacuum degradation, and heat-loss mechanisms. However, the thermal energy delivered by optimized receivers must ultimately be stored and released efficiently to ensure continuous power production during transient or non-solar periods.

For this reason, Chapter 7 expands the research perspective from component-level optimization to system-level integration. The thermochemical energy storage model developed and described in previous sections investigates the $CaO/Ca(OH)_2$ reaction system. This system operates within a temperature range that is compatible with parabolic trough outlet conditions. Figure 7.9 shows a schematic diagram of thermochemical storage for a PTC system. By numerically modeling coupled heat transfer, mass transport, and reaction kinetics using the same CFD-based methodology adopted in earlier chapters, this work maintains methodological continuity while addressing the broader objective of improving the overall efficiency and dispatchability of parabolic trough solar plants.

Therefore, this chapter of the thesis should not be interpreted as a deviation from the main research line but as a natural extension that connects receiver optimization to plant-level energy management and long-duration storage.

Simple calculations of $CaO/Ca(OH)_2$ thermochemical storage based on PTC plant operating conditions (such as temperature limits) for hydration (discharging) and dehydration (charging) are shown in Tables 7.1 and 7.2. As seen in the hydration kinetics equations (7.11 and 7.12), the steam pressure must exceed the equilibrium pressure, which is assumed to be 30 kPa, and the pressure driving force (h_p) must be greater than 1, as calculated in Table 7.1. For the dehydration kinetics equations (7.17 and 7.18), the steam pressure must be lower than the equilibrium pressure, which is assumed to be 0.5 kPa, and the pressure driving force (h_p) must be lower than 1, as calculated in Table 7.2.

TABLE 7.1: Hydration (Discharging)

T(°C)	T (K)	P_{eq} (kPa)	P_{H_2O}/P_{eq}	h_P
260	533	0.0505	594.3	200.4
270	543	0.1087	381.3	138.5
280	553	0.1827	248.6	67.8
290	563	0.2715	116.5	49.3
300	573	0.2715	110.5	49.3
310	583	0.3988	75.2	35.7

TABLE 7.2: Dehydration (Charging)

T(°C)	T (K)	P_{eq} (kPa)	P_{H_2O}/P_{eq}	h_P
400	673	7.6	0.066	0.82
395	668	6.6	0.076	0.79
390	663	5.7	0.088	0.76
385	658	4.9	0.102	0.72
380	653	4.2	0.118	0.69

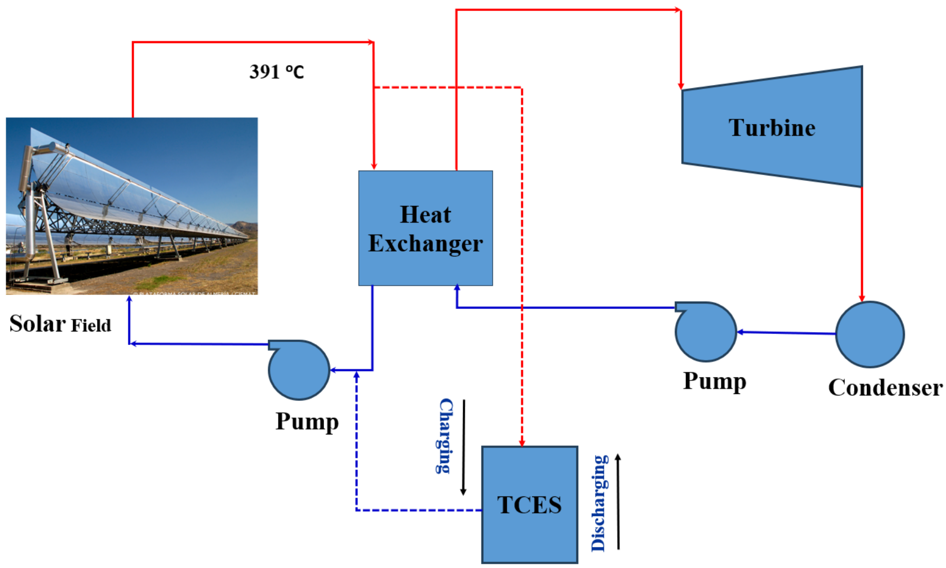

FIGURE 7.9: Schematic diagram of thermochemical storage for a PTC system.

7.5 Conclusions and Future Work

The numerical investigation demonstrated the capability of $Ca(OH)_2$-based TCES systems for efficient energy storage with direct heat transfer. The main conclusions are:

- The developed UDF-based kinetic model successfully captured the reaction dynamics of hydration and dehydration.

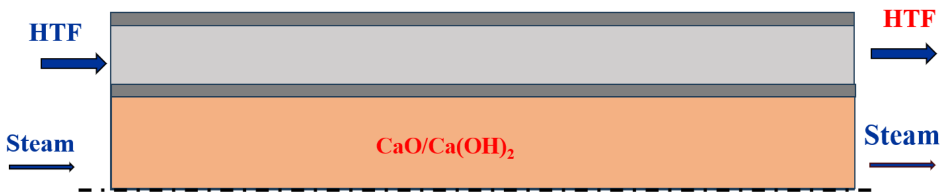

FIGURE 7.10: 2D schematic diagram of an indirect thermochemical reactor for a PTC system.

- Simulation results showed good agreement with experimental data for both charging (dehydration) and discharging (hydration) processes.
- The energy storage performance highlights the strong potential of $Ca(OH)_2$-CaO systems for integration with solar thermal plants, particularly in medium- to high-temperature applications.

Future Work

While the present work provided valuable insights into the feasibility of $Ca(OH)_2$-based thermochemical storage, further research is required for advancing towards practical implementation. The following aspects are recommended for future work:

- **Integration with Parabolic Trough Systems:** Extend the numerical model to a system-level simulation including a parabolic trough collector as shown in Figure 7.9.
- **Dynamic Simulations:** Couple the TCES model with transient solar irradiance data to evaluate the impact of weather fluctuations and diurnal cycles on overall efficiency and operational stability.
- **Optimization of Heat Exchanger and Reactor Geometry:** Conduct parametric studies on reactor configuration, flow distribution, and packing structure to improve heat transfer and reduce thermal gradients during both charging and discharging for the indirect reactor as shown in Figure 7.10.

- **System Scaling and Industrial Application:** Investigate scale-up to multi-MWh storage units and study integration with turbines or district heating systems for practical deployment.

Chapter 8

Conclusions and future research

This thesis addressed the thermal performance, reliability, and heat-loss mechanisms of parabolic trough collector (PTC) receivers under realistic operating conditions. The research focused on the coupled effects of non-uniform solar heat flux, internal heat transfer enhancement using longitudinal fins, vacuum degradation in the annular region, and the presence of residual gases such as air and hydrogen. The work was motivated by the need to mitigate circumferential temperature gradients, reduce thermal stresses, and limit heat losses that directly affect the efficiency and operational lifespan of commercial parabolic trough receivers.

The thesis is structured around three core research themes: (i) enhancement of internal heat transfer through optimized longitudinal fin configurations, (ii) quantification of heat losses under varying annulus vacuum levels and atmospheric conditions, and (iii) assessment of receiver thermal behaviour under realistic degradation scenarios, including hydrogen accumulation and wind effects. The conclusions drawn from these investigations are presented below as answers to the research questions formulated in Chapter 1.

8.1 Answers to Specific Research Questions

1. *How do the number, height, and circumferential placement of longitudinal fins influence heat transfer performance and temperature uniformity in parabolic trough receivers under non-uniform heat flux conditions?*

A comprehensive numerical investigation was conducted to evaluate longitudinally finned parabolic trough receivers subjected to the inherently non-uniform circumferential heat flux characteristic of PTC systems. A novel concept of asymmetrically distributed fins, varying both in circumferential position and height, was introduced to better match the local heat flux distribution around the absorber tube.

The results demonstrate that fin placement and geometry strongly influence both the internal heat transfer mechanisms and the circumferential temperature distribution. Fins located in regions exposed to higher local heat flux effectively reduce maximum wall temperatures and circumferential temperature differences. In particular, fins placed on the lower half of the receiver enhance conductive heat transfer due to direct exposure to high heat flux, while fins on the upper (colder) half promote flow redistribution by displacing the high-velocity core of the heat transfer fluid toward the lower region, thereby enhancing convective heat transfer.

By strategically combining shorter fins in the high-flux region with longer fins in the low-flux region, both conductive and convective heat transfer mechanisms are simultaneously improved. The best-performing configurations (4FCase4, 6FCase4, and 8FCase4) achieved maximum improvements in the overall Nusselt number of 17.6%, 33.0%, and 45.6%, respectively, relative to a smooth receiver. Correspondingly, peak absorber temperatures were reduced by up to 36.2 K, and total heat losses were reduced by up to 18.0%.

These findings confirm that asymmetric longitudinal fin configurations provide a simple, cost-effective, and manufacturable solution for significantly improving the thermal performance and temperature uniformity of parabolic trough receivers.

Future Work

Future research should focus on extending the present numerical framework to include thermo-mechanical stress analysis in order to directly quantify the reduction in thermal stresses and deformation resulting from optimized fin configurations. Experimental validation of asymmetric fin designs under realistic solar flux conditions would further strengthen their applicability for commercial receivers. Additionally, the long-term effects of fouling, thermal cycling, and material degradation on fin performance should be investigated to assess durability over the receiver lifetime.

2. *How does vacuum level and atmospheric condition influence heat losses in smooth and finned parabolic trough receivers?*

The influence of annular region pressure, inlet heat transfer fluid temperature, and atmospheric conditions on receiver heat losses were systematically investigated. The results show that under low vacuum pressures, conduction heat loss is negligible and radiation dominates the total heat loss. However, as the annulus pressure increases, conductive heat transfer becomes significant, reducing the relative contribution of radiation to the total heat loss.

When the annular space is filled with air at atmospheric pressure, the total heat loss is nearly doubled compared to full vacuum conditions. The incorporation of longitudinal fins was shown to successfully reduce the outer surface temperature of the receiver, thereby primarily reducing radiative heat losses. As a result, the total heat loss for finned receivers was reduced by approximately 9% compared to smooth receivers under identical operating conditions.

Furthermore, atmospheric conditions were found to play a non-negligible role. Increased wind speed and lower ambient temperatures lead to higher convective heat losses, highlighting the importance of considering realistic environmental conditions in receiver performance assessment.

Future Work

Future studies should investigate transient vacuum degradation scenarios, including partial vacuum recovery and getter saturation effects, to better represent long-term field operation. Coupling the receiver model with meteorological datasets from operational solar fields would allow for improved annual performance prediction. In addition, experimental campaigns under controlled vacuum and wind conditions would be valuable to further validate the numerical heat-loss models developed in this thesis.

3. *What is the impact of hydrogen accumulation and realistic operating conditions on the thermal behaviour and heat losses of parabolic trough receivers?*

   A detailed three-dimensional conjugate heat transfer analysis was performed to investigate receiver thermal behaviour under vacuum and low-pressure hydrogen conditions in the annulus. The results show that hydrogen accumulation dramatically alters the heat transfer mechanisms within the annular space. Compared to vacuum conditions, the presence of hydrogen increases total heat losses by approximately a factor of three.

   For example, at a mass flow rate of 3 kg/s and an inlet temperature of 390 °C, heat loss increased from 230.9 W/m under vacuum conditions to 723.2 W/m with hydrogen in the annulus. Hydrogen was also found to slightly lower absorber surface temperatures while substantially increasing glass envelope temperatures, by up to 142 °C, due to enhanced conductive and convective heat transfer.

   Parametric analysis revealed that increasing the mass flow rate from 3 kg/s to 6 kg/s reduced the maximum circumferential temperature difference on the absorber surface by 40.4%, improving temperature uniformity and mitigating thermal stresses. Higher inlet temperatures further enhanced temperature uniformity. Wind-speed analysis showed that external flow increased total heat losses by up to 18%, while significantly reducing glass envelope temperatures, particularly under hydrogen-filled annulus conditions.

   These results clearly demonstrate the necessity of maintaining high-vacuum conditions to minimize energy dissipation and preserve receiver performance.

   Future Work

   Future research should investigate coupled hydrogen permeation, getter degradation, and vacuum loss models to enable predictive maintenance strategies for commercial receivers. The integration of real-time monitoring data with CFD-based digital twins could support condition-based operation and early fault detection. Moreover, mitigation strategies such as advanced getter materials, hydrogen barriers, or alternative annulus gas management techniques should be explored.

In addition, future studies should analyse and optimise various end-bellows configurations (such as Solel UVAC and Schott joints), with particular emphasis on their thermal performance under degraded vacuum conditions.

4. *Can a new performance metric be developed to enable meaningful comparison of finned and smooth receivers under non-uniform heat flux conditions?*

   A novel performance evaluation approach was developed to enable meaningful comparison between finned and smooth receivers under non-uniform heat flux conditions. Conventional metrics based solely on inner Nusselt number or pressure drop were shown to be insufficient, as they do not adequately capture circumferential temperature gradients or peak temperatures.

   The proposed evaluation framework incorporates both thermal enhancement and hydraulic penalties while accounting for non-uniform heating, allowing clearer identification of optimal fin configurations. This approach proved more effective than commonly used methods in the literature and enabled robust comparison of different receiver designs under realistic operating conditions.

8.2 Overall Remarks

Overall, this thesis provides a unified and realistic numerical framework for analyzing and optimizing the thermal performance of parabolic trough receivers. By simultaneously addressing internal heat transfer enhancement and external heat-loss mechanisms under non-ideal operating conditions, the work bridges an important gap between simplified academic models and real-world receiver behaviour. The results offer practical design guidelines for finned receiver optimization, improved understanding of vacuum degradation effects, and valuable insights for enhancing the efficiency, reliability, and longevity of solar thermal power plants.

The methodologies and findings presented in this thesis contribute to the development of next-generation high-performance parabolic trough receivers and support the broader deployment of reliable and dispatchable concentrating solar thermal technologies.

Finally, the thermochemical energy storage modelling framework developed in the last part of the PhD programme can be extended toward large-scale reactor optimisation and dynamic integration with parabolic trough systems. Future studies could address multi-cycle operation, material ageing, and control strategies under variable solar input. The combined optimisation of high-performance receivers and advanced thermal energy storage represents a promising pathway toward more efficient and dispatchable solar thermal power plants.

Appendix A

A.0.1 User-defined functions (UDFs) for hydration and dehydration kinetics

```c
#include "udf.h"
#include <math.h>   /* for log(), pow() */

/* ====== user knobs you may tune ====== */
#define ETA_R        1          /* particle efficiency (paper B) */
#define N_PRESS      0.83          /* pressure exponent */
#define A0_S         1.3945e4      /* s^-1, Schaube far-from-eq pre-exponent */
#define E_JPMOL      8.9486e4      /* J/mol, Schaube far-from-eq activation energy */
#define R_UNIV       8.314462618e0 /* J/(mol K) */
#define MW_H2O       18.01528e-3   /* kg/mol */
#define SITE_RHO     0.003337144       /* kmol/m^2  (put your Site Density from GUI here) */
#define Z0_CAO       1.0           /* initial site fraction of CaO at t=0 (from GUI) */

/* small clamps to avoid log(0) / pow() domain issues */
#define Z_EPS        1.0e-12

/* Peq of H2O over Ca(OH)2/CaO, Pa  (ln(Peq/1e5)= -12845/T + 16.508; T in K) */
static inline real Peq_Pa(real T)
{
    return 1.0e5 * exp(-12845.0/T + 16.508);
}

```

```c
/* p_i from mass fraction (ideal gas) */
static inline real p_part(real rho, real Y, real MW,
    real T)
{
    /* rho[kg/m3], MW[kg/mol] => n_i [mol/m3] = rho*Y/MW
        ; p_i = n_i*R*T */
    return (rho*Y/MW) * R_UNIV * T;   /* Pa */
}

/* ===== CaO + H2O -> Ca(OH)2 hydration (surface rate)
    ===== */
DEFINE_SR_RATE(surface_rate_UDF_A, c, t, r, mw, yi, rr)
{
    /* state */
    const real T   = C_T(c,t);
    const real rho = C_R(c,t);

    /* steam partial pressure */
    const int  iH2O   = mixture_specie_index(
        THREAD_MATERIAL(t), "h2o");
    if (iH2O < 0) { *rr = 0.0; return; }
    const real Y_H2O  = yi[iH2O];
    const real pH2O   = p_part(rho, Y_H2O, MW_H2O, T);

    /* equilibrium limit */
    const real Peq = Peq_Pa(T);
    if (pH2O <= Peq) { *rr = 0.0; return; }
    const real hP  = pow((pH2O/Peq) - 1.0, N_PRESS);

    /* Arrhenius (with bed-scale reduction) */
    const real K   = (ETA_R * A0_S) * exp(-E_JPMOL/(
        R_UNIV*T)); /* 1/s */

    /* site fraction of CaO (current) */
    const int  iCaO  = mixture_specie_index(
        THREAD_MATERIAL(t), "cao");
    if (iCaO < 0) { *rr = 0.0; return; }
    /* (1 - X) = Z/Z0; clamp it to (0,1) to keep log()
        defined and negative */
    real one_minus_X = yi[iCaO] / Z0_CAO;
    if (one_minus_X < Z_EPS)        one_minus_X = Z_EPS;
```

```
    else if (one_minus_X > 1.0-Z_EPS) one_minus_X = 1.0
        - Z_EPS;

    /* your model term: 3*(1-X)*(-ln(1-X))^(2/3) */
    const real s     = -log(one_minus_X);       /*
        positive for 0<one_minus_X<1 */
    const real g     = 3.0 * one_minus_X * pow(s,
        2.0/3.0);

    const real dXdt = K * g * hP;               /* 1/s */

    /* surface molar rate (kmol/m^2-s) of CaO
        consumption */
    const real r_surf = dXdt * Z0_CAO * SITE_RHO;

    *rr = MAX(r_surf, 0.0);
}
```

LISTING A.1: ANSYS Fluent UDF for hydration

```
#include "udf.h"
#include <math.h>

/* ========== */
#define ETA_R          1.0           /* particle efficiency
    (bed-scale reduction, if needed) */
#define N_PRESS        3.0           /* dehydration
    pressure exponent (Schaube) */
#define R_UNIV         8.314462618   /* J/(mol K) */
#define MW_H2O         18.01528e-3   /* kg/mol */
#define SITE_RHO       0.00333       /* kmol/m^2  (Site
    Density from GUI) */
#define Z0_CAOH2       1.0           /* initial site
    fraction of Ca(OH)2 at t=0 */

#define Z_EPS          1.0e-12

/* Peq of H2O over Ca(OH)2/CaO, Pa  (ln(Peq/1e5)=
    -12845/T + 16.508) */
static inline real Peq_Pa(real T)
{
```

```
    return 1.0e5 * exp(-12845.0/T + 16.508);  /* Schaube
        2012 */
}

/* partial pressure from mass fraction (ideal gas) */
static inline real p_part(real rho, real Y, real MW,
    real T)
{
    return (rho*Y/MW) * R_UNIV * T;   /* Pa */
}

/* ===== Ca(OH)2 -> CaO + H2O dehydration (surface rate)
     ===== */
DEFINE_SR_RATE(surface_rate_UDF_dehydration, c, t, r, mw
    , yi, rr)
{
    const real T   = C_T(c,t);
    const real rho = C_R(c,t);

    /* steam partial pressure */
    const int  iH2O  = mixture_specie_index(
        THREAD_MATERIAL(t), "h2o");
    if (iH2O < 0) { *rr = 0.0; return; }
    const real Y_H2O = yi[iH2O];
    const real pH2O  = p_part(rho, Y_H2O, MW_H2O, T);

    /* equilibrium */
    const real Peq = Peq_Pa(T);
    if (pH2O >= Peq) { *rr = 0.0; return; }  /* no
        driving force for dehydration */
    const real hP  = pow(1.0 - (pH2O/Peq), N_PRESS);

    /* site fraction of Ca(OH)2 (current); (1 - X) = Z/
        Z0 */
    const int  iCaOH2 = mixture_specie_index(
        THREAD_MATERIAL(t), "caoh2");
    if (iCaOH2 < 0) { *rr = 0.0; return; }
    real one_minus_X = yi[iCaOH2] / Z0_CAOH2;
    if (one_minus_X < Z_EPS)           one_minus_X =
        Z_EPS;
    else if (one_minus_X > 1.0-Z_EPS)  one_minus_X = 1.0
         - Z_EPS;
```

```

    const real X  = 1.0 - one_minus_X;

    /* Two kinetic regimes (Schaube 2012):
       X < 0.2 : F1  (A=1.9425e12 s^-1, E=187.88 kJ/mol)
       X >=0.2 : R2  (A=8.9583e9  s^-1, E=162.26 kJ/mol;
            f(X)=2*(1-X)^(1/2))  */
    real A, E_JPMOL, fX;
    if (X < 0.2) {
        A         = 1.9425e12;          /* 1/s */
        E_JPMOL   = 187.88e3;           /* J/mol */
        fX        = (1.0 - X);          /* F1 */
    } else {
        A         = 8.9583e9;           /* 1/s */
        E_JPMOL   = 162.26e3;           /* J/mol */
        fX        = 2.0*sqrt(1.0 - X); /* R2 */
    }

    const real K = (ETA_R * A) * exp(-E_JPMOL/(R_UNIV*T)
       );  /* 1/s */

    const real dXdt = K * fX * hP;     /* 1/s */

    /* surface molar rate (kmol/m^2-s) of Ca(OH)2
       consumption */
    const real r_surf = dXdt * ZO_CAOH2 * SITE_RHO;

    *rr = MAX(r_surf, 0.0);
}
```

LISTING A.2: ANSYS Fluent UDF for dehydration

Bibliography

[1] Md Tasbirul Islam, Nazmul Huda, A.B. Abdullah, and R. Saidur. A comprehensive review of state-of-the-art concentrating solar power (csp) technologies: Current status and research trends. *Renewable and Sustainable Energy Reviews*, 91:987–1018, 2018.

[2] María Isabel Roldán Serrano. *Concentrating Solar Thermal Technologies*, pages 11–24. Springer International Publishing, Cham, 2017.

[3] A. Fernández-García, E. Zarza, L. Valenzuela, and M. Pérez. Parabolic-trough solar collectors and their applications. *Renewable and Sustainable Energy Reviews*, 14(7):1695–1721, 2010.

[4] Zhiyong Wu, Dongqiang Lei, Guofeng Yuan, Jiajia Shao, Yunting Zhang, and Zhifeng Wang. Structural reliability analysis of parabolic trough receivers. *Applied Energy*, 123:232–241, 2014.

[5] Guillermo Espinosa-Rueda, José Luis Navarro Hermoso, Noelia Martínez-Sanz, and Manuel Gallas-Torreira. Vacuum evaluation of parabolic trough receiver tubes in a 50 MW concentrated solar power plant. *Solar Energy*, 139:36–46, 2016.

[6] Jian Li, Zhifeng Wang, Dongqiang Lei, and Jianbin Li. Hydrogen permeation model of parabolic trough receiver tube. *Solar Energy*, 86:1187–1196, 2012.

[7] Henry Price, Russell Forristall, Timothy Wendelin, Allan Lewandowski, Timothy Moss, and Carin Gummo. Field survey of parabolic trough receiver thermal performance, 2006.

[8] Hank Price, Eckhard Lüpfert, David Kearney, Eduardo Zarza, Gilbert Cohen, Randy Gee, and Rod Mahoney. Advances in parabolic trough solar power technology. *Journal of Solar Energy Engineering, Transactions of the ASME*, 124:109–125, 2002.

[9] A.Z. Hafez, A.M. Attia, H.S. Eltwab, A.O. ElKousy, A.A. Afifi, A.G. AbdElhamid, A.N. AbdElqader, S-E.K. Fateen, K.A. El-Metwally, A. Soliman, and I.M. Ismail. Design analysis of solar parabolic trough thermal collectors. *Renewable and Sustainable Energy Reviews*, 82:1215–1260, 2018.

[10] O. Achkari, A. El Fadar, M. Mortadi, and Y. Elaouzy. Investigation of commercial scale csp plants performance: Effect of their installed capacity. *Next Sustainability*, 6:100143, 2025.

[11] Henry Price, Mary Jane Hale, Rod Mahoney, Carin Gummo, Robert Fimbres, and Robert Cipriani. Isec2004-65178 developments in high temperature parabolic trough receiver technology, 2004.

[12] Dongqiang Lei, Xuqiang Fu, Yucong Ren, Fangyuan Yao, and Zhifeng Wang. Temperature and thermal stress analysis of parabolic trough receivers. *Renewable Energy*, 136:403–413, 2019.

[13] Wassila Ajbar, A. Parrales, A. Huicochea, and J. A. Hernández. Different ways to improve parabolic trough solar collectors' performance over the last four decades and their applications: A comprehensive review. *Renewable and Sustainable Energy Reviews*, 156:111947, 2022.

[14] M. Allam, M. Tawfik, M. Bekheit, and E. El-Negiry. Heat transfer enhancement in parabolic trough receivers using inserts: A review. *Sustainable Energy Technologies and Assessments*, 48, 2021.

[15] Aggrey Mwesigye and Josua P. Meyer. Optimal thermal and thermodynamic performance of a solar parabolic trough receiver with different nanofluids and at different concentration ratios. *Applied Energy*, 193:393–413, 2017.

[16] Pedram Alamdari, Mehdi Khatamifar, and Wenxian Lin. Heat loss analysis review: Parabolic trough and linear Fresnel collectors. *Renewable and Sustainable Energy Reviews*, 199:114497, 2024.

[17] Magdalena Barnetche, Luis F. González-Portillo, and Rubén Abbas. Optimum integration of latent heat storage in a solar thermal system for industrial processes: In series or in parallel? *Applied Thermal Engineering*, 232:121090, 2023.

[18] Marco A. David-Hernández, Antonio Cazorla-Marín, José Gonzálvez-Maciá, Jorge Payá-Herrero, and Miguel Frasquet. Enhanced monitoring and dynamic analysis of a concentrated solar thermal experimental plant for steam production. *Applied Thermal Engineering*, 249:123418, 2024.

[19] Bappa Mondal and Ambarish Maji. A brief review on analysis and recent development of parabolic trough collector. *Energy Storage and Saving*, 2025.

[20] Vinod Kumar and Liqiang Duan. Off-design dynamic performance analysis of a solar aided coal-fired power plant. *Energies*, 14, 2021.

[21] Ahmed Bilal Awan, M.N. Khan, Muhammad Zubair, and Evangelos Bellos. Commercial parabolic trough csp plants: Research trends and technological advancements. *Solar Energy*, 211:1422–1458, 2020.

[22] Michael de Oliveira Resende, Monique Ellen Torres da Silva, Augusto Cesar Laviola de Oliveira, Sérgio Zolnier, Eloiny Guimarães Barbosa, and Marcio Arêdes Martins. Experimental study of alternative receiver tube for parabolic trough system for typical summer and winter months in a tropical region. *Applied Thermal Engineering*, 232:121023, 2023.

[23] Hyemin Kim, Veerakumar Chinnasamy, Jeonggyun Ham, and Honghyun Cho. Parabolic trough collectors: A comprehensive review of design innovations, optimization studies and applications. *Energy Conversion and Management*, 327:119534, 2025.

[24] Sanaz Akbarzadeh and Mohammad Sadegh Valipour. Heat transfer enhancement in parabolic trough collectors: A comprehensive review. *Renewable and Sustainable Energy Reviews*, 92:198–218, 2018.

[25] Xingwang Song, Guobo Dong, Fangyuan Gao, Xungang Diao, Liqing Zheng, and Fuyun Zhou. A numerical study of parabolic trough receiver with nonuniform heat flux and helical screw-tape inserts. *Energy*, 77:771–782, 2014.

[26] Aggrey Mwesigye, Tunde Bello-Ochende, and Josua P. Meyer. Heat transfer and entropy generation in a parabolic trough receiver with

wall-detached twisted tape inserts. *International Journal of Thermal Sciences*, 99:238–257, 2016.

[27] Yun Liu, Qun Chen, Kang Hu, and Jun-Hong Hao. Flow field optimization for the solar parabolic trough receivers in direct steam generation systems by the variational principle. *International Journal of Heat and Mass Transfer*, 102:1073–1081, 2016.

[28] Bhavin Mehta, Dattatraya Subhedar, Hitesh Panchal, Zafar Said, Kamal Sharma, Md Irfanul Haque Siddiqui, L Natrayan, and Marc A. Rosen. Twisted tape inserts in parabolic trough solar collectors: Assessment of energy, exergy, and environmental impacts. *Applied Thermal Engineering*, 250:123566, 2024.

[29] Awatef Abidi, A.S. El-Shafay, Mohamed Degani, Kamel Guedri, S. Mohammad Sajadi, and Mohsen Sharifpur. Improving the thermal-hydraulic performance of parabolic solar collectors using absorber tubes equipped with perforated twisted tape containing nanofluid. *Sustainable Energy Technologies and Assessments*, 52:102099, 2022.

[30] Prashant Saini, Atul Dhar, and Satvasheel Powar. Performance evaluation of a parabolic trough collector with a uniform helical wire coil flow insert. *Results in Engineering*, 21:101794, 2024.

[31] Hacı Mehmet Şahin, Eşref Baysal, Ali Rıza Dal, and Necmettin Şahin. Investigation of heat transfer enhancement in a new type heat exchanger using solar parabolic trough systems. *International Journal of Hydrogen Energy*, 40(44):15254–15266, 2015.

[32] İbrahim Halil Yılmaz, Aggrey Mwesigye, and Taha Tuna Göksu. Enhancing the overall thermal performance of a large aperture parabolic trough solar collector using wire coil inserts. *Sustainable Energy Technologies and Assessments*, 39:100696, 2020.

[33] P. Wang, D. Y. Liu, and C. Xu. Numerical study of heat transfer enhancement in the receiver tube of direct steam generation with parabolic trough by inserting metal foams. *Applied Energy*, 102:449–460, 2013.

[34] Hossein Ebadi, Antonio Cammi, Nima Fathi, and Laura Savoldi. Heat transfer enhancement on csp tubular receivers using partially

filled raschig ring porous inserts: A numerical study. *Solar Energy*, 297:113635, 2025.

[35] Hao Peng, Meilin Li, and Xingang Liang. Thermal-hydraulic and thermodynamic performance of parabolic trough solar receiver partially filled with gradient metal foam. *Energy*, 211:119046, 2020.

[36] K. Arshad Ahmed and E. Natarajan. Thermal performance enhancement in a parabolic trough receiver tube with internal toroidal rings: A numerical investigation. *Applied Thermal Engineering*, 162:114224, 2019.

[37] Seyed Ebrahim Ghasemi and Ali Akbar Ranjbar. Numerical thermal study on effect of porous rings on performance of solar parabolic trough collector. *Applied Thermal Engineering*, 118:807–816, 2017.

[38] Behzad Vahedi, Ehsan Golab, Arsalan Nasiri Sadr, and Kambiz Vafai. Thermal, thermodynamic and exergoeconomic investigation of a parabolic trough collector utilizing nanofluids. *Applied Thermal Engineering*, 206:118117, 2022.

[39] Diogo do Carmo Zidan, Cristiana Brasil Maia, and Mohammad Reza Safaei. Performance evaluation of various nanofluids for parabolic trough collectors. *Sustainable Energy Technologies and Assessments*, 50:101865, 2022.

[40] Lizhuang Dou, Bin Ding, Qiang Zhang, Guiyue Kou, and Mingfei Mu. Numerical investigation on the thermal performance of parabolic trough solar collector with synthetic oil/cu nanofluids. *Applied Thermal Engineering*, 227:120376, 2023.

[41] Naima Talem, Sofiane MIHOUB, Lakhdar Boumia, Abdelkader Safa, Javier Navas, Patrice Estellé, and Zouaoui Benayad. Thermal performance of parabolic trough collector using oil-based metal nanofluids. *Applied Thermal Engineering*, 256:124128, 2024.

[42] Anfal Benrezkallah, Yacine Marif, Mohammed Elbar Soudani, Mohamed Mustapha Belhadj, Taha Hamidatou, Naima Mekhloufi, and Ahlam Aouachir. Thermal performance evaluation of the parabolic trough solar collector using nanofluids: A case study in the desert of algeria. *Case Studies in Thermal Engineering*, 60:104797, 2024.

[43] Sovan Kumar Panja, Biplab Das, and Vinyas Mahesh. Performance evaluation of a novel parabolic trough solar collector with nanofluids and porous inserts. *Applied Thermal Engineering*, 258:124495, 2025.

[44] Abhinav Kumar. Comparative investigations on thermal performance assessment of a linear parabolic trough solar collector using various nanofluids and incident angles. *Energy*, 317:134707, 2025.

[45] Vinayagam Mohanavel, K. Logesh, R. Venkatesh, Pradeep Kumar Singh, Ismail Hossain, Manzoore Elahi M. Soudagar, Sami Al Obaid, Sulaiman Ali Alharbi, and Venu Kannan Ramachandaramurthy. Ferric oxide nanofluid on functional properties of parabolic trough solar collector under different flow rate. *Applied Thermal Engineering*, 265:125608, 2025.

[46] M.H. Pahlavanian, A.M. Jadidi, M. Zaboli, et al. Harmonizing green energy: enhancing parabolic trough solar collectors through numerical optimization, twisted tapes, and nanofluids, with an environmental perspective. *Journal of Thermal Analysis and Calorimetry*, 149:9731–9750, 2024.

[47] S. Mojtaba Tabarhoseini and M. Sheikholeslami. Modeling of evacuated tube solar collector involving longitudinal fins and nanofluids. *Sustainable Energy Technologies and Assessments*, 53, 2022.

[48] Hussein A. Mohammed, Hari B. Vuthaluru, and Shaomin Liu. Thermohydraulic and thermodynamics performance of hybrid nanofluids based parabolic trough solar collector equipped with wavy promoters. *Renewable Energy*, 182:401–426, 2022.

[49] Farhan Lafta Rashid, Hakim S. Aljibori, Hayder I. Mohammed, Arman Ameen, Shabbir Ahmad, Mohamed Bechir Ben Hamida, and Ameer H. Al-Rubaye. Recent advances and developments of the application of hybrid nanofluids in parabolic solar collector energy systems and guidelines for future prospects. *Journal of Engineering Research*, 2024.

[50] Arianna Berto, Marco Azzolin, Pascal Lavieille, Andrey Glushchuk, Patrick Queeckers, Stefano Bortolin, Carlo Saverio Iorio, Marc Miscevic, and Davide Del Col. Experimental investigation of liquid film

thickness and heat transfer during condensation in microgravity. *International Journal of Heat and Mass Transfer*, 199:123467, 2022.

[51] D. P. Edwards, A. Hirsa, and M. K. Jensen. Turbulent flow in longitudinally finned tubes. *Journal of Fluids Engineering*, 118:506–513, 1996.

[52] Michael K. Jensen and Alex Vlakancic. Technical note experimental investigation of turbulent heat transfer and fluid flow in internally finned tubes. *International Journal of Heat and Mass Transfer*, 42:1343–1351, 1999.

[53] X. Liu and M. K. Jensen. Geometry effects on turbulent flow and heat transfer in internally finned tubes. *Journal of Heat Transfer*, 123:1035–1044, 2001.

[54] Evangelos Bellos, Christos Tzivanidis, and Dimitrios Tsimpoukis. Multi-criteria evaluation of parabolic trough collector with internally finned absorbers. *Applied Energy*, 205:540–561, 2017.

[55] Evangelos Bellos and Christos Tzivanidis. Enhancing the performance of a parabolic trough collector with combined thermal and optical techniques. *Applied Thermal Engineering*, 164:114496, 2020.

[56] Burak Kurşun. Thermal performance assessment of internal longitudinal fins with sinusoidal lateral surfaces in parabolic trough receiver tubes. *Renewable Energy*, 140:816–827, 2019.

[57] Evangelos Bellos and Christos Tzivanidis. Investigation of a star flow insert in a parabolic trough solar collector. *Applied Energy*, 224:86–102, 2018.

[58] Hao Peng, Meilin Li, Fenfen Hu, and Shiyu Feng. Performance analysis of absorber tube in parabolic trough solar collector inserted with semi-annular and fin shape metal foam hybrid structure. *Case Studies in Thermal Engineering*, 26:101112, 2021.

[59] Peng Liu, Ting Ting Ren, Yan Lin Ge, Wei Liu, and Lin Gen Chen. Performance analyses of a novel finned parabolic trough receiver with inner tube for solar cascade heat collection. *Science China Technological Sciences*, 66:1417–1434, 2023.

[60] Xiangtao Gong, Fuqiang Wang, Haiyan Wang, Jianyu Tan, Qingzhi Lai, and Huaizhi Han. Heat transfer enhancement analysis of tube receiver for parabolic trough solar collector with pin fin arrays inserting. *Solar Energy*, 144:185–202, 2017.

[61] Z. D. Cheng, Y. L. He, and F. Q. Cui. Numerical study of heat transfer enhancement by unilateral longitudinal vortex generators inside parabolic trough solar receivers. *International Journal of Heat and Mass Transfer*, 55:5631–5641, 2012.

[62] Adel Laaraba and Ghazali Mebarki. Enhancing thermal performance of a parabolic trough collector with inserting longitudinal fins in the down half of the receiver tube. *Journal of Thermal Science*, 29:1309–1321, 2020.

[63] G. L. Harding. Helium permeation in all-glass tubular evacuated solar energy collectors. *Solar Energy Materials*, 5:141–147, 1981.

[64] Koenraad F. Beckers and Greg C. Glatzmaier. Addressing solar power plant heat transfer fluid degradation: Experimental measurements of hydrogen transport properties in binary eutectic biphenyl/diphenyl ether. *Solar Energy*, 173:304–312, 2018.

[65] Xabier Olano, Alberto García de Jalón, David Pérez, Javier García Barberena, Javier López, and Martín Gastón. Outcomes and features of the inspection of receiver tubes (ITR) system for improved O&M in parabolic trough plants. *AIP Conference Proceedings*, 2033(1):030011, 2018.

[66] B. Kalidasan, Muhammed A. Hassan, A. K. Pandey, and Subramaniyan Chinnasamy. Linear cavity solar receivers: A review. *Applied Thermal Engineering*, 221:119815, 2023.

[67] Frank Burkholder, Michael Brandemuehl, Henry Price, Judy Netter, Chuck Kutscher, and Ed Wolfrum. Parabolic trough receiver thermal testing. *Proceedings of the ASME 2007 Energy Sustainability Conference*, pages 961–970, 2007.

[68] Loreto Valenzuela, Rafael López-Martín, Carmen M. Amador-Cortés, and Christoph Hilgert. Experimental investigation of heat losses in

hydrogen-doped parabolic trough receivers. *SolarPACES Conference Proceedings*, 3, 2025.

[69] Frank Burkholder and Chuck Kutscher. Heat loss testing of Schott's 2008 PTR70 parabolic trough receiver. Technical Report NREL/TP-550-45633, National Renewable Energy Lab. (NREL), Golden, CO (United States), 2009.

[70] F. Burkholder and C. Kutscher. Heat-loss testing of Solel's UVAC3 parabolic trough receiver. Technical Report NREL/TP-550-42394, National Renewable Energy Lab. (NREL), Golden, CO (United States), 2008.

[71] Dongqiang Lei, Qiang Li, Zhifeng Wang, Jian Li, and Jianbin Li. An experimental study of thermal characterization of parabolic trough receivers. *Energy Conversion and Management*, 69:107–115, 2013.

[72] José M. Márquez, Rafael López-Martín, Loreto Valenzuela, and Eduardo Zarza. Test bench heatrec for heat loss measurement on solar receiver tubes. *AIP Conference Proceedings*, 1734(1):030025, 2016.

[73] Eneko Setien, Rafael López-Martín, and Loreto Valenzuela. Methodology for partial vacuum pressure and heat losses analysis of parabolic troughs receivers by infrared radiometry. *Infrared Physics & Technology*, 98:341–353, 2019.

[74] S. Caron and M. Röger. In-situ heat loss measurements of parabolic trough receivers based on transient infrared thermography. *Solar Energy*, 135:111–121, 2016.

[75] María Elena Carra, Eneko Setién, Loreto Valenzuela, Rafael López-Martín, Carmen Amador, Simon Caron, Jesús Ballestrín, Jesús Fernández-Reche, José A. Carballo, and Antonio Ávila Marín. Study of parameters influence on the measurement of vacuum level in parabolic trough collectors' receivers using infrared thermography. *Infrared Physics & Technology*, 131:104657, 2023.

[76] Ayoub Oufadel, Massaab El Ydrissi, Aicha Alami Hassani, Hicham Ghennioui, Abdelattif Ghennioui, El Ghali bennouna, Abderrahmane El Amri, and Farid Abdi. In-situ heat losses measurements

of parabolic trough receiver tubes based on infrared camera and artificial intelligence. *Environmental Challenges*, 10:100679, 2023.

[77] Miguel-Angel Pérez-Cutiño, Aggelos Pikrakis, José-Miguel Díaz-Báñez, and Juan Valverde. Meta-learning with hypernetworks: Cost-effective fault detection in parabolic trough plants. *Engineering Applications of Artificial Intelligence*, 133:108492, 2024.

[78] Thomas Kraft, Gregor Bern, Shahab Rohani, Mark Schmitz, and Werner Platzer. Vacuum loss detection of PTC in CSP plants via temperature-sensors. *SolarPACES Conference Proceedings*, 2, 2024.

[79] Greg C. Glatzmaier. Hydrogen measurement & extraction at Nevada solar one. *SolarPACES Conference Proceedings*, 2, 2024.

[80] R. Forristall. Heat transfer analysis and modeling of a parabolic trough solar receiver implemented in engineering equation solver. Technical Report NREL/TP-550-34169, National Renewable Energy Laboratory (NREL), Golden, CO, 2003.

[81] Ricardo Vasquez Padilla, Gokmen Demirkaya, D. Yogi Goswami, Elias Stefanakos, and Muhammad M. Rahman. Heat transfer analysis of parabolic trough solar receiver. *Applied Energy*, 88(12):5097–5110, 2011.

[82] Soteris A. Kalogirou. A detailed thermal model of a parabolic trough collector receiver. *Energy*, 48(1):298–306, 2012.

[83] Zhiyong Wu, Shidong Li, Guofeng Yuan, Dongqiang Lei, and Zhifeng Wang. Three-dimensional numerical study of heat transfer characteristics of parabolic trough receiver. *Applied Energy*, 113:902–911, 2014.

[84] Jiangfeng Guo, Xiulan Huai, and Zhigang Liu. Performance investigation of parabolic trough solar receiver. *Applied Thermal Engineering*, 95:357–364, 2016.

[85] Dongqiang Lei, Yucong Ren, and Zhifeng Wang. Numerical study of conduction and radiation heat losses from vacuum annulus in parabolic trough receivers. *Frontiers in Energy*, 16:1048–1059, 2022.

[86] Evangelos Bellos, Christos Tzivanidis, and Dimitrios Tsimpoukis. Optimum number of internal fins in parabolic trough collectors. *Applied Thermal Engineering*, 137:669–677, 2018.

[87] İbrahim Halil Yılmaz and Aggrey Mwesigye. Modeling, simulation and performance analysis of parabolic trough solar collectors: A comprehensive review. *Applied Energy*, 225:135–174, 2018.

[88] Fritz Zaversky, Rodrigo Medina, Javier García-Barberena, Marcelino Sánchez, and David Astrain. Object-oriented modeling for the transient performance simulation of parabolic trough collectors using molten salt as heat transfer fluid. *Solar Energy*, 95:192–215, 2013.

[89] Ze-Dong Cheng, Ya-Ling He, and Yu Qiu. A detailed nonuniform thermal model of a parabolic trough solar receiver with two halves and two inactive ends. *Renewable Energy*, 74:139–147, 2015.

[90] F. R. Menter. Two-equation eddy-viscosity turbulence models for engineering applications. *AIAA Journal*, 32(8):1598–1605, 1994.

[91] S.M.A. Rahman, Salah Issa, Abdul Ghani Olabi, and Mohammad Ali Abdelkareem. Numerical investigation of the thermal-hydraulic performance of a novel parabolic trough wavy tubular receiver by using fmwnct/oil-nanofluid coupled with fins. *Case Studies in Thermal Engineering*, 59:104431, 2024.

[92] Mridul Sharma and Ravindra Jilte. Heat transfer and hydraulics for a novel receiver pipe of solar parabolic trough: a computational approach. *Environmental Science and Pollution Research*, 2023.

[93] Mahfuja A. Khuda, Javad Khalesi, Zecan Tu, Yun Long, Daniela Piccioni Koch, and Nenad Sarunac. Numerical analysis of a developing turbulent flow and conjugate heat transfer for molten salt and liquid sodium in a solar receiver. *Applied Thermal Engineering*, 217:119156, 2022.

[94] Zecan Tu, Daniela Piccioni Koch, Nenad Sarunac, Martin Frank, and Junkui Mao. Thermal analysis of a solar external receiver tube with a novel component of guide vanes. *Energies*, 14(8), 2021.

[95] Mahfuja A Khuda, Javad Khalesi, Zecan Tu, Yun Long, Daniela Piccioni Koch, and Nenad Sarunac. Numerical analysis of a developing turbulent flow and conjugate heat transfer for molten salt and liquid sodium in a solar receiver. *Applied Thermal Engineering*, 217:119156, 2022.

[96] Sumeet Anand and Sumit Kumar. Optimization of gaseous working fluid and internally finned absorber tube for enhancing the thermal performance of parabolic trough solar collector. *Applied Thermal Engineering*, 239:122078, 2024.

[97] Ansys Inc. *Ansys Fluent Theory Guide, Release 2025 R1*. Ansys, Inc., Canonsburg, Pennsylvania, USA, 2025. https://www.ansys.com.

[98] Ansys Inc. *Ansys Fluent User's Guide, Release 2025 R1*. Ansys, Inc., Canonsburg, Pennsylvania, USA, 2025. https://www.ansys.com.

[99] Vinod Kumar, Carlo Nonino, and Stefano Savino. On the improvement of the thermal performance of longitudinally finned parabolic trough solar receivers. *Applied Thermal Engineering*, 279:127840, 2025.

[100] Y.A. Jebbar, F.K. Fluiful, W.J. Khudhayer, N. Ali Hasson, and A.J. Abdulhamed. Improvement of heat transfer in a parabolic trough collector receiver tube with hollow cylindrical inserts: A cfd study. *International Journal of Heat and Technology*, 42(3):924–932, 2024.

[101] V.E. Dudley, Gregory Kolb, A.R. Mahoney, T.R. Mancini, C.W. Matthews, M. Sloan, and D. Kearney. Test results: SEGS LS-2 solar collector. Technical Report SAND94-1884, SANDIA National Laboratories, 1994.

[102] Dušan P. Sekulić and Ramesh K. Shah. *Fundamentals of Heat Exchanger Design*. Wiley, 2023.

[103] R.L Webb and E.R.G Eckert. Application of rough surfaces to heat exchanger design. *International Journal of Heat and Mass Transfer*, 15(9):1647–1658, 1972.

[104] A. Fernández-García, E. Zarza, L. Valenzuela, and M. Pérez. Parabolic-trough solar collectors and their applications. *Renewable and Sustainable Energy Reviews*, 14:1695–1721, 2010.

[105] Mohamed S. Shahin, Mehmet F. Orhan, and Faruk Uygul. Thermodynamic analysis of parabolic trough and heliostat field solar collectors integrated with a rankine cycle for cogeneration of electricity and heat. *Solar Energy*, 136:183–196, 2016.

[106] Peng Liu, Zhimin Dong, Hui Xiao, Zhichun Liu, and Wei Liu. Thermal-hydraulic performance analysis of a novel parabolic trough receiver with double tube for solar cascade heat collection. *Energy*, 219:119566, 2021.

[107] Ansys Inc. *Ansys Fluent User's Guide, Release 2025 R1*. Ansys, Inc., Canonsburg, Pennsylvania, USA, 2025. https://www.ansys.com.

[108] H. Blasius. Das aehnlichkeitsgesetz bei reibungsvorgängen in flüssigkeiten. *Mitteilungen über Forschungsarbeiten auf dem Gebiete des Ingenieurwesens*, 131:1–49, 1913.

[109] V. Gnielinski. New equations for heat and mass transfer in turbulent pipe and channel flow. *Int. Chem. Eng*, 16(2):359–368, 1976.

[110] F-Chart Software. Engineering equation solver (ees), 2025.

[111] A. C. Ratzel, C. E. Hickox, and D. K. Gartling. Techniques for reducing thermal conduction and natural convection heat losses in annular receiver geometries. *Journal of Heat Transfer*, 101(1):108–113, 1979.

[112] F. Incropera, David DeWitt, Theodore Bergman, and Adrienne Lavine. *Fundamentals of Heat and Mass Transfer*. 2007.

[113] Aggrey Mwesigye, İbrahim Halil Yılmaz, and Josua P. Meyer. Numerical analysis of the thermal and thermodynamic performance of a parabolic trough solar collector using SWCNTs-Therminol®VP-1 nanofluid. *Renewable Energy*, 119:844–862, 2018.

[114] J. O. Hirschfelder, C. F. Curtiss, and R. B. Bird. *Molecular Theory of Gases and Liquids*. John Wiley & Sons, New York, 1954.

[115] National Renewable Energy Laboratory. Concentrating solar power projects – solarpaces. https://solarpaces.nrel.gov/. Accessed: 2025-10-14.

[116] Manuel Botejara-Antúnez, Jaime González-Domínguez, Francisco Javier Rebollo-Castillo, and Justo García-Sanz-Calcedo. Life cycle and environmental impact assessment of heat transfer fluids in parabolic trough csp plants. *Sustainable Energy Technologies and Assessments*, 74:104188, 2025.

[117] Eastman Chemical Company. Eastman product finder: Heat transfer fluids. https://www.eastman.com/en/products/product-finder, Accessed: 2025-10-14.

[118] Therminol® VP-1 Heat Transfer Fluid, Accessed: 2025-05-02.

[119] Therminol® VP-1 Heat Transfer Fluid: Product Technical Data Sheet, Accessed: 2025-05-02.

[120] B.S. Petukhov. Heat transfer and friction in turbulent pipe flow with variable physical properties. In *Advances in Heat Transfer*, volume 6, pages 503–564. Elsevier, 1970.

[121] Loreto Valenzuela, Rafael López-Martín, Carmen M. Amador-Cortés, and Christoph Hilgert. Experimental heat losses in hydrogen-doped parabolic trough receivers. *SolarPACES Conference Proceedings*, 3, 2024.

[122] F. Schaube, A. Kohzer, J. Schütz, A. Wörner, and H. Müller-Steinhagen. De- and rehydration of Ca(OH)2 in a reactor with direct heat transfer for thermo-chemical heat storage. Part A: Experimental results. *Chemical Engineering Research and Design*, 91(5):856–864, 2013.

[123] F. Schaube, I. Utz, A. Wörner, and H. Müller-Steinhagen. De- and rehydration of Ca(OH)2 in a reactor with direct heat transfer for thermo-chemical heat storage. Part B: Validation of model. *Chemical Engineering Research and Design*, 91(5):865–873, 2013. Publisher: Elsevier BV.

[124] Guy Ervin. Solar heat storage using chemical reactions. *Journal of Solid State Chemistry*, 22(1):51–61, 1977.

[125] D.R. Brown, J.L. LaMarche, and G.E. Spanner. Chemical energy storage system for SEGS solar thermal power plant. Technical report, Pacific Northwest National Laboratory (PNNL), Richland, WA, 1991.

[126] Franziska Schaube, Antje Wörner, and Rainer Tamme. High Temperature Thermochemical Heat Storage for Concentrated Solar Power Using Gas–Solid Reactions. *Journal of Solar Energy Engineering*, 133(3):031006, 2011.

[127] M. Linder, Chr. Roßkopf, M. Schmidt, and A. Wörner. Thermochemical Energy Storage in kW-scale based on CaO/Ca(OH)2. *Energy Procedia*, 49:888–897, 2014.

[128] J. Yan and C.Y. Zhao. Experimental study of CaO/Ca(OH)2 in a fixed-bed reactor for thermochemical heat storage. *Applied Energy*, 175:277–284, 2016.

[129] Abhishek Singh, Stefania Tescari, Gunnar Lantin, Christos Agrafiotis, Martin Roeb, and Christian Sattler. Solar thermochemical heat storage via the Co3O4/CoO looping cycle: Storage reactor modelling and experimental validation. *Solar Energy*, 144:453–465, 2017.

[130] Xinyi Luo, Wei Li, Lianjie Zhang, Min Zeng, Jirí Jaromír Klemeš, and Qiuwang Wang. Effects evaluation of Fin layouts and configurations on discharging performance of double-pipe thermochemical energy storage reactor. *Energy*, 282:128821, 2023.

[131] Jinzhi Cai and Zhenshan Li. First principles-based kinetic analysis of Ca(OH)2 dehydration in thermochemical energy storage system. *Journal of Energy Storage*, 97:112759, 2024.

[132] Haocheng Sun, Zhiwei Ge, Zhihan Yao, Liang Wang, Xipeng Lin, Yakai Bai, Shuang Zhang, and Haisheng Chen. Advancing calcium-based thermochemical heat storage: Impact of a dual-reaction strategy on the system performance. *Applied Energy*, 396:126299, 2025.

[133] W.J. Yan, H. Ye, Ge Zhu, and Y.B. Tao. An innovative integration of parabolic trough collector with advanced thermochemical heat storage systems. *Solar Energy*, 300:113774, 2025. Publisher: Elsevier BV.

[134] Carlos Ortiz, Marco Binotti, Matteo C. Romano, José Manuel Valverde, and Ricardo Chacartegui. Off-design model of concentrating solar power plant with thermochemical energy storage based on calcium-looping. *AIP Conference Proceedings*, 2126(1):210006, 2019.

[135] R. Bravo, C. Ortiz, R. Chacartegui, and D. Friedrich. Hybrid solar power plant with thermochemical energy storage: A multi-objective operational optimisation. *Energy Conversion and Management*, 205:112421, 2020.